Design and Fabrication of Plasmonic Nanostructures for Multifunctional Applications

by

Haseeb Ahmed

A thesis submitted in partial fulfillment of the requirements for the degree of

Master of Science

in

Microsystems and Nanodevices

Department of Electrical and Computer Engineering
University of Alberta

ABSTRACT

Plasmonic nanostructures have received increasing attention due to their unique ability to mediate the conversion of light into different forms of energy. This opens pathways for numerous applications from ultrasensitive surface-enhanced Raman scattering (SERS) materials characterization to heterogeneous photocatalysis and green energy harvesting. However, plasmonic nanostructures should meet a number of requirements for their potential to be realized. In addition to nanoscale dimensions, a high uniformity and compatibility with existing microelectronics and microfluidics settings are required. Direct-write nanofabrication techniques, such as electron beam lithography (EBL) and more recently, focused ion beam (FIB) processes offer unmatched control over nanoscale geometries and also high flexibility to allow for various designs. However, careful co-optimization of the process conditions is required to fabricate periodic nanopatterns efficiently. Use of dielectric substrates, which are often required for nanoplasmonic designs, is particularly challenging for EBL fabrication due to the accumulation of charge during EBL exposures. In this work, a 10 keV EBL process was optimized to fabricate periodic arrays of 50 nm pitch holes in positive-tone EBL resist (polymethyl methacrylate or PMMA) on fused silica (FS) supports. The patterned PMMA was used as a lift off mask to create 50 nm pitch arrays of Au dots on FS. In order to verify the performance of these Au/FS structures, SERS biodetection experiments were performed. For this purpose, the samples were bio-functionalized with thiolated DNA aptamers that bind specifically to an important biomarker, protein interleukin 6 (IL-6). The samples were loaded with IL-6 from a solution and characterized by SERS. The results suggest that the fabricated Au/FS plasmonic nanostructures are efficient for SERS enhancement, and potentially also for broader applications. In order to test multifunctional applications, Au/FS plasmonic substrates created by physical vapour deposition (PVD) deposition of Au were additionally employed to characterize liquid-liquid phase separation in a solution of microtubule-associated protein tau, which plays an important role in Alzheimer's, Parkinson's, and several other neurodegenerative diseases. The results suggest that plasmonic substrates may both facilitate liquid-liquid phase separation in solutions of proteins and enhance the SERS effect, which makes possible in-situ characterization of proteinaceous phase-condensates. Furthermore, 10 keV EBL was employed to fabricate plasmonic Ag nanostructures on indium-titanium oxide (ITO) supports in various designs. Currently, the Ag/ITO plasmonic nanostructures are undergoing characterization in a collaborator's group. An alternative nanopatterning technique, He-FIB milling, was also tested. A superb positional control was achieved; however, the He-FIB technique was found to be slower than EBL for the fabrication of large arrays of plasmonic nanostructures. To summarize, the results demonstrate that plasmonic nanostructures consisting of nanostructured noble metals such as Au or Ag on dielectric supports could potentially serve for a broad variety of applications. The challenges relate primarily to the efficiency and cost of the direct-write processes such as EBL or FIB. Further optimization would address, in the first place, improvements of the sensitivity of EBL and/or FIB nanopatterning.

ACKNOWLEDGMENT

All praises belong to Allah, Lord Almighty, and my dearest companion for providing me with the great opportunity, strength, and capability in completing pursue this MSc degree. Peace and blessings be upon our Prophet Muhammad (SAW), his family, and companions.

First and foremost, I would like to express my sincere appreciation to Dr. Maria Stepanova and Dr. Steven Dew for allowing me to study and research on such incredible projects. Also, both served as my supervisors during the entire period of my degree. I would like to present my immense gratitude to them for their outstanding guidance, motivation, and financial and moral support throughout this work. They ignited a newly acquired curiosity in me and a passion for learning about the interesting fields of nanofabrication and biosensing. I appreciate very much for the chance and assistance they provided me, although it has been challenging and full of meaningful learning experiences.

I want to express my gratitude to the member of my research team whose knowledge served as one of the pillars of my formational work. I want to thank Dr. Min Wu because she personally contributed to the advancement of this work.

I would also like to offer my great appreciation to Dr. Karthik Shankar from the Department of Electrical and Computer Engineering (ECE) at the University of Alberta and his group members, Navneet Kumar, Dr. Kazi Alam, and Narendra Chaulagain, for their collaboration, especially with the preparing of substrates and subsequent testing of heptamer plasmonic structures.

I am highly appreciative of the involvement of Dr. Holger Wille, as well, from the Centre for Prions and Protein Folding Diseases (CPPFD) at the University of Alberta, and his group member, Dr. Jose Miguel Flores Fernandez, for his help and support in preparing the tau protein solutions for the liquid-liquid phase separation.

I would also like to present my gratitude to many staff members working at the nanoFAB in the University of Alberta, especially Dr. Gustavo de Oliveria Luiz, Dr. Shihong Xu, Dr. Peng Li and Dr. Shiau-Yiu Wu, for their ideas, training, and utmost support.

Finally, I would like to express my endless gratitude and love to my beloved parents (Mama and Papa) for raising me and giving me an excellent education, finances, love, prayers, and support all the time, and of course, to my dearest siblings for their tremendous support, love, and prayers as well. Notably, the advice and guidance received from my older brother (Mr. Asif Ali) were lifesaving. Also, I would like to thank to all my spiritual brothers, friends, and relatives. All of your support has been a great source of inspiration for me throughout this journey. Lastly, I would like to dedicate all my successes to Allah, as without His blessings, I would never have completed this degree. With that, I would like to present this dissertation.

Table of Contents

List of Tables

List of Figures

List of Abbreviations

BSD – Backscatter detector

c-FEG – Cold field emission gun

DI – De-ionized

EBL – Electron beam lithography

FBMS – Fixed beam moving stage

FESEM – Field emission scanning electron microscope

FIB – Focused ion beam

FS – Fused silica

GAMESS – General Atomic & Molecular Electronic Structure System

HIM – Helium ion microscope

HSQ – Hydrogen silsesquioxane

IL-6 – Interleukin 6ITO – Indium-tin-oxide

LSPR – Localized surface plasmon resonance

MB – Methylene blue

MNP – Metallic nanopattern

NPVE – Nanopatterning and Visualization Engine

PMMA – Polymethylmethacrylate

PVD – Physical vapor deposition

SE – Secondary electrons

SELEX – Systematic evolution of ligands by exponential enrichment

SEM – Scanning electron microscope

SERS – Surface enhanced Raman scattering

Si – Silicon

SP – Surface plasmon

SPR – Surface plasmon resonance

1. Introduction

Plasmonic nanostructures, which commonly consist of nanometre scale noble metal structures interfacing a dielectric, possess unique properties. Exposure of such nanostructures to light produces oscillations of electron density, known as surface plasmons, accompanied by a very efficient absorption of incoming photons. This leads to a conversion of energy from light into "hot-spots" – nano-sized regions where electromagnetic energy is accumulated due to the excitation of the plasmon oscillations. The possibility of additional conversion of the energy of highly localized hot-spots into different forms[1,2] opens paths for numerous applications, from ultrasensitive surface-enhanced Raman scattering (SERS) characterization of the material[3,4,5] to heterogeneous photocatalysis[6,7,8,9] and green energy harvesting[2,9].

In particular, SERS employs the enhancement of inelastic Raman scattering of light by materials located in the immediate neighborhood of nanostructures where the surface plasmonic waves are generated, often termed plasmonic substrates. The technique captures unique vibrational signatures of molecules with an unparalleled sensitivity and allows for selective detection of ultra-small amounts of materials, down to monolayers and even single molecules[3,4,5]. Moreover, a promising emerging application combines plasmonic-driven photocatalytic modification of materials with ultrasensitive SERS detection in-situ within a single multifunctional design[10,11,12,13,14]. This could enable the efficient manufacturing of highly specific and valuable compounds at a high rate and with minimal energy. However, plasmonic nanostructures should meet a number of requirements to be efficient for the SERS enhancement and other applications. In addition to proper selection of materials and nanoscale dimensions, a high uniformity and compatibility with existing microelectronic, photonic, microfluidic and micro-electromechanical systems are required[5,15,16].

Electron beam lithography (EBL) offers unmatched control over nanoscale geometries, and also flexibility to allow for almost arbitrary structures and designs[15,17]. However, careful co-optimization of EBL exposure and development steps is required to reliably fabricate periodic patterns with deep nanoscale dimensions[18,19]. Usage of dielectric substrates is particularly challenging due to the accumulation of charge during exposure resulting in defocusing of the electron beam and distortions of the pattern. In this work, a 10 keV EBL process was optimized to fabricate periodic arrays of 50 nm pitch Au dots on fused silica (FS) supports whose performance was then tested as plasmonic substrates for SERS bio-detection.

2. Literature Review

2.1. Optical Biosensors

Biosensors are analytical devices, which are used to detect the presence of specific chemical or biological compounds (analytes) by using biological or bioinspired materials as recognition elements and ideally generate output signals proportional to the amount of analyte[20,21,22,23,24,25]. Commonly used biological recognition elements (bio-receptors) include nucleic acids (DNA/RNA) or aptamers[26,27,28] antibodies/antigens[29], enzymes[30], entire cells[31,32,33], and their organelles[34,35,36]. Bio-sensing is basically comprised of five different stages, which can be described as follows:

1. Biomolecules or living organisms are exposed to a target substance either in an aqueous solution or gaseous state.
2. Biological recognition receptors bind the analytes of interest.
3. The acts of binding (recognition) of the analyte by biological elements of the sensor produce physicochemical responses, which are commonly transformed into electrical or other signals of recognizable form using proper transduction elements.

4. The signal is amplified, processed as required for conversion into readable format, and forwarded to display.
5. The processed and converted signal is then displayed and recorded in the form of charts, data reports and graphs output for the end user (see **Figure 1**)[37,38,39,40,41,42].

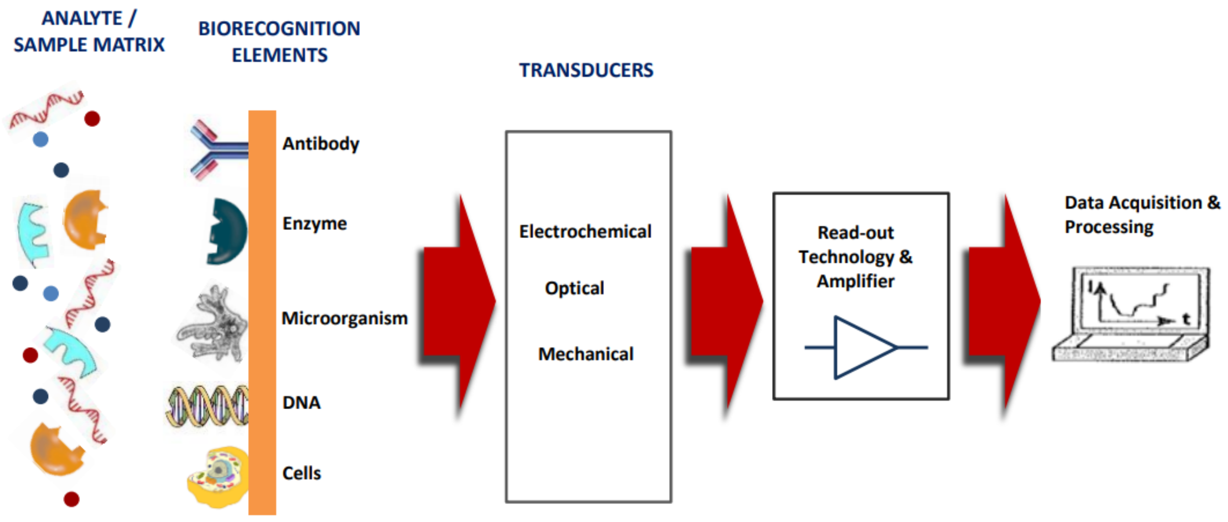

Figure 1: Schematic diagram of biosensor comprising five different aspects: targeting of analyte, recognition of elements, transducing system, amplification and electronics, data acquisition and output-display[43] (reproduced with permission of University College Cork).

In biological interactions, molecular recognition plays a crucial role. Molecular recognition is specific non-covalent binding between two or more macromolecules that includes such interactions as, for example, hydrogen bonding, π-π interactions, and/or various electrostatic effects[44]. In biological systems, the non-covalent binding energies vary depending upon the interacting groups; for example hydrogen bonding energies[45] may be in the range from 2 to as much as 40 kcal/mol; π-π interaction[45,46] (π-stacking) may take values up to 100 kcal/mol, although the most often encountered values are under 10 kcal/mol; whereas salt bridging[45,47] (sometimes referred to as dipole-dipole interaction) typically has binding energy under 30 kcal/mol. Energies of most non-covalent bonds are less than those of covalent bonds, which generally are in the range from 70 to 360 kcal/mol[48]. In typical biological systems, energies of non-covalent intermolecular binding are typically less than 10-15 kcal/mol[49], which is only a marginally stable affinity at physiological conditions. For the relatively weak non-covalent intermolecular bonding to occur and remain sufficiently robust, the molecules should possess a geometrical complementarity, also known as the lock and key principle[50]. The resulting specific biomolecular recognition is necessary to life and has many forms. It is involved in almost all stages of biological processes such as protein synthesis, response of immune system involving antibody-antigen pairing, replication of DNA, and receptor ligand interactions[51,52,53,54,55,56]. These interactions show high selectivity that offer significant interest for biosensing technologies.

Depending on the element of recognition used in a biosensor, the most common biologically inspired recognition events can be subdivided into several categories[57,58] including affinity recognition (for example, antibody-antigen binding)[59], catalytic recognition (binding involving enzymes, or enzyme-containing organelles or tissues)[60] or hybridization (binding of complementary DNA or RNA molecules)[61,62]. These biological recognition events can be monitored by using a range of physical and chemical transducers. They can be broadly described as optical, mechanical and electrical transducers as shown in **Figure 1.**

The market of biosensing devices is considerable and growing very quickly. This can involve easy-to-use self-testing devices for monitoring of glucose, oxygen, cholesterol level in blood; biomarkers for pregnancy or ovulation, as well as for various diseases including diabetes, viral infection and cancer[63,64,65,66,67,68]. Biological agents that are commonly targeted for detection in molecular biosensing include pathogens (i.e. bacteria, viruses), toxins (i.e. ricin), metabolites, and enzymes[69,70,71,72].

Major areas of biosensor applications are medical/clinical[73,74], agricultural including food testing and food pathogens detection[75,76], environmental monitoring[77,78], and defence applications[79]. Importantly, portability and in-situ measurements enabled by ongoing biosensing systems' miniaturization are among current trends in research and development of biosensors[80,81,82,83,84].

One more of many important challenges in real-time biosensing is timely analyte detection. Often, quick and reliable analysis is crucial in applications of biosensors[85,86]. Especially in health and safety applications, the need for fast analysis can be of paramount importance, yet current speed capabilities of biosensing are often limited. For a thorough assessment, quantitative accuracy can be an important aspect under some circumstances as the detection of higher or lower than the expected value would be crucial.

A key challenge in biosensors development is achieving selectivity to a specific analyte in the presence of interfering species. A high commercial interest has been generated by combinations of selectivity with sensitivity and additional features such as miniaturization, low cost, speed of operation and the possibility of continuous real-time measurements[87]. Sensitivity in particular is important, since a low signal-to-noise ratio can limit the detection capability of biosensors for many different applications[88].

Rational design based upon computational modeling is used broadly to improve binding affinities of recognition elements and achieve the highest possible selectivity against specific analytes, as well as optimise other functionalities of biosensors[89,90,91]. In particular, the combinatorial chemistry technique known as the systematic evolution of ligands by exponential enrichment (SELEX)[92] is used broadly to develop DNA and RNA aptamers that specifically bind to required compounds[93].

Although computation-based rational design of recognition elements has proven to be very efficient, non-specific binding has remained a challenge, especially when analyzing multicomponent biological samples[94]. Non-specific binding is the binding of untargeted molecules to the assay surface or detection reagents in affinity binding assays unrelated to the particular interaction being investigated. The sensitivity and specificity of the test may be impacted by non-specific binding, which may provide false positives and erroneous interpretations. A variety of techniques have been attempted to mechanically prevent or eliminate unspecific binding, such as e.g. using blocking agents or rinsing the sensor's surface[94]. Nevertheless, intense research efforts have been directed toward continuing the design of lock-and-key and/or switchable recognition elements that would prevent nonspecific binding due to geometrical selectivity or adaptive conformational response of the recognition elements[50,94].

An alternative paradigm of multiplex biosensing, which initially has been inspired by the mammalian senses of taste and smell, uses an array of sensors that do not necessarily all employ the lock-and-key principle[95]. The current concept of multiplexing includes the detection of multiple analytes in a single measurement, or alternatively, detection of a single analyte using several types of recognition elements[96,97]. Either technique offers a way to mitigate the effect of potential unspecific binding when analyzing realistic multicomponent biological samples. In the recent years, multiplex biosensing has gained acceptance and recognition, especially when employing rationally engineered, adaptive recognition elements[98]. Importantly, due to increased throughput multiplex biosensing offers a promise of real-time monitoring of analytes.

Technological challenges to be overcome include the need for transducing techniques that would allow efficient multiplexing and readout of the results.

2.2. Nanostructures

Nanostructures are objects whose one, two or three dimensions range from 1 nm (molecular scale) to 100 nm[99,100,101,102]. With the help of existing lithography and deposition techniques, nanostructures can be fabricated with a precision often down to the single-atom level[103]. Examples of nanostructures include hollow nanofibers[104], nanospheres[102,103], nanorods[102,103], and other structures with nano-dimensions[101,103,104]. These nanostructures may be biological or inorganic; natural or synthetic. Nanostructures are the basic building blocks of any nanostructured materials such as nanofibers[104,105].

Properties of nanostructures often depend upon their electronic structure and mobility of free electrons in various dimensions. In one-dimensional (1D) nanostructures, electrons are confined only in a 1D quantum well and are free to move in the other two dimensions. For example, an 1D quantum well represents a material where a thin layer of narrow-bandgap semiconductor is sandwiched between two wide-gap ones. A two-dimensional (2D) quantum well is usually represented as a 2D electronic system[106], where electrons are confined in two dimensions and free to move in the remaining 1D (e.g. quantum wires). Nanotubes, nanowires, and in some cases chains of polymers are examples of such quantum wires[107,108]. In quantum dots, motion of electrons is confined in all three dimensions, for example in various nanoparticles and nano-crystals[109,110,111]. Nanofibres and nanotubular materials are examples of one-dimensional (1D) nanomaterials, whose length may range from 100nm to 10µm[112]. Films or coating with the thickness of several nanometers are examples of two-dimensional (2D) nanomaterials[113]. Often such nanostructures of

0D, 1D, and 2D are applied on a substrate dispersed in a macroscopic fluid or solid matrix. Solutions, powders, fibrous and polycrystalline materials are examples of macroscopic materials in which nano-size structural elements of 0D, 1D, and 2D are contained[114],[115]. In nanostructured materials, the important characteristics are the dependencies of certain properties such as electronic structure, delocalized valence electron spatial confinement, or quantum size effects, on the size of nanoscale components of the material. Other properties may include high reactivity due to large surface area; altered nature of equilibrium phases in nanoparticles; or a dependence of diffusion rates on the size of the nanostructure. Overall, nanostructured materials are of particular interest due to their unique optical, chemical, mechanical, and magnetic properties[116,117,118,119].

Nanostructures differ from both individual atoms or molecules and macroscopic bulk materials. Their mechanical, electrical, optical, and chemical properties can be altered by controlling their size as well as the structure of their surface down to the atomic level. To understand the relationship between the structure of a nanomaterial and its function in a device, advanced characterization methods are crucial. By varying the size, shape and composition of nanostructures, their properties can be widely changed[113], which may result, in particular, in specific and unique sensing capabilities.

2.3. Nanoplasmonics and its Applications

2.3.1. Surface Plasmons

The interaction of metallic structures with the electromagnetic radiation is largely defined by free conduction electrons in the metal. When light strikes metal nanostructures, a phenomenon known as surface plasmon generation is triggered[120]. This includes coherent collective oscillations of delocalized electrons of the metal and a buildup of electromagnetic field at the interface of the materials around the nanostructures, as depicted in **Figure 2**. These collective oscillations of electrons are called surface plasmons (SPs). The SPs exist at an interface of a conductor (i.e. a metal, generally) and a dielectric. According to Gauss's Law, surface charge density is inversely proportional to its radius of curvature[120]. This means that the strongest electromagnetic fields occur near regions of accumulation of localized charges, such as sharp edges at the interface. The electronic charge-density oscillations associated with surface plasmons can give rise to strongly enhanced electromagnetic near-fields, which are confined near the metal surface[120].

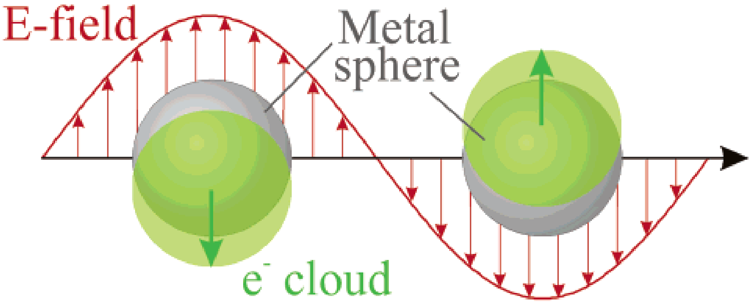

Figure 2: Schematic diagram for the movement of the conduction electron charge cloud relative to the nuclei during plasmon oscillations in a sphere as light propagates from left to right[121] (reproduced with permission from American Chemical Society).

Electromagnetic responses that accompany the generation of plasmon oscillations on the surface of a material depend on the frequency of the oscillations. Enhancement of these responses at certain frequencies is known as the surface plasmon resonance[118,120]. Resonance that occurs in an array of separate nanostructures is termed localized surface plasmon resonance (LSPR) The resonant frequencies depend on the material and geometrical characteristics of the nanostructures where plasmonic waves are induced by incoming light. If the material-dependent resonant frequency is close to the frequency of the incident light, resonant absorption of the light takes place. In addition, scattering of incident light is also enhanced in the presence of LSPR. Alternatively, if the resonant frequency is different from the frequency of the incident light, the resonance would not take place.

Figure 3: Broad spectrum of the SPR and other sensing applications that use surface plasmons[124] (reproduced with permission from Elsevier).

Increase in the absorption and/or scattering of incoming light that accompanies the LSPR is employed for a label-free technique used for many applications such as photo-detection, characterization of materials, bio-detection, environmental and food monitoring sensors, and security detection purposes. LSPR sensing devices commonly use gold, silver, copper and aluminum as the plasmonic materials. Currently, the most often used plasmonic material is gold due to its great biocompatibility, chemically inertness and stability. **Figure 3** shows the multifunctional applications of surface plasmons for various sensing applications[122,123,124].

2.3.2. Surface Enhanced Raman Spectroscopy (SERS)

Surface enhanced Raman spectroscopy or surface enhanced Raman scattering (SERS) is a method of ultrasensitive chemical detection that employs the enhancement of Raman scattering in the presence of plasmonic nanostructures. The Raman scattering, or Raman effect, was discovered by Chandrasekhara Venkata Raman in 1928 when observing the emission of light from atoms and molecules using basic optics tools such as color filtering of the sunlight and visual detection[125,126]. The Raman effect is an inelastic scattering of photons from an atom or molecule, resulting in the energy of photons being altered. This shift in a photon's energy matches the difference in the molecules' vibrational energy levels involved in the scattering[127,128].

In Raman spectroscopy, the altered frequencies that arise from inelastic scattering of initially monochromatic laser light are detected. These altered frequencies are representative of unique vibrational modes of probed molecules. The inelastic scattering which was initially observed by C.V. Raman is currently termed the anti-Stokes Raman scattering, when the energy of photons scattered inelastically is increased, whereas the vibrational energy of the molecules is decreased. In contrast, the Stokes Raman scattering results in a decrease in the energy of the scattered photons[129,130,131,132]. However, the vast majority of photons that interact with a molecule experience the Rayleigh or elastic scattering, whereas only a tiny minority of photons are scattered inelastically. The two kinds of Raman scattering[133], as well as the Rayleigh scattering, are shown in the schematic diagram in **Figure 4**.

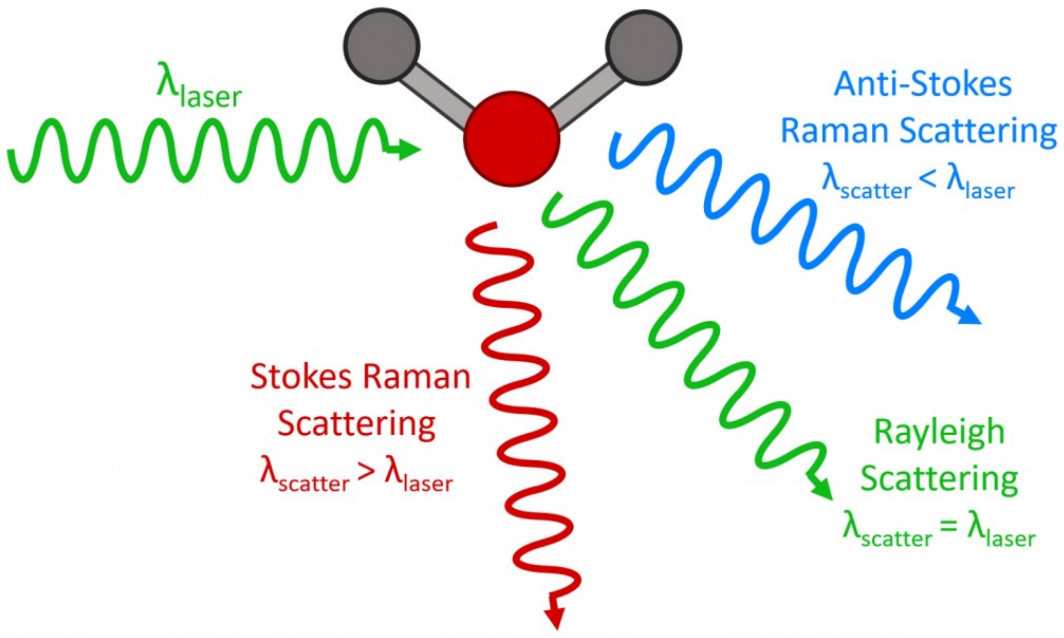

Figure 4: Schematic diagram illustrating the interaction of light with molecules via the three different types of scattering[133] (reproduced with permission from Edinburgh Instruments).

Due to the direct relation of Raman scattering with differences of vibrational energy levels of molecules, the Raman scattering spectra are representative of distinctive vibrational fingerprints that identify the molecules, as illustrated by **Figure 5**. In that, Raman scattering differs from fluorescence, when the energy of incident photons is absorbed by atoms or molecules[134] and the emission of photons occurs after the molecule relaxes to a lower electronic level. As the difference of molecular vibrational energy levels is constant, even with a different frequency of the excitation, similar vibrational fingerprints of molecules can be obtained which carry information about molecular vibrational modes. The Jablonski diagram in **Figure 5** shows the transitions between molecular energy levels that result in a Raman effect. Since the incident photons' energy is not sufficient for the molecule to get excited from the ground state up to the lowest electronic state, virtual energy levels are involved in Raman scattering instead of the electronic quantum states of the molecule. After scattering, the photons acquire lower energy in the case of Stokes Raman scattering. In terms of the wavelength, the photon is shifted toward the red end of the spectrum. Since at room temperature most molecules are in their lowest vibrational states, Raman scattering is predominantly a Stokes scattering. The anti-Stokes Raman scattering is quite weak in comparison with the Stokes Raman scattering. The reason is that a relatively small number of molecules are found in higher vibrational levels, which might result in the photons acquiring higher energy leading to a blue shift after the scattering.

Cross-sections of Raman scattering are low in comparison with fluorescence[135,136]. Whereas cross-sections of fluorescent emission are typically around 10^{-20} m^2 and often even higher, cross-sections of Raman scattering are of the order of 10^{-29} m^2 and lower[137,138,139,140]. Therefore, to produce significant signals, high-end sensitive detection methods and a large concentration of the analyte are required. Despite the relatively low cross-sections, Raman spectroscopy has been established as a widely employed analytical tool, especially due to recent advances in both excitation and detection hardware[141]. Overlaps of Raman spectra with fluorescence is another challenge that limits the applicability to non-fluorescent samples or alternatively, requires improving the detection by using higher excitation frequencies.

To understand Raman spectra and to interpret them in terms of modes of molecular vibrations, quantum chemistry methods are used to predict the vibrational modes of molecules. Among many computational quantum chemistry software applications that are used to predict the vibrational modes, the General Atomic and Molecular Electronic Structure System (GAMESS) is particularly popular[142,143,144,145,146].

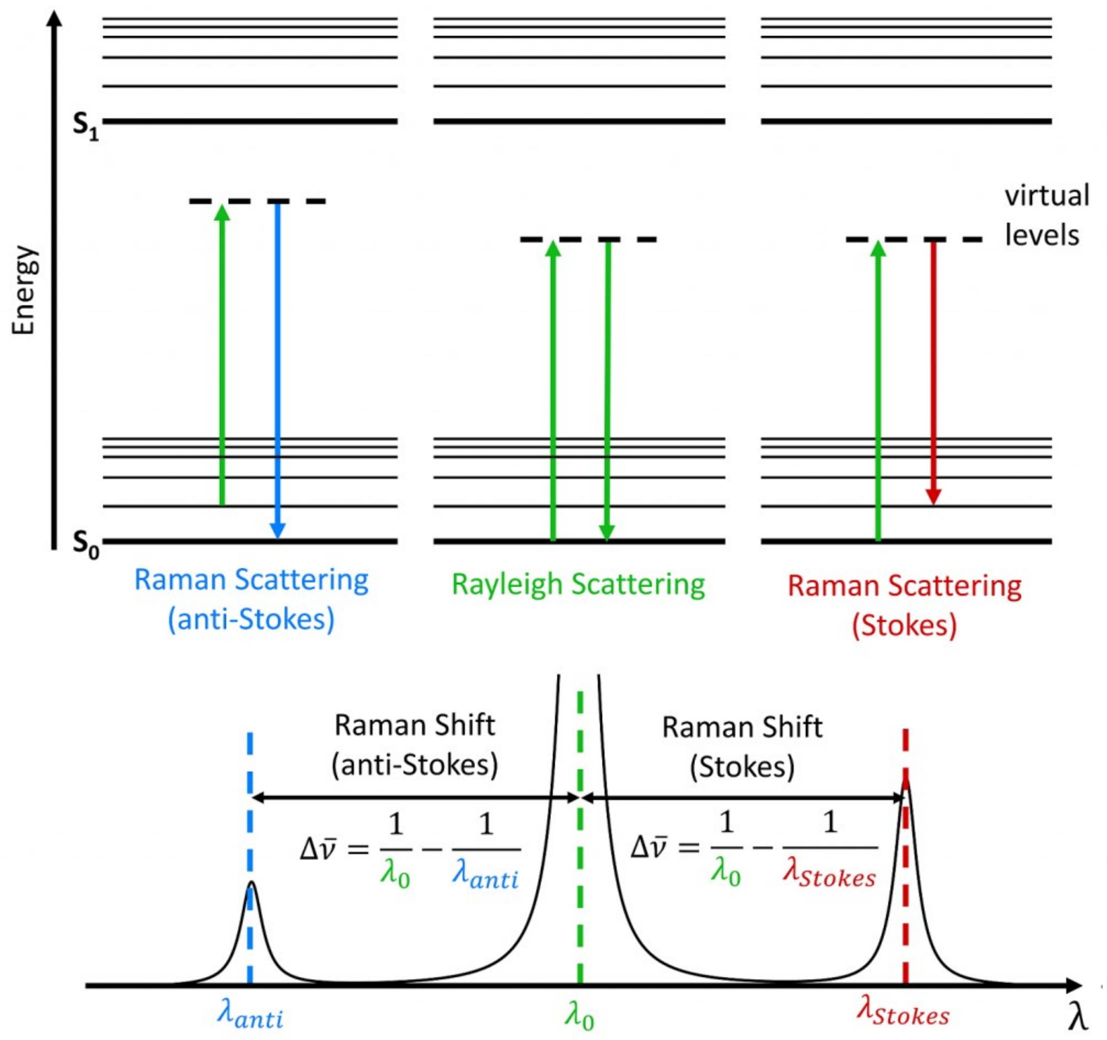

Figure 5: The Jablonski diagram showing the transitions between electronic states for anti-Stokes Raman scattering, Rayleigh scattering, and Stokes Raman scattering[133] (reproduced with permission from Edinburgh Instruments).

A dramatic increase in the probability of Raman scattering near metal surfaces was discovered accidentally by Fleischmann and co-workers in 1974 while doing measurements of Raman scattering for pyridine on silver electrodes[147]. A similar phenomenon was described in 1977 by two independent groups, Jeanmarie and Van Duyne, and Albrecht and Creighton, who observed the enhancement factors of 10^5-10^6, which could not be explained by the Raman effect alone[148,149]. Earlier it was suggested [150] that interaction with roughened metal surfaces might induce resonant Raman scattering from adsorbed molecules. Together, these observations have contributed to the advent of a technique that is currently known as the surface-enhanced Raman spectroscopy, or alternatively surface-enhanced Raman scattering (SERS). It was discovered that the enhancement is due to the interaction of metal-absorbed molecules with plasmonic waves in the nanostructured metal[146], which in particular may include charge transfer transitions in the molecules[151,152]. The interaction between free electrons in the nanostructured metal and the incoming photons results in the generation of plasmonic waves which, in turn, are coupled with vibrational modes of molecules adsorbed on the metal nanostructures. In SERS, the inelastic scattering of photons from adsorbed molecules is enhanced due to the interaction of the molecules with plasmonic waves. It was found that the SERS enhancement depends strongly on electromagnetic fields near the surface of plasmonic nanostructures. This dependence is often referred to as an "E^4 enhancement", due to the fact that SERS enhancement scales approximately as a fourth power of near-field enhancement of electromagnetic fields due to plasmonic oscillations[151]. Although even single nanoparticles of such metals as Au or Ag have been reported to produce SERS effect[153], the strongest enhancement factors, up to 10^9-10^{11}, are achieved when there is an interaction (coupling) of multiple plasmonic nanoparticles[153,154,155]. For example, SERS was used successfully to detect a fluorescent dye, rhodamine 6G, by Le Ru[156], using periodic gold nanostructures that include arrays of dots, squares, and triangles. Although the authors have not reported specific enhancement factors, they showed that the Raman amplification can be controlled by adjusting the gold particles' shape, size and spacing. SERS using similar Ag structures on a silicon wafer were investigated by Gunnarsson[157] for the same target molecule, and they observed improved results compared to nano-roughened Ag film. By creating various Ag structures between

100 and 200 nm in size using electron beam lithography, they investigated how the size and geometry of the structures influences SERS. Measurements using rhodamine 6G on gold periodic nanodot arrays and grating structures have showed an order of magnitude superior SERS enhancement versus metal-island film substrates, as reported by Kahl[158].

Strong enhancement of Raman scattering by plasmonic nanostructures is very helpful to detect small quantities of molecules[135,153,159]. However, near-field electromagnetic enhancement decays with the distance from a nanoparticle's surface[151,156]. This is the reason why SERS enhancement is noticed exclusively in the proximity of plasmonic nanostructures. To achieve a strong SERS effect, the analyte molecules must be located near the surface of the nanostructures, within at least 10-20 nm.

The SERS effect also depends on the excitation wavelength. When the excitation wavelength matches the localized surface plasmon resonance (LSPR) conditions of a nanostructure, resonant near-field electromagnetic enhancement occurs. This causes a considerable increase in the Raman scattering signal. The Mie theory can predict the excitation wavelength that produces LSPR based on the size of the nanostructure.[121,151,159]. In particular, the excitation wavelength for gold LSPR is between approximately 600 and 1200 nm, and that for silver it is between 400 and 1000 nm[153]. When the excitation wavelength does not match LSPR conditions of a nanostructure, the SERS effect is weaker, albeit still present[151,153].

Since LSPR excitation wavelength depends on nanostructures' material, the SERS effect depends on the material as well. Different LSPR excitation wavelength ranges of the often used Au and Ag plasmonic nanostructures can significantly impact their SERS enhancement capabilities[122,123] Ag has stronger plasmonic properties than Au , and therefore Ag nanostructures have a potential of greater SERS sensitivity[160]. However, Au nanostructures are more chemically stable and less reactive than Ag nanostructures. For these reasons, as well as due to better biocompatibility of gold, nanostructures of this material are commonly used for biosensing.

SERS spectra typically represent the intensity of inelastic scattering of light as a function of Raman frequency shifts expressed in cm^{-1}. These spectra carry information about transitions between electronic states of molecules, which are based on the molecule's vibration properties, chemical composition, and interaction with surrounding materials. Importantly, SERS allows capturing Raman vibration signatures of samples in broad frequency regimes, typically from ~300 to 3000 cm^{-1} in a single measurement. This makes possible the simultaneous detection of multiple analytes present in a sample, positioning SERS as a natural fit for multiplex biosensing[161]. Challenges yet to be solved relate to the development of efficient spectrum recognition techniques. Promising roadmaps, currently under intense exploration, include multivariate statistical methods to increase the accuracy of the analysis and machine learning to identify patterns (fingerprints) characteristic of specific compounds in large datasets[162],[163].

2.3.3. Plasmon-Driven Chemical Changes and Detection Combined

Conversion of the energy of light into collective oscillations of electron density accompanied by a buildup of enhanced electromagnetic fields at the interface of a metal and dielectric material results in various physico-chemical effects including local heating and excitation of hot electrons and holes. The last process ultimately may drive photocatalyzed chemical changes in materials located nearby[1,6,7,8,164,166,167,168,170,171,172]. Since the excitation of plasmon waves due to exposure to laser light can both enhance the Raman scattering and induce catalyzed photochemical changes in materials, ultrasensitive in-situ spectroscopic characterization for the induced chemical changes is possible[10,11,12,13,14,165,166,167]. That positions SERS as a unique tool for the investigation of plasmon-driven chemical reactions[168]. For example, Shattique et al[169] have reported SERS detection of a reversible reduction-oxidation process in DNA-bound dye methylthioninium chloride, or methylene blue (MB). To do this, they created a conjugate nanobiological system that links plasmonic gold nanostructures to thiolated single-stranded DNA that carries MB molecules[169]. Exposure of the conjugate system to laser light in buffer solution at a neutral pH resulted in a reversible reduction-oxidation process mediated by surface plasmons, which was monitored in-situ by SERS.

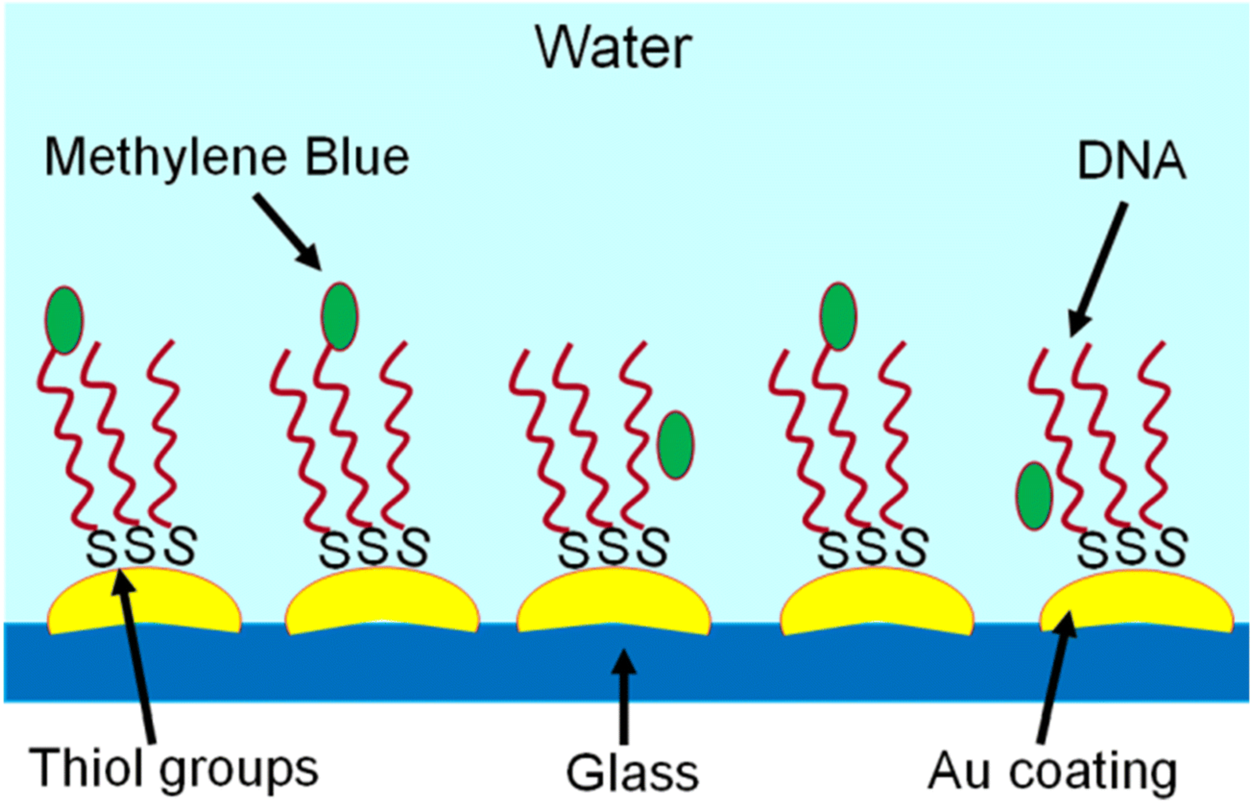

Figure 6: Conjugate nano-biological system comprising a plasmonic substrate (Au-coated glass) decorated with thiolated DNA carrying in MB molecules[169] (reproduced with permission from Springer Nature).

Summarizing, combining SERS ultrasensitive chemical sensing with heterogeneous photo-catalysis at the interface of plasmonic substrates with chemically responsive materials promises unique pathways for selective photo-catalytic synthesis or materials modification[1,6, 170 , 171]. Importantly, most plasmonic substrates that exhibit a strong SERS enhancement are also efficient as photo-catalysts and *vice versa*. This multifunctional nature of nano-plasmonics enables the combination of photocatalytic functions with ultra-sensitive characterization of molecular events within the same device[10,11,12,13,14,172].

2.4. Methods to Fabricate Plasmonic Substrates and Imaging

Various methods have been reported to fabricate plasmonic substrates. For SERS and other nanoplasmonics applications, position and size control is required to achieve the consistency of enhancement of Raman signals[173,174,175,176,177]. The best position control is achieved by employing such techniques as photolithography and direct-write methods to fabricate SERS substrates [178,179,180,181]. In particular, electron beam lithography (EBL) and focused ion beam (FIB) techniques provide superior resolution [182,183,184,185,186,187]. These techniques offer unique abilities to control both the shape and size of the nanostructures, which is critical for achieving high SERS enhancement and sufficient reproducibility of SERS measurements on these substrates[188,189,190,191]. Complementary to direct-write techniques, other methods such as for example, nanosphere lithography[102] or self-assembled metal islands[19] from physical vapor deposition (PVD), are also employed to produce plasmonic substrates; however, validation of their reliability for SERS biosensing and other applications is required[192]. Two direct-write methods, EBL and FIB milling are addressed in greater detail below.

The resolution that may be reached in imaging or patterning employing beams of particles or radiation is fundamentally constrained by the principle of Abbe's diffraction limit. It states that the relationship between a minimal resolvable feature size and the wavelength of the radiation used for this is linear. In other words, the system's resolution improves as the wavelength of light decreases. More specifically, the resolution can be described by the expression[193], $\lambda/(2NA)$, where λ is the excitation wavelength and NA is the numerical aperture of the imaging system. All forms of radiation including electrons, protons, and photons, obey this relationship.

The numerical aperture (NA) of a lens system determines the range of angles over which the system can accept or emit the radiation. Its value varies depending upon the type of lens and application. However, for approximate estimates of the resolution, NA is often assumed to be close to 1 by the order of magnitude. With this assumption, the resolution of optical techniques, such as photolithography, can be estimated as roughly a half of the wavelength of the light. On the other hand, due to the wave-particle duality, particles such as electrons also have a characteristic wavelength. According to the de Broglie relation, a particle's wavelength λ is inversely proportional to its momentum[194],[195]:

$$\lambda = \frac{h}{p} \quad , \tag{1}$$

where h is Planck's constant and p is the linear momentum of a particle (such as electron). For example, the de Broglie wavelength of 20 keV electrons is less than 0.01 nm. This makes it possible to create a highly focused electron beam that could be scanned over a substrate to generate ultrafine patterns. For comparison, in optical projection lithography, the resolution is limited by Abbe's diffraction relation. The often-used deep ultraviolet (DUV) employs exposures of approximately 190-250 nm. For this reason, the ultimate resolution limit of electron beam techniques remains far greater than that of photons-based methods, despite recent improvements of photolithography techniques[196],[197].

2.4.1. Electron Beam Lithography (EBL)

Electron beam lithography (EBL) is a very sophisticated and high-quality tool used for nanofabrication research and development purposes due to its reliability and flexibility in direct writing of sub 10 nm structures, which can be used for both direct lithography and mask generation[198]. The working principle of EBL has similarities with photolithography. In particular, in EBL surface of a substrate is covered with electron-sensitive material (resist) and exposed to a beam of electrons focused to a diameter as small as few nanometers. Inelastic collisions of electrons with the resist cause physico-chemical changes in the resist, which depend on the energy of the electron beam and the number of incoming electrons (exposure dose) on the patterned regions[18,199,]. There are two types of resists used for EBL: positive tone and negative tone resists. After electron beam exposure of positive tone resists, the exposed or patterned parts acquire a greater solubility in developers. In contrast, electron beam exposure of negative tone resists leads to lower solubility properties of exposed parts[200]. Common examples of positive tone resists are polymethylmethacrylate (PMMA)[18,,201], ZEP[202,203] and SML[204]. The positive tone resists contain long chain polymers, and upon exposure of electrons, the polymer chains are broken into smaller fragments making the resist soluble in proper developers[18,]. For negative tone resists, the resists undergo cross linking reactions that create larger structures that become insoluble in developers. The classic examples are hydrogen silsesquioxane (HSQ)[205], Ma-N[206], NEB22 and UVN30[207].

Although the theoretical resolution limit based on de Broglie wavelength of electrons is extremely high, other limiting factors come to play in practical applications of electron beam lithography. First, electron beams undergo electrostatic broadening in the beam and random scattering in the resist as well as backscattering from the substrate[18]. This broadens the area of focus for the electrons and leads to exposure of resist regions that were not supposed to be modified, resulting in less precise patterning. In addition, diffusion and mechanical deformation may occur during resist's development. To minimize these impacts, careful co-optimization of EBL exposures and development is required[18]. With that, EBL can offer a resolution of fabrication down to a few nm[208,209]. Moreover, when applied to fabricate SERS devices, EBL allows flexibility in testing and control over nano-features for differently patterned designs. However, this comes at the expense of slow patterning and long time required for large-area exposures[210,211,212].

2.4.2. Focused Ion Beam (FIB) Milling and Imaging

Focused ion beams are employed for an alternative class of particle beam techniques. In particular, ion beams can be used for imaging of a broad range of materials including metals, semiconductors and dielectrics. The principle of FIB imaging is similar to that of scanning electron microscope (SEM), except that electrons are used in SEM, whereas ions such as He^+, Ga^+ or Ne^+ are employed in FIB. **Figure 7** compares the penetration of focused 30 keV Ga^+ and He^+ ion beams in a substrate to that of 1 keV electrons. Since the interaction volume created by focused He^+ ions beam within the escape depth of secondary electrons is much smaller in comparison with electrons and Ga^+ ions, helium ion microscopy (HiM) provides a better resolution for imaging in comparison to both SEM and Ga^+ ion microscopy. A typical helium ion microscope consists of a sample stage in a vacuum chamber, an ionization source, an ion focusing column, detectors and a gas delivery system[213,214,215,216].

FIB milling employs erosion of surfaces due to sputtering of the impacted surface material. Due to the small interaction area, FIB can be used as an ultrahigh-resolution fabrication tool to produce pits of a diameter less than 10 nm. Furthermore, unlike EBL, there is no need of a mask. Another advantage of FIB milling over electron beam lithography is less proximity effect. When using He+ ions, there is also a gain in resolution. FIB milling with He ions allows creation of pits of 5 nm in diameter. The main limitation of helium FIB is related to relatively longer exposure time and slow patterning[217,218,219], resulting in relatively low throughput. In contrast, the large beam diameter of gallium ions is often considered a disadvantage in terms of resolution, surface damage and contamination due to the ion implantation[220]. However, Ga ions can be used to fabricate larger structures.

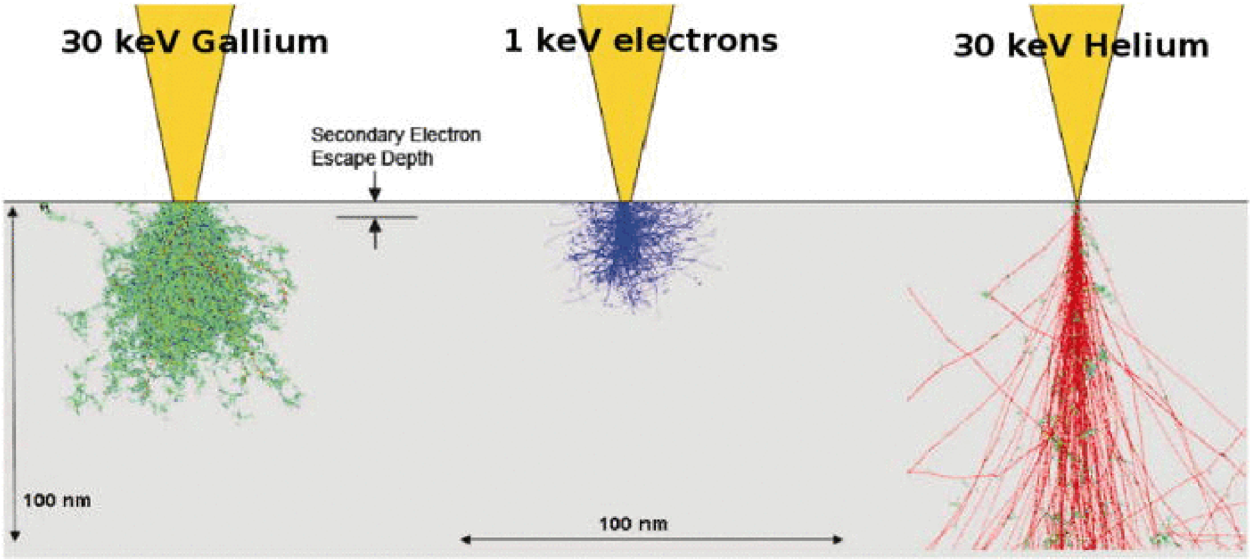

Figure 7: Comparison of the interaction volume of charged particle beams in a Si substrate with the escape depth of secondary electrons used for imaging[221] (reproduced with permission from AIP Publishing).

2.4.3. Challenges of Plasmonic Substrate Fabrication

In the last 15 years, techniques that allow tuning nanostructures' size and shape have undergone rapid development. However, further developments are expected in the upcoming years as nanoplasmonics applications are still in early stages[222]. Due to the enhanced focused and localized fields existing primarily at interfaces between metallic nanopatterns and dielectrics, a significant increase in intensities of SERS have been achieved when metallic nanostructures are fabricated on dielectric substrates. For SERS detection of analytes in solution employing microfluidic channels or chambers, transparent dielectric substrates would be potentially beneficial as well. In particular, fused silica (FS) possesses excellent dielectric properties, a very high transmission, as well as a low background spectrum for SERS imaging in comparison to other substrate materials. However, nanofabrication on dielectric substrates comes with significant challenges. Especially when using EBL, build up of charges during electron beam exposure leads to distortions. Adhesion factors also need to be considered while working with certain common plasmonic metals such Au and Ag on substrates such as glass. To overcome these challenges, special nanofabrication designs are required.

2.5. Objectives of the Work

This research work pursued advancement of both the fabrication of plasmonic nanostructures and their multifunctional usage. The target design of plasmonic substrates included nasnostructures of noble metals on planar dielectric supports which are compatible with both microelectronic and microfluidic settings. The applications focused on SERS detection and characterization of biological compounds in solution. Specific objectives of the work include the following.

- Improvements of existing protocols developed earlier in this group[19] for EBL based fabrication of periodic arrays of Au nanodots on fused silica supports. These included, in particular, the usage of a 10 keV acceleration voltage combined with an improved design for anti-charging coatings when doing EBL exposures of a resist on FS supports in order to fabricate arrays of Au nanodots with a 50 nm pitch.

- Diversification of nanofabrication methods for metallic plasmonic nanostructures. Tests of helium FIB milling for the fabrication of periodic arrays of pits in Au films on FS supports.
- Diversification of plasmonic substrate designs. The target designs included periodic arrays of Au nanodots on FS supports and periodic arrays of Ag nanodots on indium tin oxide supports; the latter in collaboration with Dr. Karthik Shankar's group. In addition, self-assembled Au nanostructures on FS supports created by physical vapor deposition (PVD) method were adopted for some of characterization experiments.
- Diversification of multifunctional nano-biological designs that interface plasmonic substrates with biological materials. The main focus here was on an immobilization of analyte molecules on the substrates via specific binding to dedicated anchor compounds. However, a more flexible design that interfaced a solution containing protein molecules with a plasmonic substrate was also employed to induce and characterize liquid-liquid phase separation in the solution.

3. Equipment

This chapter introduces key instruments used for the research.

3.1. Raith 150^{TWO} EBL Instrument

Figure 8: Image of the Raith 150^{TWO} EBL system (https://raith.com/product/raith150-two/) present at the fabrication and characterization facility nanoFAB, University of Alberta.

The Raith 150^{TWO} (**Figure 8**) is a powerful electron beam lithography tool with ultra high-resolution capabilities. Acceleration voltages are available in broad regimes of 0.1 – 30 keV for both exposure and imaging. This system has a capacity of handling a wafer size from a few mm to 8 inches through a load locking function and provides robust capability of writing features smaller than 5 nm, overlay alignment better than 40 nm, field stitching errors about ~25 nm, and can pattern nanostructures over a wafer with a 150 mm diameter. Furthermore, this tool also allows handling of up to 7-inch masks and doing fixed beam moving stage (FBMS) exposures. Automated wafer scale e-beam writing, focus correction, and beam tracking with increased e-beam stability are available. The system is equipped with an environmentally controlled enclosure.

3.2. Zeiss ORION NanoFab Ion Beam System with Ga^+/He^+ FIB

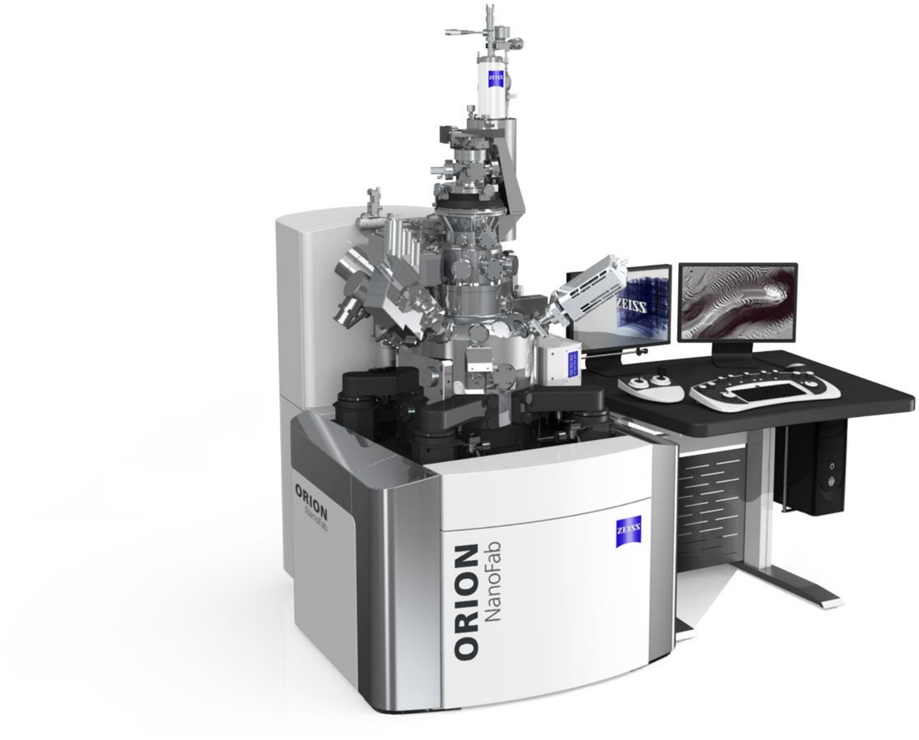

Figure 9: Zeiss ORION nanoFab Ion Microscope (https://www.zeiss.com) present at the University of Alberta.

The Zeiss ORION NanoFab microscope (**Figure 9**) is a unique and powerful tool for both microscopic imaging and nanofabrication employing He^+ and Ga^+ focused ion beams. When the instrument is employed as a helium ion microscope (HiM), it provides large depth of field and superb surface sensitivity with the ion beam energy range from 10kV to 30kV and beam current range from 0.1 to 100 pA. That enables the HiM to provide very high resolution down to sub 0.5 nm on insulating materials and devices. Ultra-high resolution of nanofabrication can be achieved by direct milling (patterning via material removal) or by lithography (resist exposure and pattern transfer). In particular, the focused He^+ ion beam allows milling of very delicate nanometer structures with sizes down to 10 nm with ease, whereas the Ga^+ FIB can be employed for bulk micromachining at larger scales. Moreover, this sophisticated system also provides, direct imaging of insulating materials (no need to prepare the surface), and controlled patterning and imaging by using the NanoPatterning and Visualization Engine (NPVE) software system – an integrated hardware and software control system.

3.3. Scanning Electron Microscopes (SEM)

A scanning electron microscope (SEM) is a type of electron microscope broadly used to visualize surfaces of materials. SEM images of samples are produced by raster-scanning the samples[223] with a focused beam of electrons and measuring the backscattered electron current to provide an image contrast. Information about morphology, orientation of grains, surface topography, and composition of a material can be provided. Crystallographic analysis is also possible. Importantly, SEM provides a very high resolution of imaging down to 1 nm and better. Although traditionally SEM instruments have operated in a high vacuum mode, some of recent systems allow wet conditions (environmental SEM) and variable pressure in the vacuum chamber.

3.3.1. Zeiss SIGMA Field Emission SEM System

Figure 10: Zeiss SIGMA field emission scanning electron microscope (https://www.zeiss.com/microscopy/en/products/sem-fib-sem/sem/sigma.html) present at nanoFAB, University of Alberta.

The Zeiss SIGMA field emission scanning electron microscope (**Figure 10**) is equipped with a dedicated system that allows the SEM tool to offer high quality imaging with excellent surface sensitivity while operating at low kV regimes. Furthermore, this SEM tool is equipped with an in-lens secondary electron (SE) detector and a backscattered electron detector (BSD) to ensure efficient signal detection. In addition, this instrument simultaneously combines energy dispersive X-ray spectrometry (EDS) and electron backscatter diffraction (EBSD) acquisition with the Oxford AztecSynergy system. This provides accurate phase identification and fast mapping. In the present work, this SEM instrument was utilized for imaging of metallic nanostructures on silicon, fused silica and ITO substrates.

3.3.2. Hitachi S4800 Field Emission SEM (FESEM) System

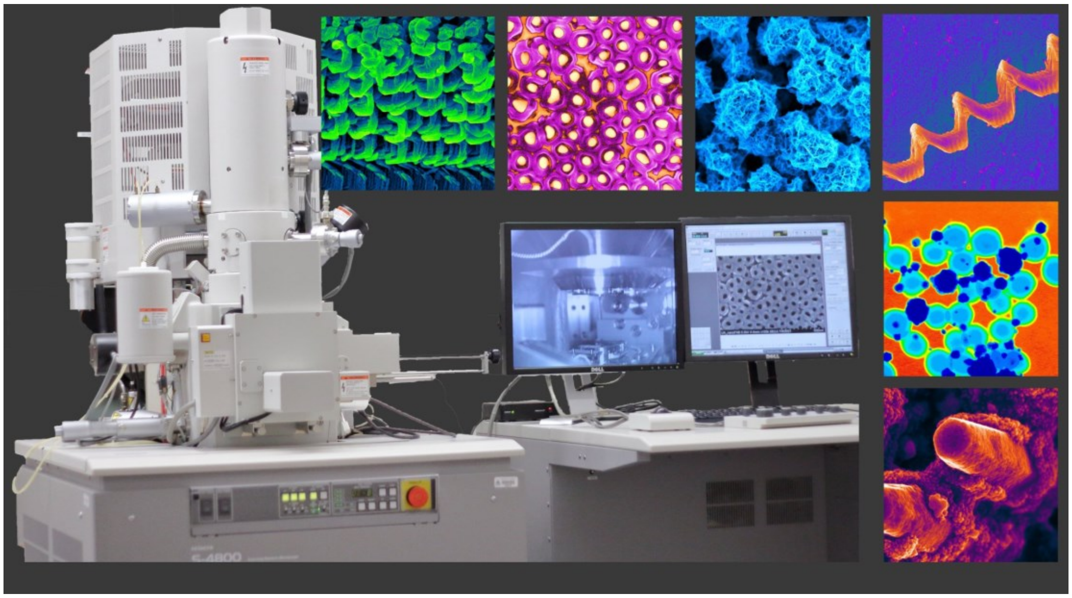

Figure 11: Hitachi S-4800 Field Emission Scanning Electron Microscope (FESEM) system (https://www.hitachi-hightech.com/global/products/science/appli/em/fe-sem/) present at nanoFAB, University of Alberta.

The Hitachi S4800 field emission scanning electron microscope provides a resolution of 1-2 nm depending upon the accelerating voltage (**Figure 11**). This FESEM system is configured for imaging with different detectors for secondary and backscattered electrons and is equipped with a cold field emission gun (c-FEG). These detectors can be used in parallel for visualization of both surface morphology and composition of the sample. Additionally, the Hitachi FESEM system's cryo-holder is cooled down by employing liquid nitrogen for better stability and resolution.

3.4. Renishaw inVia^{TM} Confocal Raman Microscope

Figure 12: Renishaw InViaTM Raman Microscope (https://www.renishaw.com/en/invia-confocal-raman-microscope--6260) present at the nanoFAB, University of Alberta.

The inVia Qontor confocal Raman microscope (**Figure 12**) is a powerful and flexible Raman instrument with the capabilities of focused analysis of samples in both two and three dimensions. Various surfaces i.e. smooth, rough, flat or round can be probed. This instrument is well suited for both microscopy and macro-imaging as it is equipped with four objective lenses: 5X, 20X, 50X, and 100X. Three lasers with excitation wavelengths of 532 nm (50 mW), 633 nm (17 mW) and 785 nm (300 mW) are available. The instrument allows the user to identify the regions on a substrate which are providing the highest Raman signal. Importantly, this Raman microscope is equipped with the LiveTrack^{TM} focus tracking technology that automatically maintains optimum focus during data collection. All the features combined provide a high signal throughput, high spectral resolution, high sensitivity and stability.

3.5. Kurt J. Lesker Electron Beam Evaporator and PVD Method

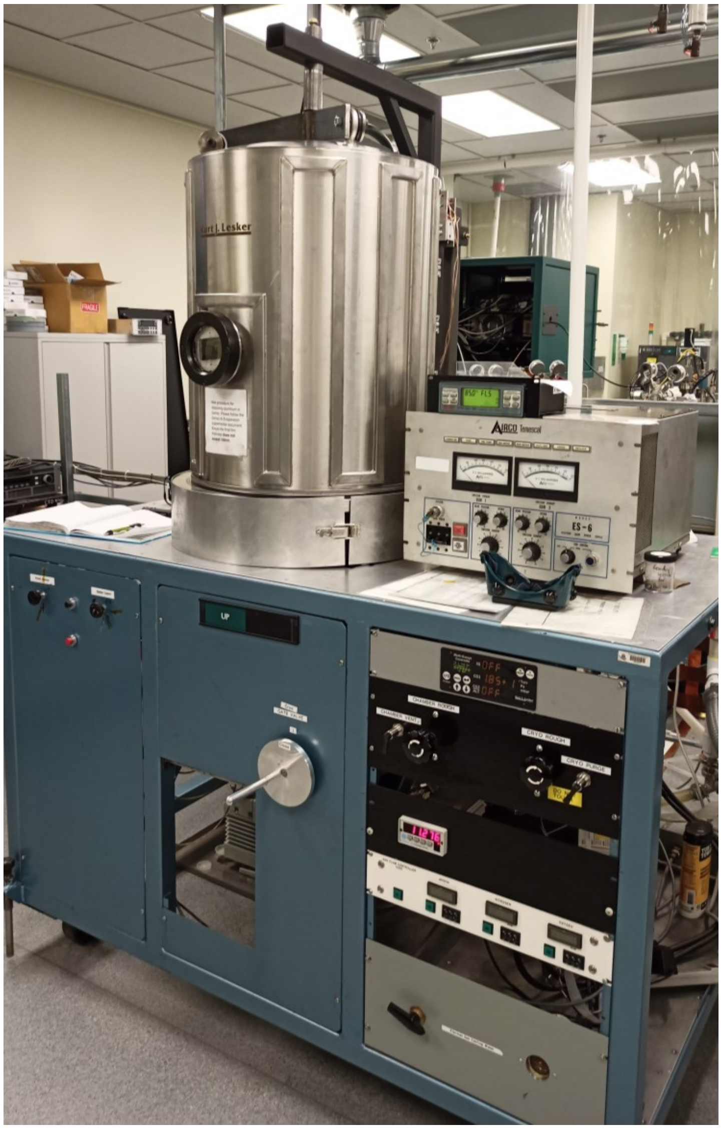

Figure 13: Kurt J. Lesker electron beam evaporator (GOMEZ) (https://www.lesker.com/) present at the nanoFAB, University of Alberta.

A Kurt J. Lesker electron beam evaporator (**Figure 13**) is used for physical vapor deposition (PVD) of a variety of materials via the electron beam heating process. This e-beam evaporator has 4 pocket holders for loading of 4 crucibles that allow deposition of multiple layers of different materials. The base pressure can go below $7x10^{-5}$ Pa ($5x10^{-7}$ Torr) within 1 hour. The crucibles' cooling system provides a uniform temperature gradient within the metal, allowing for a consistency between deposition runs and minimum contamination by the crucible material.

The instrument comprises a bell jar shaped to improve directionality in the deposition instrument with a significant distance between the sample holder and the metal crucible. Electron beam evaporation is a "line-of sight" process where atoms travel from the source to the sample in a straight path and only can reach locations in direct view with no obstacles along the path[224],[225]. Directionality is particularly important when this technique is used for metallization of high-aspect-ratio EBL resist patterns, when a possibility of "flagging" may interfere with subsequent liftoff and negatively impact the ultimate resolution of the patterning process. "Flagging" is unwanted retention of metal when lift-off does not occur properly. This may happen when the edges of resist are covered by metal without a gap between the metal on top of the resist and the metal on the substrate[226]. To prevent "flagging", re-entrant profiles can be used. A re-entrant profile is a resist pattern that has undercuts or is concave-shaped. Such a shape can help to prevent edges of the resist from metallization. Concavity or undercuts often arise naturally after development of EBL resists, especially when the resist was exposed with low-kV electrons beams that broaden due to scattering[18]. Alternatively, double layer resists can be used to create undercuts. A double layer resist involves depositing a second layer of lower sensitivity resist material on top of the first layer, which can help to hold the edges of the resist pattern in place[226,227].

When fabricating high-resolution nanostructures, it is important to carefully choose the deposition technique out of many available options. Alternatively to line-of-sight electron beam deposition, conformal coating methods such as, for example, chemical vapor deposition (CVD) produce a uniform film over the entire surface of 3D features without requiring a direct-view geometry[225,228]. Although conformal CVD methods are used broadly for uniform coating of high-aspect ratio 3D nanostructures, they are not suitable for metallization of EBL resists. For this reason, the Kurt J. Lesker's PVD system was employed for metallization in the present work.

3.6. Brewer's Cee 200X Spinner and Cee 1300X Hotplate

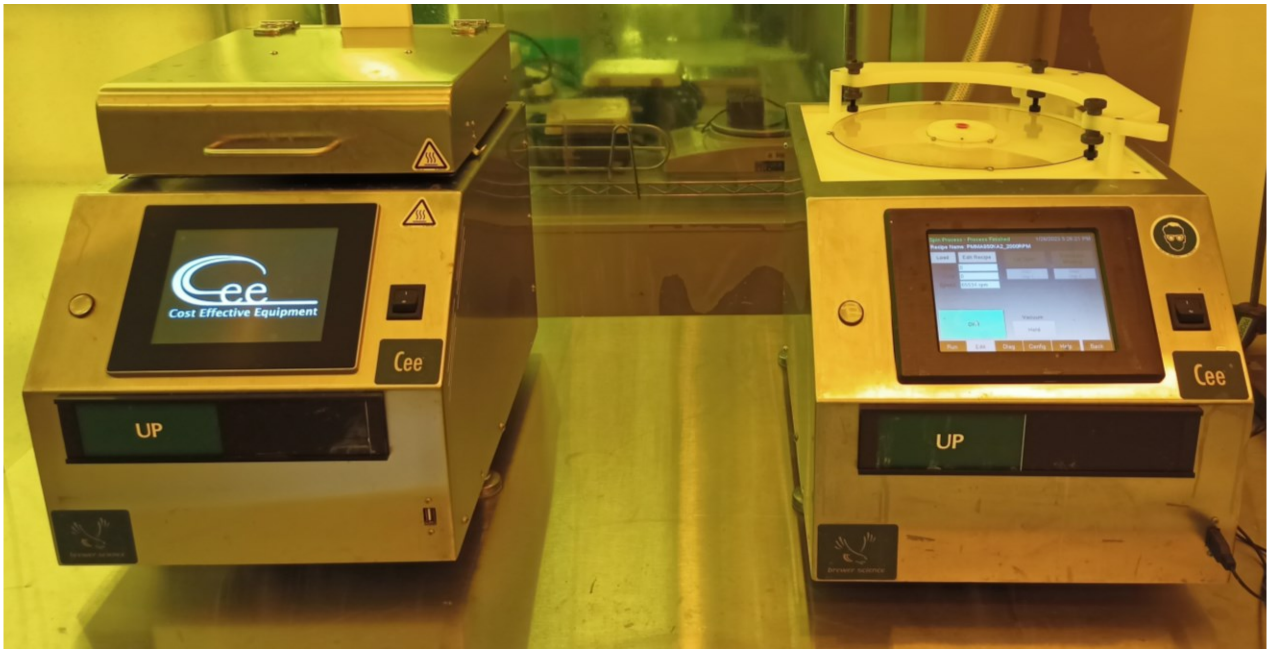

Figure 14: Brewer Science Cee 1300X hotplate (left) and Cee 200X spinner (right) (https://www.brewerscience.com/) present at the nanoFAB, University of Alberta.

The Brewer Cee 200X spinner is used for spin-coating the samples at a high spin speed up to 10,000 rpm and fast ramp rates with a high torque. The consistency in the thickness of spin-coated resist is enhanced due to the top cover design of the spinner. The Cee 1300X hotplate is used for baking samples right after the spin-coating. The top cover of the hotplate also helps in providing the consistency in baking the resists samples. **Figure 14** illustrates the spinner and the hotplate at the University of Alberta's nanoFAB.

3.7. J.A. Woollam M-2000V Spectroscopic Ellipsometer

Figure 15: J.A. Woollam M-2000V spectrometric ellipsometer (https://www.jawoollam.com/products/m-2000-ellipsometer) present at the nanoFAB.

Ellipsometry is an optical technique that is used to measure the thicknesses of thin films and characterize surface roughness through measurements of dielectric properties of materials. The J.A. Woollam M-2000V ellipsometer (**Figure 15**) offers fast data acquisition, wide spectral range, and an advanced optical design. The spectral range of 370-1000 nm comprises 390 wavelengths that can be measured at different angles of incidence. In particular, the instrument can determine the thickness of a polymer coating on opaque substrates such as silicon with a 0.01 nm accuracy, and on transparent substrates such as fused silica with a 10-20 nm accuracy.

4. Results and Discussion

4.1. Fabrication of Plasmonic Nanostructures

This research work pursued the fabrication of periodic arrays of plasmonic Au and Ag nanostructures on two dielectric substrates: fused silica (FS) and indium tin oxide (ITO). Electron-beam lithography (EBL) was used as a primary nanofabrication method. For comparison, Si substrates were also employed in some EBL designs. To broaden the nanofabrication capabilities, the helium FIB milling was employed to fabricate periodic arrays of pits in Au layers on FS substrates. In addition, self-assembled Au nanostructures on FS substrates were created by the physical vapor deposition (PVD) method to perform some of characterization experiments.

4.1.1. EBL Fabrication of PMMA Masks on FS, Si and ITO Substrates

Nanostructured masks consisting of periodic arrays of dots (pits) in a layer of positive tone electron-beam resist polymethylmethacrylate (PMMA) on FS, ITO, and Si substrates were fabricated over an area from approximately 2,500 μm^2 to 14,400 μm^2 using EBL. The EBL fabrication of PMMA masks on FS substrates included the following steps: (1) deposition of PMMA resist and an anti-charging layer of a conductive polymer on the substrate via spin-coating; (2) electron beam lithography exposure; (3) removal of the conductive polymer; and (4) removal of soluble regions of the resist (development) as shown in **Figure 16**. In contrast to the FS substrates, the fabrication of PMMA masks on ITO and Si substrates did not require an additional conductive coating on top of the PMMA resist due to the inherent conductivity of the substrate.

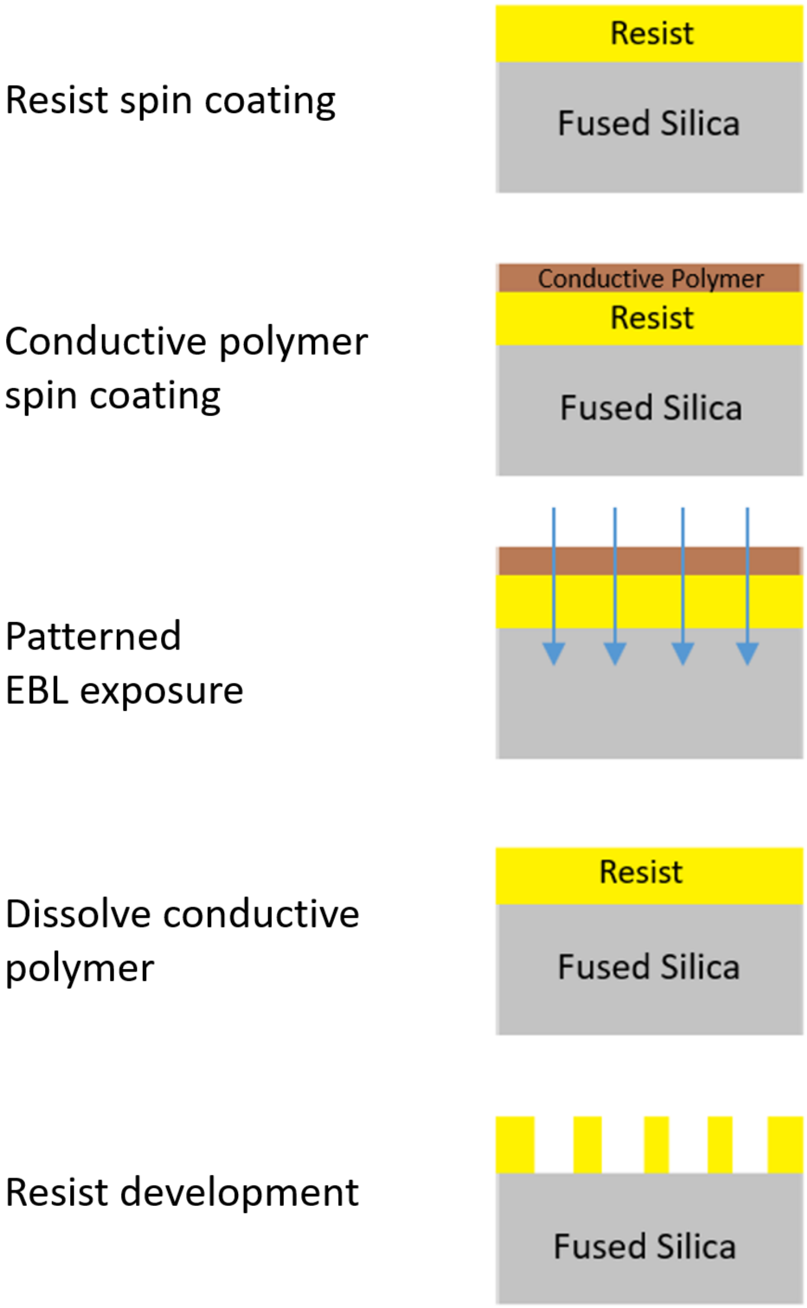

Figure 16: Nanofabrication scheme for PMMA masks on FS substrates using EBL.

To prepare the samples for EBL exposures, the FS and Si substrates were cleaned in piranha (H_2SO_4:H_2O_2, 3:1) solution. The ITO substrates (from Guluo Glass) were provided by Navneet Kumar (Dr. Karthik Shankar's group). The ITO substrates were rinsed with de-ionized (DI) water and then placed in a sonication bath with acetone and methanol solutions for 10 minutes each. The cleaned substrates were spin-coated with a 90 nm layer of PMMA 950K A2 resist. To avoid degradation of the writing pattern during EBL exposures on FS substrates, an additional 60 nm thick protective layer of water-soluble conductive polymer Electra 92 (Allresist GmbH) was applied on the top surface of PMMA as schematically shown in **Figure 17**(a). As already mentioned, in the case of Si and ITO substrates, no anti-charging layer was needed on top of PMMA. The corresponding samples after spin-coating are shown in **Figure 17**(b, c). The thicknesses of both PMMA and Electra 92 layers were verified using a J.A. Woollam VASE® Ellipsometer, M-2000V (Section 3.7).

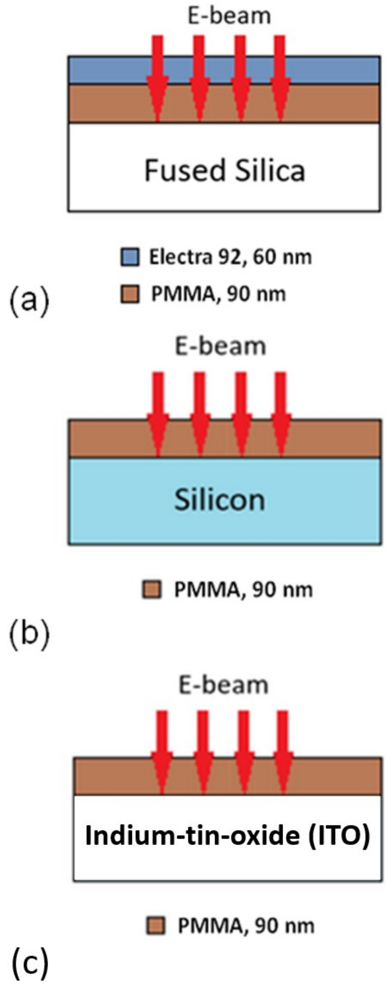

Figure 17: (a) – Scheme of samples for EBL fabrication of periodic arrays of dots in PMMA on FS (a), Si (b), and ITO (c) substrates.

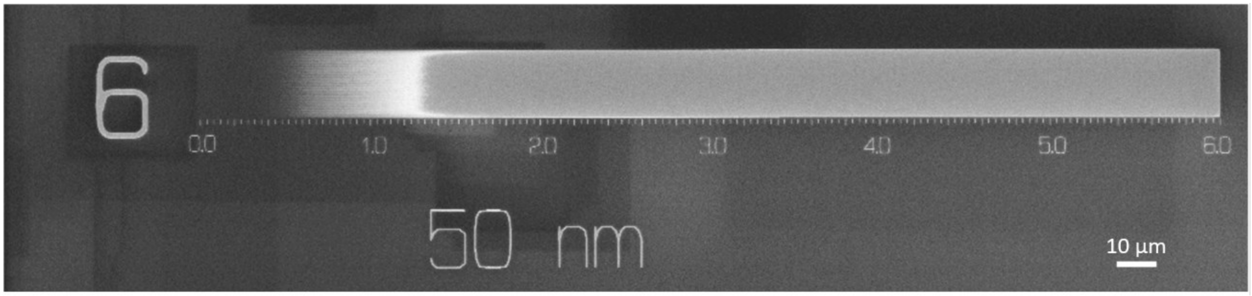

Figure 18: SEM image of dose gradient testing bar for a periodic array of single-pixel dots with a 50nm pitch in PMMA.

For EBL exposures, the Raith 150^{TWO} instrument (Sect. 3.1) was employed. A relatively low accelerating voltage of 10 keV was selected to achieve a greater sensitivity. An optimal exposure dose of 2.7 fC/dot was identified from a dose gradient test for the periodic pattern consisting of 50 nm pitch dots in PMMA as illustrated in **Figure 18**. Following the EBL exposure of the samples on FS, the conductive layer was removed by placing the samples into deionized (DI) water for 60s. The samples on Si and ITO substrates did not require additional conductive coating, whereas the other process steps were the same. The samples were developed during 20s in a solution of isopropanol with water (IPA:water, 7:3) followed by rinsing in IPA for 10s at ambient temperature. The resulting pattern in PMMA of a FS substrate after development is presented in **Figure 19**(a). For comparison, similar 50 nm pitch arrays of dots fabricated in PMMA on Si and ITO substrates are shown in **Figure 19**(b, c).

As can be seen in **Figure 19**(a), EBL nanopatterning with a 10 keV accelerating voltage allows the fabrication of high-quality periodic arrays of dots with a 50 nm pitch in PMMA on FS supports. To fabricate this periodic pattern, a 60 nm thick conductive coating of Electra 92 polymer was applied on top of the PMMA resist. Exposure doses from 2.1 fC/dot to 2.7 fC/dot were required to produce a successful periodic pattern in PMMA under these conditions. This exposure dose window is close to the doses of 2.4-3.0 fC/dot employed earlier to fabricate arrays of dots with a similar 50 pm pitch in PMMA on fused silica supports using a different conductive polymer, aquaSAVE (Mitsubishi Rayon) with a 30 keV accelerating voltage[19,229,230]. Also, the required EBL exposure doses are 2.5-2.9 times higher than the doses of 0.72-1.10 fC/dot needed to fabricate 50 nm pitch dots in PMMA on Si substrates without the conductive layer with a 10 keV accelerating voltage (see **Figure 19**(b)). To better understand the reason of the difference, the EBL simulator developed earlier[231,232] was used to calculate the yield of main-chain scission in PMMA with and without the Electra 92 coating. **Figure 20**(a) and **Figure 20**(b) present cross-sections of the predicted 3D scission patterns in the periodic, 50 nm pitch arrays of dots for the samples' designs as depicted in **Figure 19**(a) and **Figure 19**(b), respectively. The exposure doses and other conditions used in the simulations matched the experimental settings. As can be seen in **Figure 20**(a), the 10 keV electron beam undergoes a significant broadening and absorption when it travels through the layer of conductive polymer before reaching the PMMA resist. This broadening may explain the relatively high exposure doses required to fabricate the dots in the Electra 92 coated samples with 10 keV accelerating voltages. Nevertheless, the broadening of the electron beam has not prevented the fabrication of high-quality periodic arrays of nanodots in PMMA. Unlike different anti-charging schemes reported earlier[19,231,232], the usage of Electra 92 conductive coating has allowed the fabrication of highly regular 50 nm pitch dots in PMMA on fused silica substrates using electron beam exposures with relatively low accelerating voltages of 10 keV. Although this comes at the expense of certain loss in sensitivity in comparison to similar nanopatterning on Si supports without the conductive coating, the capability to fabricate periodic arrays of nanodots in PMMA on dielectric supports is instrumental for the subsequent fabrication of plasmonic nanostructures.

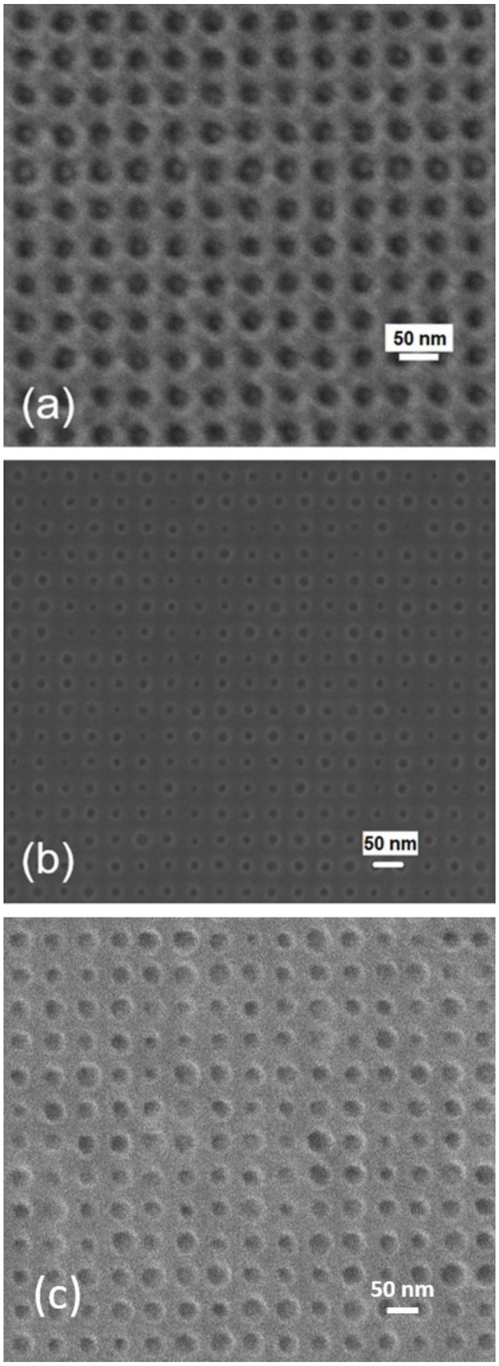

Figure 19: (a) – HIM image of an array of 50 nm pitch dots (pits) in PMMA on a FS substrate after a 10 keV, 2.7 fC/dot exposure, subsequent development and deposition of 10 nm layer of Au; (b) – SEM image of a similar array in PMMA on Si after a 10 keV, 1.0 fC/dot EBL exposure and subsequent development; (c) – HIM image of 50 nm pitch arrays of dots in PMMA on ITO substrate with exposure dose at 0.96 fC/dot right after the development.

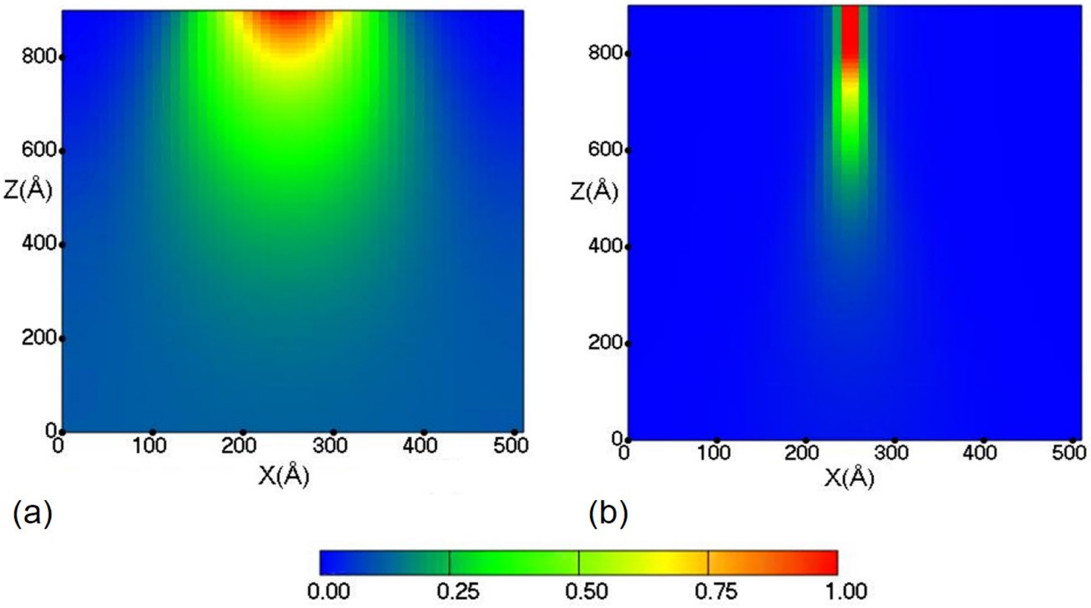

Figure 20: Simulated[231,232] yield of main-chain scission per monomer for a periodic dot array with a 50 nm pitch, in 90 nm thick PMMA resist on a FS substrate with a 60 nm coating of Electra 92 (a) and on a Si substrate (b) without additional coating, using a 10 keV accelerating voltage and the dose of 2.7 fC/dot (a) and 1.0 fC/dot (b). In the images, X is width and Z is depth in the PMMA layer. The legend bar annotates the yield of main-chain scission.

In order to fabricate similar 50 nm pitch arrays of nanodots in PMMA on ITO substrates, the exposure dot doses were tested through the EBL simulator[231]. According to the simulations, the predicted optimal exposure dose for ITO substrates is approximately 1.0 fC/dot, which is close to the corresponding optimal dot dose for the Si substrate, as shown in **Figure 21**. Subsequently, the doses were tested experimentally using the gradient dose bar presented in **Figure 18**. According to the experiments, the exposure doses required for the fabrication of the 50 nm pitch arrays of dots were in the range of 0.6 – 1.20 fC/dot, with an optimal dose about 0.95 fC/dot. A pattern exposed at a dose of 0.96 fC/dot is shown in **Figure 19**(c). Therefore, both the experiments and the simulations indicate that the optimal exposure doses are similar for Si and ITO substrates.

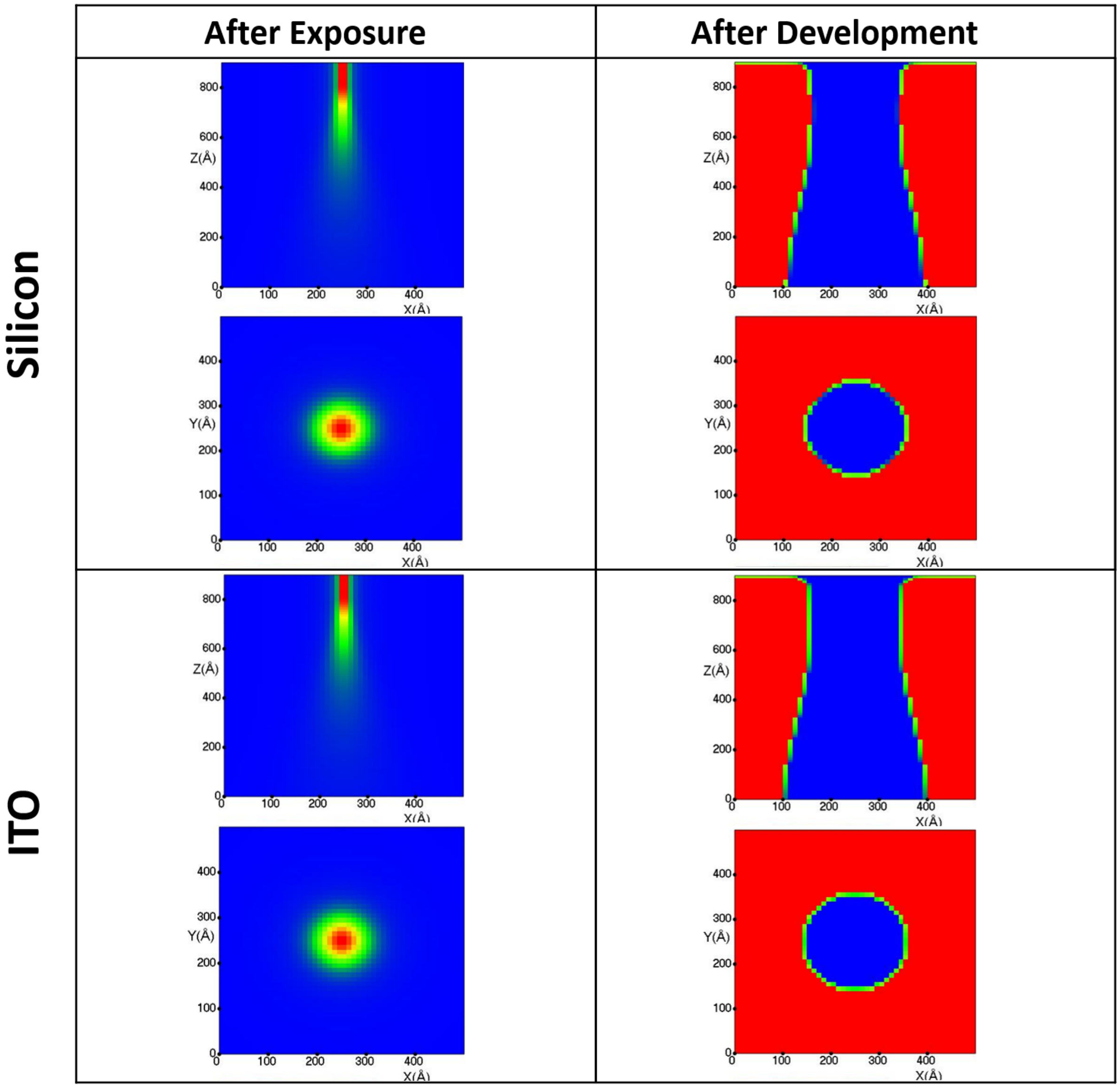

Figure 21: The EBL simulation[231] results for main-chain scission yield after exposure (left) and for clearance profiles after development (right) in a 90 nm thick PMMA resist on Si and ITO substrates. For EBL exposures, 10 keV accelerating voltage was used with the dose rate of 0.9 fC/dot for Si and 1.0 fC/dot for ITO. The development conditions were as in the experiments. For the scission yield (left), the color coding is as in **Figure 20**. For the clearance profiles (right), red color indicates the remaining resist and blue color shows the locations where the resist is removed.

4.1.2. Fabrication of Plasmonic Nanostructures Using PMMA Masks

The patterned PMMA was used as a mask to fabricate periodic 50 nm pitch arrays of Au nanodots on FS supports. For this purpose, a 10 nm layer of Au was deposited on top of PMMA by electron evaporation using a Kurt J. Lesker system (Sect. 3.5). The samples were subsequently immersed in acetone for 10 minutes and then lift-off was performed by sonication in acetone for 1 min to remove the PMMA and overlying Au as illustrated in **Figure 22**. The resulting array of Au nanodots with a 50 nm pitch on a FS substrate is shown in **Figure 23**. The fabricated arrays contained 1000x1000 Au nanodots in total.

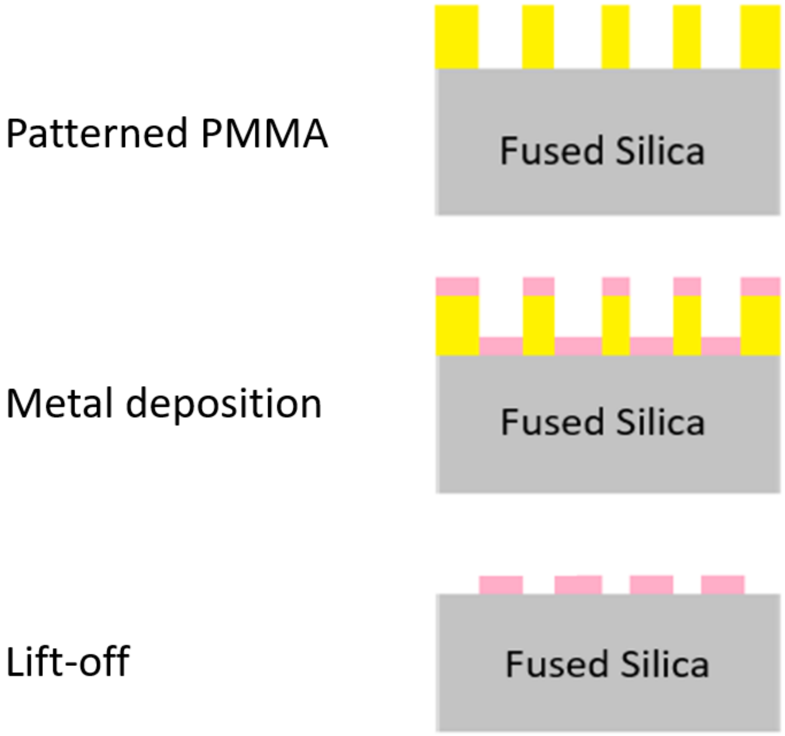

Figure 22: Illustration of the metallization and liftoff steps to obtain periodic arrays of Au nanodots on FS substrates where yellow color shows the PMMA resist and pink color represents Au metal.

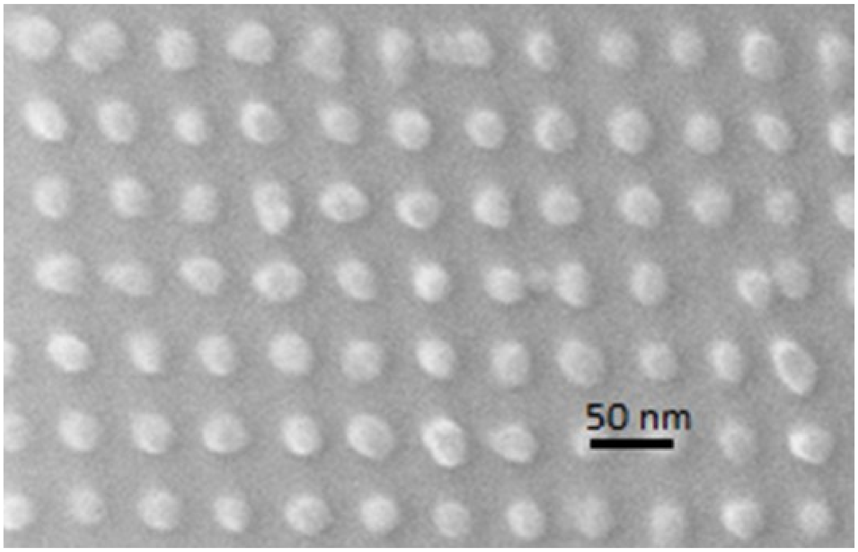

Figure 23: HIM image of a 50 nm pitch square array of 1000x1000 Au nanodots on FS.

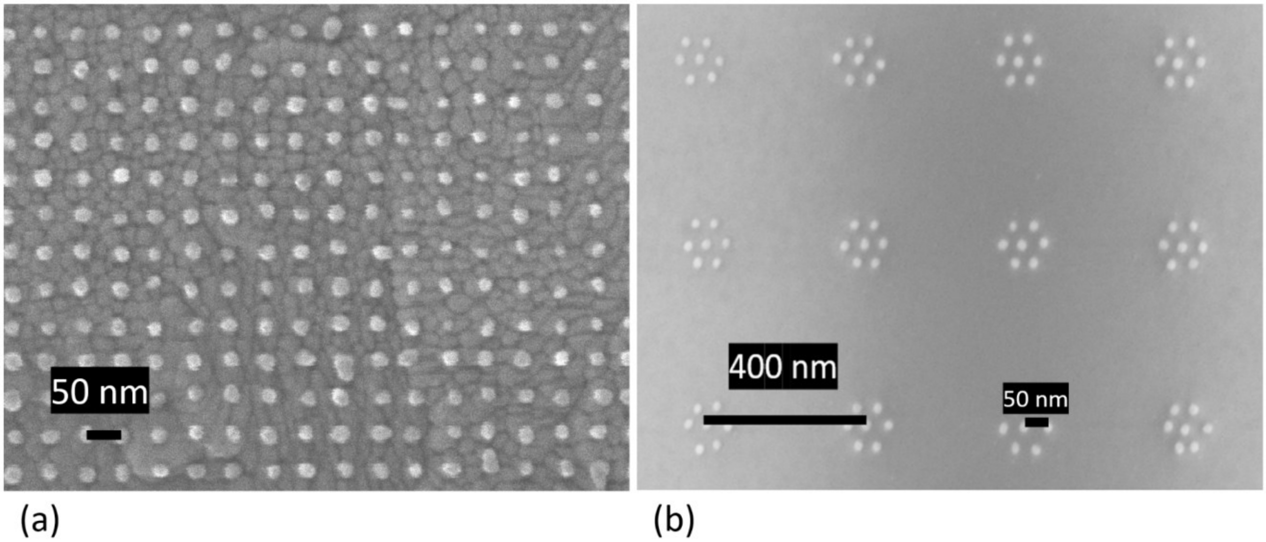

Figure 24: (a) – HIM image of a periodic 1000 x 1000 array of Ag nanodots with a 50 nm pitch on an ITO substrate; (b) – SEM image of a periodic 120 µm x 120 µm array of Ag nanodot heptamers with a 400 nm pitch and a 50 nm distance between the dots within each heptamer (also on an ITO substrate). To fabricate the corresponding PMMA masks, the exposure dose rates of 1.04 fC and 1.2 fC were used, respectively.

In a framework of our collaboration project with Dr. Karthik Shankar's group, arrays of plasmonic nanostructures on the ITO-substrates were fabricated following similar procedures. Specifics of this collaboration required Ag nanopatterns in place of Au. A 10 nm layer of Ag metal was deposited over PMMA masks on the ITO substrates using electron evaporation; the Ag-coated samples were placed in an acetone-filled beaker for 10 minutes; and then lift-off was performed by sonication in acetone for 1 min. **Figure 24** illustrates two designs, a simple square array of Ag nanodots at 50 nm pitch (a) and a periodic array of heptamer structures with a 50 nm inter-dots distance and a 400 nm pitch (b). Large arrays extending 120 µm x 120 µm were created for the heptamer structures for future testing.

4.1.3. Improved Protocol of EBL-Based Nanopatterning on Dielectric Substrates

Initially, the protocol developed in the group earlier[19] was selected for the EBL-based fabrication of nanostructures on dielectric substrates. However, modifications of the protocol have been required in the course of the work. As described in Sect. 4.1.1, new conductive polymer, Electra 92, was employed for anti-charging protection during EBL exposures instead of AquaSAVE. The replacement of the conductive polymer was required due to its availability. As a consequence of somewhat lesser sensitivity of the new conductive polymer, a decrease of the accelerating voltage from 30 keV to 10 keV was required in order to efficiently pattern the PMMA masks. Development and testing of the corresponding protocols, as described in Sect. 4.1.1 and 4.1.2, resulted in the first successful fabrication of periodic 50 nm pitch arrays of dots in PMMA on FS supports using 10 keV EBL exposures achieved in this group. In addition, details of sample preparation and processing at the University of Alberta's nanoFAB have undergone adjustments in response to the evolution of available instruments and procedures. The updated nanofabrication protocols for plasmonic nanostructures are listed below.

1. Substrate preparation

i. The Disco DAD 3840 dicing saw is used to cut the fused silica or silicon wafers accurately and precisely into samples of approximately 1 cm x 1 cm size.

ii. The samples are cleaned in piranha (H_2SO_4:H_2O_2, 3:1) solution bath for 15-20 min, rinsed with DI water, and dried with nitrogen.

iii. The samples are placed on the Cee 1300X hotplate (Sect. 3.6) at 180° C face up for 3 min until they cool to the room temperature (RT).

2. Spin coating of the resist and conductive layer on the substrate and baking

i. The sample is placed on the Brewer Science Cee 200X spinner (Sect. 3.6) and centered on the vacuum chuck. A drop of PMMA resist is put on the center of the sample using a glass pipette. The sample is spun for 60 sec at 3500 rpm with a ramp time of 2 sec.

ii. The PMMA coated sample is baked for 3 min at ~180° C. After baking, the sample is allowed to cool down to RT.

iii. After baking and cooling of the PMMA coated sample, the sample is put on the vacuum chuck of the spinner again. A drop of conductive polymer Electra 92 is put on the center of the sample, and the sample is spun at 2000 rpm for 60 sec.

iv. The sample is put on the hotplate at 90° C for 2 min, and then let to cool down at RT.

Note: Prior to baking, it is beneficial to first clean the entire support wafer of silicon in the hotplate with isopropanol and dry the wafer with nitrogen. Then, the silicon wafer is placed back on the hotplate. As soon as the temperature of the wafer has reached ~180° C, the sample can be put on top of the silicon wafer.

3. EBL exposures

i. The substrate is loaded into the Raith 150^{TWO} EBL system's chamber (Sect. 3.1). For convenience, leaving a very fine mark from the bead edge pen is helpful for focusing and finding where the pattern will be exposed.
ii. The required focusing, aperture control and stigmation adjustment are performed to obtain the circular carbon dot of < 30 nm. If the exposed carbon dot diameter is less than 30 nm and completely circular, the write field alignment is done, and exposure of the pattern can be performed.

4. Removal of conductive polymer and development of exposed samples.

i. Firstly, a beaker is filled up with DI water. Exposed samples are placed in the beaker for 60 sec for the removal of conductive polymer Electra 92.
ii. A second beaker is filled with the developer mixture (IPA:H_2O, 7:3) and the mixture is stirred for 5 min at RT. Also, a third beaker with a high purity isopropanol solution is prepared.
iii. The samples are placed in the second beaker, where they are moved clockwise and counter clockwise using tweezers for 20 sec. The samples are immediately transferred into the isopropanol, and rinsed for 10 sec by moving the samples up and down using tweezers. Then, the samples are dried with nitrogen.

5. Metallization and liftoff

i. The samples are loaded into the Kurt J. Lesker electron beam evaporation system (Sect. 3.5) upside down along with an Au or Ag metal crucible to create a layer of evaporated metal on the front face of the sample. A 10 nm thick layer of Au or Ag is deposited at a rate of 0.3-0.4 Angstrom/sec and 0.5–0.6 Angstrom/sec, respectively.

ii. A beaker with acetone is put into the sonication system. The sonication bath is filled with water such that the level of water matches the level of acetone. The sample is placed into the acetone beaker for 10 min holding the sample with tweezers and moving it clockwise and counter clockwise after every 2 ½ min. Then, the sonication system is turned on for up to 60 sec.

iii. The samples are rinsed with isopropanol immediately after the sonication. It is highly recommended to clean the samples with DI water as well. Then, the samples are inspected in the optical microscope to verify that the liftoff process was successful. If required, the sonication bath processing is repeated.

The described EBL protocols for fabrication of periodic arrays of nanodots on FS substrates require the usage of a conductive polymer, such as e.g. Electra92, as well as adjustment of accelerating voltage and optimizing of exposure dosage depending upon the sensitivity of the conductive polymer. Nevertheless, the developed EBL protocol provides sufficient positional control and resolution to fabricate high-quality periodic arrays of approximately 25 nm sized noble-metal dots with a 50 nm pitch on dielectric substrates.

4.1.4. Fabrication of Plasmonic Nanostructures Using FIB Milling

Complementary to arrays of noble-metal nanodots, periodic arrays of nanopits or nanopores have been reported to exhibit plasmonic properties[164,176,179]. In order to broaden the capabilities to fabricate plasmonic nanostructures, helium FIB milling was employed to drill arrays of pits directly in a layer of Au at a surface of a dielectric substrate.

For this purpose, piranha-cleaned FS substrates were coated with 50 nm and 10 nm films of Au using the Kurt J. Lesker electron evaporation instrument. Based on previous user experiences of effective parameters for similar materials to achieve required milling depth, the accelerating voltage of 25 keV was employed for the helium FIB exposures. A beam current of 1.27 pA with the dot dose of 2.00 pC was used for the 50 nm thick layer of Au, and a beam current of 0.791 pA with the dot dose of 0.5 pC was used for the 10 nm layer of Au on a FS substrate. The optimum working range of dot doses was found to be from 0.80 pC to 0.32 pC for a 10 nm layer of Au.

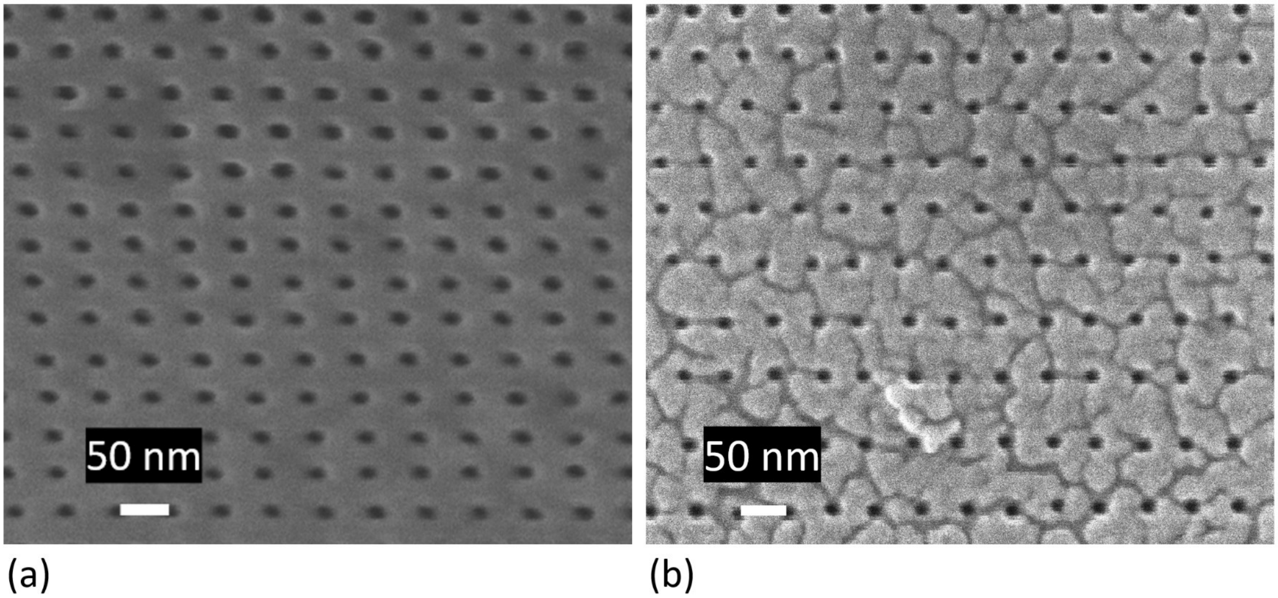

Figure 25: HIM microscopy images of periodic arrays of nano-pits with a 50 nm pitch fabricated by helium FIB milling of a 50 nm thick Au layer on a FS substrate (a), and a 10 nm Au layer on a FS substrate.

Figure 25 presents periodic arrays of pits with a 50 nm pitch fabricated in a 50 nm thick Au film on a FS substrate (a) and in a 10 nm thick Au film on a FS substrate (b). High quality arrays of pits with 15-20 nm diameters were fabricated in both samples. Importantly, there is no need for additional anti-charging layers during the He-FIB exposures, since the Au film itself plays the role of the protective layer reducing the dispersion of the ion beam and increasing the accuracy of the patterning. However, the time required to fabricate an array of 99 x 99 pits in a 10 nm Au film on FS was about 7 hours and 17 min. For comparison, it will only take around 50 sec to write a similar array of dots in PMMA by EBL. It was concluded that, although the He-FIB milling offers superb accuracy, heavier ions might be required to increase the efficiency of the FIB fabrication of plasmonic nanostructures.

4.2. Bio-functionalization and Testing of Plasmonic Substrates

4.2.1. Testing of Au Nanodots on FS Supports

To verify the performance of the fabricated arrays of 50 nm pitch Au dots on FS (**Figure 23**) as plasmonic substrates, SERS biodetection was attempted. For this purpose, an important inflammation marker was targeted, protein interleukin-6 (IL-6)[233]. The molecular structure of IL-6 is shown in **Figure 26**. The Au/FS substrates were bio-functionalized with thiolated DNA aptamers that bind specifically to IL-6[234]. Upon binding to Au nanodots via thiol groups, the DNA aptamers were loaded with the IL-6 protein to obtain a monolayer of the IL-6/DNA complex immobilized on Au dots in solution as illustrated in **Figure 27**.

Lyophilized ActiveMax® human IL-6 protein was purchased from ACROBiosystems and reconstituted in a Tris-EDTA buffer (pH 7.9) to a solution of 4.8µM. Lyophilized IL6-binding, thiolated DNA aptamer 5’-/5ThioMC6-D/ GG TGG CAG GAG GAC TAT TTA TTT GCT TTT CT[234] was procured from Integrated DNA Technologies Inc. and reconstituted in the buffer to a solution of 40 µM. The author would like to thank group member, Dr. Min Wu, for her help with preparing the IL-6 and DNA solutions.

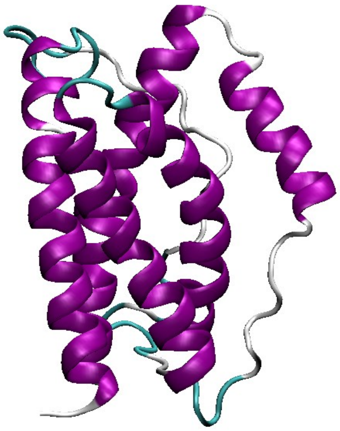

Figure 26: Molecular structure of IL-6 protein created with VMD software[235] using the 1IL6.pdb file from the Protein Data Bank[236].

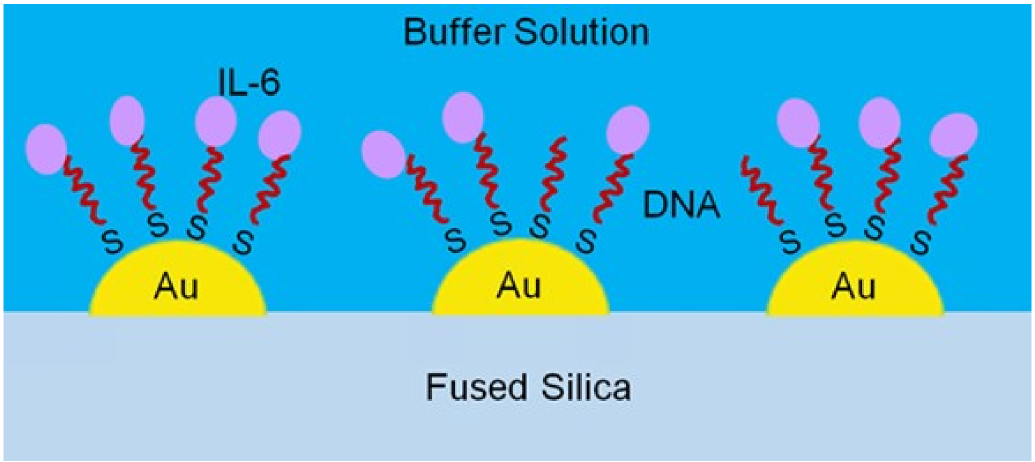

Figure 27: Scheme of the bio-functionalized samples consisting of Au/FS substrates (see **Figure 23**) carrying the immobilized DNA/IL-6 complex.

The steps taken for samples' biofunctionalization are illustrated in **Figure 28**. The Au/FS substrates were incubated with 100µL of the DNA aptamer solution at room temperature for 24 hours. After subsequent rinsing with Tris-EDTA buffer solution at least 2 times, the samples were incubated with 20 µL of the IL-6 solution for 24 hours. After the incubation, the samples were rinsed with Tris-EDTA buffer solution again to remove any unattached biomolecules. In addition, two sets of benchmark samples were prepared for comparison. In one of these additional sets, the Au/FS substrates were incubated with 100 μL of the DNA aptamer solution for 24 hours and rinsed; however, they were not loaded with the IL-6 protein. In the second set of samples, the Au/FS substrates were incubated with 20 μL of the IL-6 solution for 24 hours without prior addition of the DNA aptamer, and subsequently rinsed. After rinsing, all the biofunctionalized samples were sprayed with fresh buffer solution, capped with a thin glass cover, and sealed as described elsewhere[19] to prevent evaporation of the solution and protect the samples from damage.

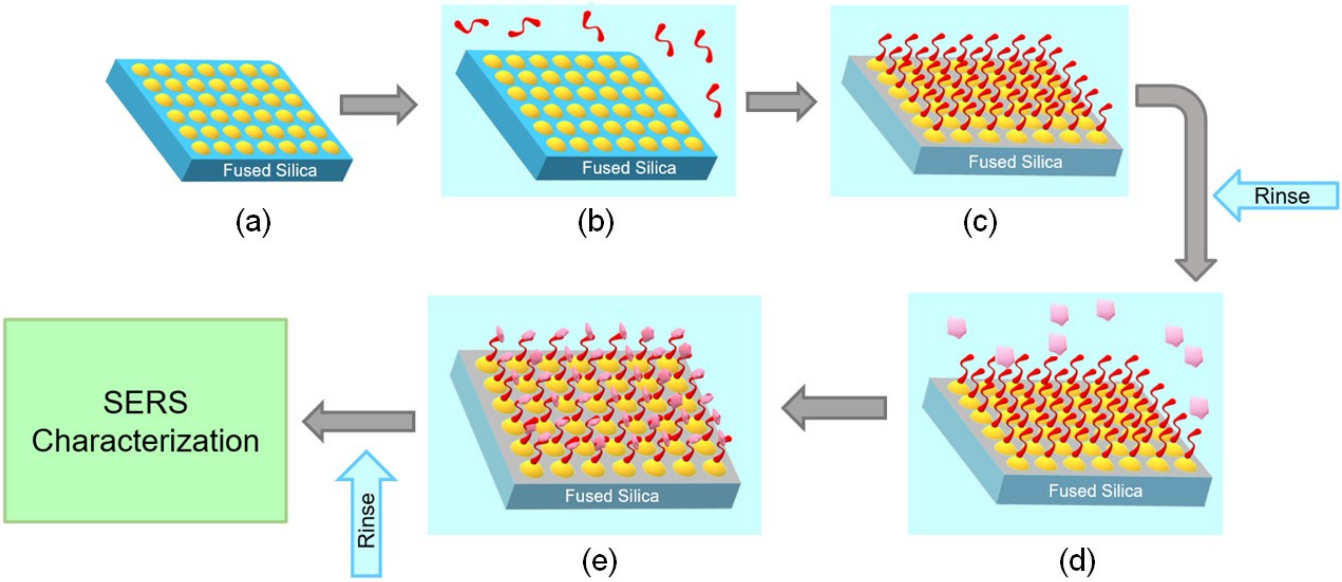

Figure 28: Steps of substrate bio-functionalization: (a) – The Au nanopattern on FS support; (b) – incubation with the solution of thiolated DNA aptamer; (c) – binding of DNA to Au nanodots; (d) – incubation with the solution of IL-6 protein; (e) – binding of IL-6 to the Au-immobilized DNA.

To collect Raman spectra from the samples, the Renishaw inVia Qontor confocal Raman microscope (Sect. 3.4) was used with a 785 nm laser excitation wavelength. The 532 nm and 633 nm excitation wavelengths were also tested; however, the 785 nm exposures resulted in better signal-to-baseline ratios of the Raman spectra than the other wavelengths. The exposures were done at a 1.5 mW power and exposure of 10 s during each acquisition, which are typical conditions used for this Raman microscope. A 50X objective lens and a 10X eyepiece were employed. The acquired spectra were background-subtracted using Renishaw's Windows®-based Raman Environment (WiRE™) software. All the samples were maintained in an aqueous environment at all times during the entire experiment.

Figure 29 depicts a SERS spectrum from the DNA/IL-6 complex immobilized on the nanopatterned Au/FS substrate. By the design, it is expected that the DNA strands bind to the surface of Au nano-dots through their thiol groups (see **Figure 27**). After biofunctionalization of the Au/FS substrate followed by rinsing and buffer replacement, any biological components are supposed to be present only on the surface of the substrate in a monolayer quantity or less. Nevertheless, the spectral region of approximately 400 - 2000 cm^{-1}, which is often termed the fingerprint region due to its relation to unique molecular vibrations, exhibits distinct SERS bands. **Table I** lists the most pronounced bands from the spectrum in **Figure 29** accompanied by interpretations based on the literature. For comparison, **Figure 30** shows a SERS spectrum of the benchmark sample after incubation with the DNA aptamer alone, rinsing, and buffer replacement. The corresponding spectral fingerprint represents Au-immobilized DNA aptamers without the protein attached. Major bands of the spectrum are listed in **Table I**. In addition, **Figure 31** presents a spectrum from the Au/FS substrate after incubation with a solution of IL-6 protein alone, rinsing, and buffer replacement. The low intensity of SERS bands in the spectrum in **Figure 31** indicates inefficient attachment of the IL-6 protein directly to the Au/FS substrate in the absence of the DNA aptamer, resulting in insufficient retention of the protein at the surface after rinsing.

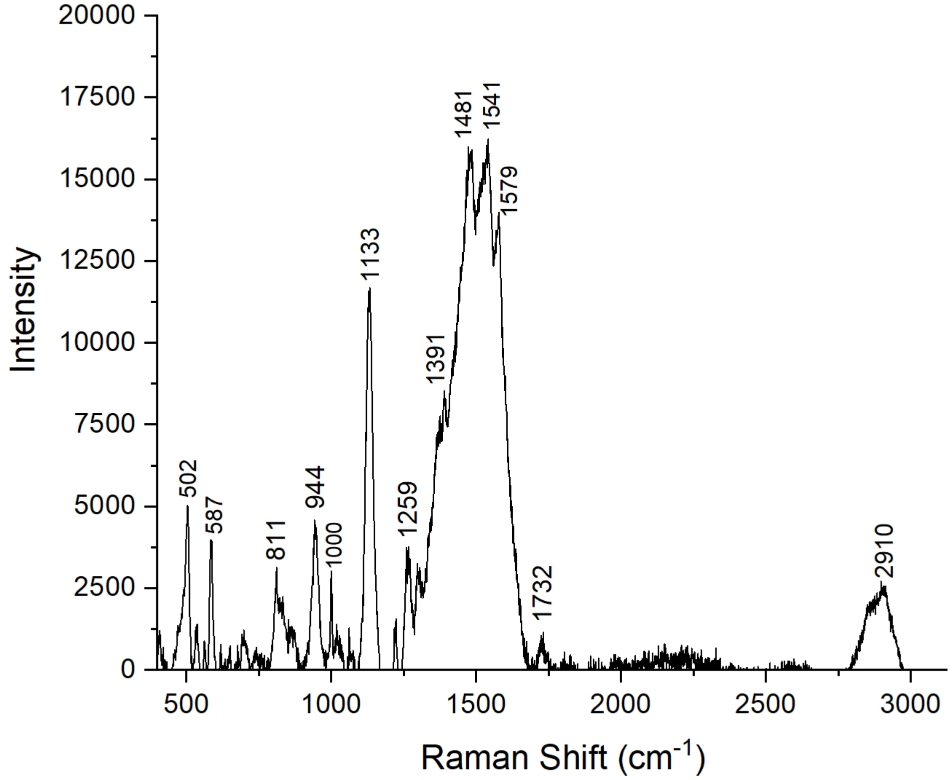

Figure 29: SERS spectrum of the Au-immobilized DNA/IL-6 complex. The spectrum was background-subtracted.

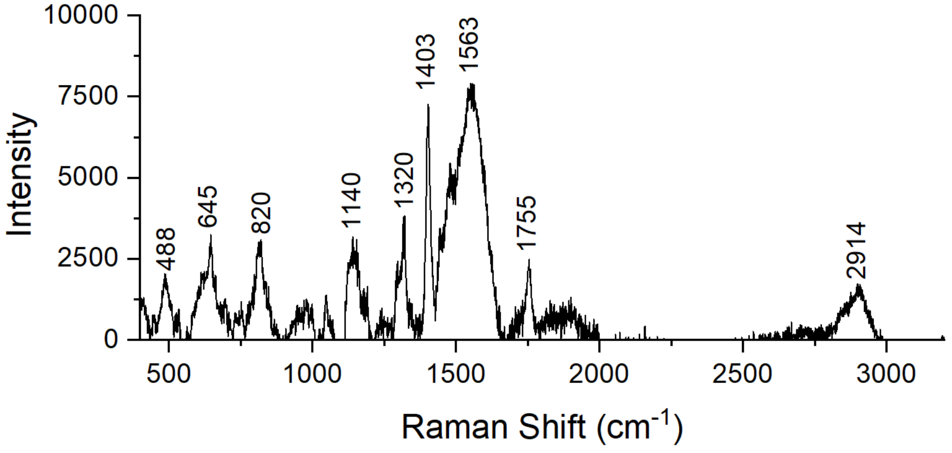

Figure 30: SERS spectrum of the Au-immobilized IL-6 binding DNA aptamer. The spectrum was background-subtracted.

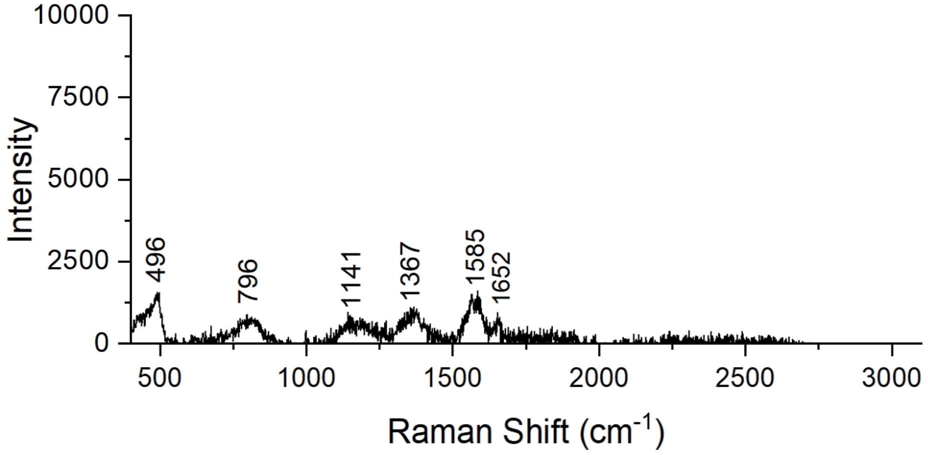

Figure 31: SERS spectrum from the Au/FS substrate after incubation with IL-6 protein alone, rinsing and buffer replacement. The spectrum was background-subtracted.

In the SERS spectrum from the Au-immobilized DNA/IL-6 complex in **Figure 29**, the strongest fingerprint feature arises from an overlap of several closely positioned bands. Peaks at 1391 cm^{-1}, 1481 cm^{-1}, 1541 cm^{-1}, and 1579 cm^{-1} can be distinguished. In the literature, Raman bands in the region of approximately 1350-1450 cm^{-1} are often attributed to C-H and C-C bond vibrations in amino acids and proteins[237,238,239,240]. In particular, Raman bands reasonably close to the observed peak at 1391 cm^{-1} were reported for lyophilized IL-6[237]. The other bands with peaks at approximately 1481 cm^{-1}, 1541 cm^{-1}, and 1579 cm^{-1} can be assigned to various vibrational modes in IL-6 as well[237,238,239]. However, such bands are also attributable to vibrations in DNA[241,242], as listed in **Table I**. The next prominent feature in **Figure 29**, a strong and narrow peak at 1133 cm^{-1}, can be attributed to C-N and C-C bond stretching in both DNA and IL-6 protein[237,240,241,242]. The remaining bands peaking at 1000 cm^{-1}, 944 cm^{-1}, 811 cm^{-1} and 502 cm^{-1} have been attributed to IL-6[237,239,240,241,242], whereas the band at 587 cm^{-1} seems to originate from DNA[242]. Finally, the band peaking at 2914 cm^{-1} (C-H bond stretching) is common for many organic compounds including both proteins and DNA[241].

The SERS spectrum from the Au-immobilized IL-6 free DNA aptamer shown in **Figure 30** exhibits a prominent feature with a peak at 1563 cm^{-1}. In Raman and SERS studies of DNA samples, bands near this region are commonly attributed to stretching of pyrimidine ring[241,242]. Remarkably, both the location and the apparent contribution of several closely positioned bands are reminiscent of similar spectral feature in **Figure 29**, although the intensity of the highest peak is less than in **Figure 29**. Other notable peaks are found at 820 cm^{-1} (O-P-O bonds stretches in DNA[241]) and at 1140 cm^{-1} (C-N bond vibrations in DNA[241]). For the latter, a reasonably matching band is observed in **Figure 29** at 1133 cm^{-1}.

Table I: SERS band assignments for the Au-immobilized DNA/IL-6 complex and IL-6 free DNA aptamer.

Raman Shifts, cm^{-1}		**Assignments**	**References**
DNA/IL-6	**DNA**		
	488	Cytosine ring vibrations in DNA	171,241
502		S-S bond stretching in IL-6	239,241,242
587		Ring vibrations in DNA	241,242
	645	Ring vibrations in DNA	241,242
811		C-C, C-O, and C-H bond vibrations in IL-6	240

	820	O-P-O stretch in DNA	[241]
944		Backbone C-C stretching for α-helices in IL-6	[237,239,242]
1000		Aromatic ring vibrations of PHE residue in IL-6	[237,239,242]
1133	1140	C-N, C-C vibrations in IL-6 and DNA	[237,240-242]
1259		Amide III mode in IL-6; C-N vibrations in DNA	[237-239,241]
	1320	Guanine ring vibrations in DNA	[241]
1391	1403	C-H vibrations in IL-6 and DNA	[237,239-242]
1481		CH_2 and CH_3 bending in IL-6; C-N and C=N stretching in DNA	[237,239,242]
1541	1563	Amide II mode in IL-6; ring vibrations in DNA	[237,238,241,242]
1579		Aromatic ring vibration of TYR and PHE in IL-6; adenine and guanine ring stretching in DNA	[237,239,242]
1732	1755	Amide I mode in IL-6; C=O vibrations in DNA	[237-239,241]
2910	2914	C-H stretching in IL-6 and DNA	[237,241]

From comparison of the SERS results, it appears that the spectrum of immobilized DNA/IL-6 complex in **Figure 29** is influenced by fingerprints of both the IL-6 protein[237] and the

DNA aptamer. The interpretation of specific bands is often not unique, since some vibrations in the IL-6 and in the DNA occur at close frequencies. A pronounced difference across the spectra in **Figure 29** and **Figure 30** relates to the intensity of major peaks. The intensities of the strongest bands from the immobilized DNA/IL-6 complex in **Figure 29** are approximately two times higher than their counterparts from the immobilized IL-6 free DNA aptamers in **Figure 30**. This difference cannot be explained by concurrent attachment of the IL-6 protein to the Au/FS substrate due to inefficient attachment of the protein directly to the substrate. Therefore, the well-pronounced SERS fingerprint from the DNA/IL-6 complex in **Figure 29** results from specific attachment of IL-6 protein to the immobilized DNA aptamer. In particular, overlapping vibration bands from C-H, C-N, and C-C bonds, as well as from ring-forming groups in both IL-6 and DNA produce the prominent spectral features at 1100-1600 cm^{-1} in **Figure 29**. For additional comparison, an attempt was done to collect unenhanced Raman spectra from a drop of IL-6 solution deposited on a piranha-cleaned, bare FS substrate without Au nanostructures. However, in the absence of SERS enhancement, Raman spectrum of IL-6 solution could not be identified through available background-extraction procedures due to overwhelming fluorescence signal.

To conclude, the Au/FS plasmonic substrates were confirmed to provide sufficient SERS enhancement for the collection of the spectra from Au-immobilized DNA/IL-6 complexes, as well as from the immobilized IL-6 free DNA. As already mentioned, some vibrations occur at close frequencies in both the IL-6 and in the DNA, and therefore the corresponding SERS bands overlap. Generally speaking, overlaps of SERS or Raman bands are common for bio-detection applications[238,239,240] especially when multiple biological components are present[241]. For this reason, Raman/SERS spectra are often analysed in terms of cumulative vibrational fingerprints[241], rather than individual spectral bands. **Figure 29** exhibits a distinct SERS fingerprint of Au-immobilized

DNA/IL-6 complex. From comparison of the SERS spectrum in **Figure 29** and additional four spectra from the DNA/IL-6 complex shown in **Supplementary Figure 37**, the characteristic features of the SERS fingerprint for the DNA/IL-6 complex include an intense and broad bundle of overlapping peaks between 1350 and 1600 cm^{-1}; a strong and narrow peak at 1333-1141 cm^{-1}; and a medium-intensity peak at 498-504 cm^{-1}. **Supplementary Table II** lists the average positions and standard deviations of the positions of these features across the five spectra. From both the visual inspection of the spectra and the calculated standard deviations, it is clear that these features are reproduced consistently across the repetitive SERS experiments of the DNA/IL-6 complex immobilized on the Au/FS substrates. According to **Table I**, most of the bands of the repetitive fingerprint are attributable to molecular vibrations in both IL-6 and DNA. Other bands listed in **Table I** such as 587, cm^{-1}, 811 cm^{-1}**,** 944 cm^{-1}, 1000 cm^{-1},1259 cm^{-1}, and 1000 cm^{-1}, although tending to be less intense, are observed in at least three out of the five SERS spectra. Summarising, the multiple collected SERS spectra exhibit a significant consistency of the fingerprint of the DNA/IL-6 complex. However, certain variability has also been observed. This highlights the importance of future development of efficient SERS spectrum recognition techniques, as outlined earlier in Sect. 2.3.2.

Although detailed deconvolution of the spectra and their analysis in terms of individual IL-6 or DNA bands was not pursued in this work, the applicability of the Au/FS plasmonic substrates for SERS fingerprinting of multi-component biological samples can be considered demonstrated. Importantly, the experiments also confirm the consistency of the SERS fingerprinting for sub-monolayer quantities of the DNA/IL-6 complex. The amount of immobilized DNA/IL6 complexes is not known precisely; however, with the expectation that the DNA/IL6 load of the Au dots in our experiments is close to a monolayer, from the signal-to-noise ratio of the spectra in **Figures 29** and **37(a-d)** one can infer that the sensitivity limit of the SERS detection is of the order of approximately 1/5 of the monolayer. Assuming, from geometrical considerations, that the number of immobilized DNA/IL-6 complexes might be close to 25 per one Au dot, the estimated detection limit is approximately 5 complexes per dot.

4.2.2. Toward Applications of Ag/ITO Nanostructures and Au-Nanopits

As a part of the collaboration project with Dr. Karthik Shankar, preliminary tests of photocatalytic properties, the 50-nm pitch arrays of Ag nanodots on ITO substrates (**Figure 24**(a)) were performed by members of their group. For these tests, photocatalytic reduction of aromatic thiol 4-nitrobenzenethiol (NBT) into a dimerized form, dimercaptoazobenzene (DMAB)[13], was used. For this purpose, multiple Ag/ITO samples were incubated with NBT and dried. The dried NBT/Ag/ITO samples were exposed to a 532 nm laser, and SERS spectra were collected with the Renishaw inVia Qontor Raman microscope. All the spectra exhibited strong SERS bands typical of the reduced isoform DMAB[13], such as for example strong bands at approximately 1141 cm^{-1}, 1390 cm^{-1} and 1435 cm^{-1}. Such vibration bands are not observed in the monomeric oxidized 4-NBT[13]. Therefore, photocatalytic plasmon-mediated reduction of NBT into DMAB occurred during the laser exposures of the NBT/Ag/ITO samples. These preliminary tests confirm that the fabricated 50 nm pitch arrays of Ag nanodots on ITO substrates offer a very good promise for plasmonic-induced photocatalysis. Whereas the conclusions from these tests are very important to support the objectives of the present thesis, the author claims the fabrication of Ag nanodots on the ITO substrates only. The Ag/ITO sample's functionalization with NBT, as well as the laser exposures and the collection of SERS spectra were performed by members of Dr. Karthik Shankar group, and therefore these results are not claimed as contributions of this thesis.

Although both 50 nm pitch arrays, Au/FS and Ag/ITO, have proven efficient as plasmonic substrates, it should be noted that the 50 nm pitch geometry still has room for improvements. In the first place, this geometry exploits the buildup of plasmon-induced electromagnetic fields, which are the strongest within narrow inter-particle gaps of about 20 nm and less[229]. The desire to balance this "near-field" electromagnetic enhancement with inter-particle gaps that could accommodate biological macromolecules such as DNA or proteins resulted in the periodic arrays of noble metal nanodots with a pitch of 50 nm and inter-particle gaps of 20-25 nm. However, for visible-light excitation, collective plasmonic resonance is achieved at greater dimensions[135,137]. In an effort to both achieve a near-field enhancement and approach resonance conditions, we created periodic arrays of Ag nanodot heptamers with a 400 nm pitch and a 50 nm distance between the dots within the heptamers on ITO substrates, such as shown in **Figure 24**(b). Such structures are expected to be more efficient than 50 nm pitch arrays of nanodots, for both SERS enhancement and plasmonic photocatalysis. Tests of the fabricated heptameric structures are currently ongoing with the Dr. Karthik Shankar group. If confirmed to be efficient, such substrates can significantly advance applications of nanoplasmonics in the community.

One more design of nanostructures that we developed, the periodic arrays of nano-pits fabricated by FIB milling (**Figure 25**), is anticipated to perform efficiently for samples that do not involve immobilization of molecules at the surface, such as solitons[243] containing the molecules. However, this requires arrays of sizes at least 100x100 μm. As explained in Sect. 4.1.4, the He-FIB milling that we have tested does not offer a sufficient throughput to fabricate such arrays. Milling by heavier ions, such as Ga, might be more efficient for this purpose, albeit at the expense of a certain loss in resolution. However, tests of Ga milling could not be accommodated in the present work due to the instrument's accessibility pause.

4.3. SERS Characterization of Proteinaceous Multi-Phase Coacervates

To diversify applications of plasmonic substrates, 10 nm Au-coated FS substrates were additionally employed to both induce and characterize liquid-liquid phase separation in solutions of a protein termed microtubule-associated protein tau (tau)[244,245], which plays an important role in Alzheimer's, Parkinson's, and several other neurodegenerative diseases.

Lyophilized recombinant human tau protein (1-441) was purchased from Bon-Opus Biosciences. I am grateful to Jose Miguel Flores Fernandez (Dr. Holger Wille's group, Department of Biochemistry) for reconstitution of the lyophilized protein in HPLC water to obtain 55.00 µM, 27.50 µM, 13.75 µM, and 5.50 µM solutions.

To prepare plasmonic substrates for subsequent characterization of the tau protein solutions, the piranha cleaned FS substrates were coated with a 10 nm layer of Au using the Kurt J. Lesker electron beam evaporator (Sect. 3.5). A 10 µL drop of each tau protein solution was placed in the center of the respective plasmonic substrates. Therefore, protein molecules were contained in the solution without specific attachment to the substrate. To prevent evaporation, the samples were covered with a thin glass slide and sealed as described elsewhere[19]. The Renishaw inVia Qontor confocal Raman microscope (Sect. 3.4) was employed to collect confocal microscopy images and SERS spectra of the samples. The samples were exposed with a 785 nm laser of 1.5 mW power during 10 sec for each SERS acquisition, using a 50x objective lens.

Figure 32 presents confocal microscopy images of a 55 µM solution of tau protein on the plasmonic substrate (Au-coated FS). Droplets of tau phase-condensate can be discerned in all the images. The size of the droplets varies. Interestingly, the biggest droplets have formed regular circular structures of 100-200 µm in diameter. Such morphologies can be attributed to an unusual phenomenon known as the multiphase coacervation[246] – a process when a solution of charged macromolecules undergoes a separation into multiple liquid phases. **Figure 33** shows representative SERS spectra gathered at different locations: from the interior of a circular structure (a); from a large droplet at the periphery of the circle (b); and from outside of the circular structures. The highest intensity of the characteristic 1333-1350 cm^{-1} band is observed from a large drop at the periphery of the circle. The differences across the three SERS fingerprints may indicate the coexistence of at least three liquid phases in the 55 µM solution of tau protein.

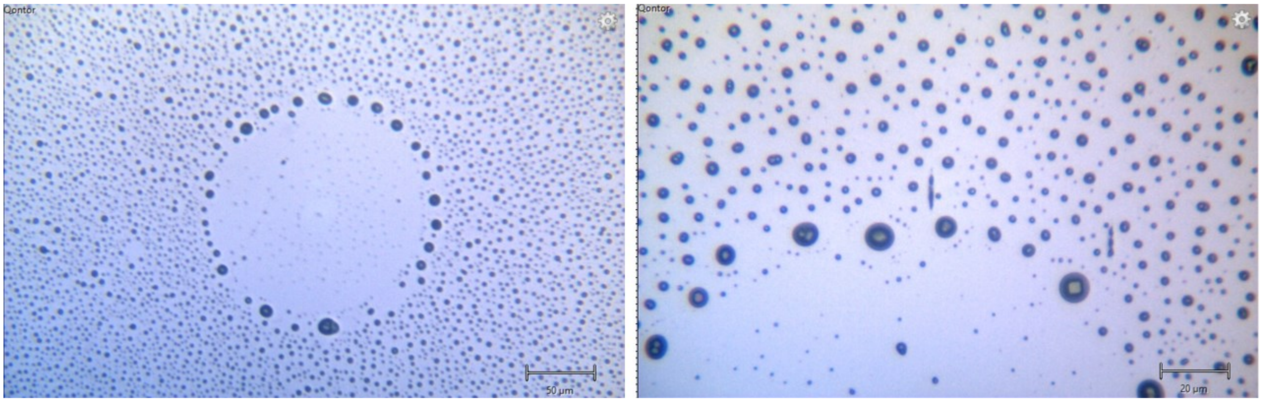

Figure 32: Confocal microscopy images (Renishaw inVia Qontor) of phase-condensate droplets in a 55 µM solution of tau protein on a plasmonic Au/FS substrate. The size bars are 50 µm (left) and 20 µm (right). Unexpectedly, the largest droplets have formed multiple circular structures.

For comparison, **Figure 34**(a) presents a confocal microscopy image of a 27.50 µM solution of tau protein on a plasmonic Au/FS substrate. Quasi-circular structures of approximately 100-200 µm in size are clearly visible; however, smaller droplets of phase-condensate cannot be discerned. The corresponding SERS spectra taken inside of a circular structure (b), at its periphery (c), and outside (d) feature several strong peaks. Unlike the spectra shown in **Figure 33**, the highest intensities of the SERS bands are found inside the circular structures. Spectral fingerprints from inside and outside of the circular structures are dramatically different.

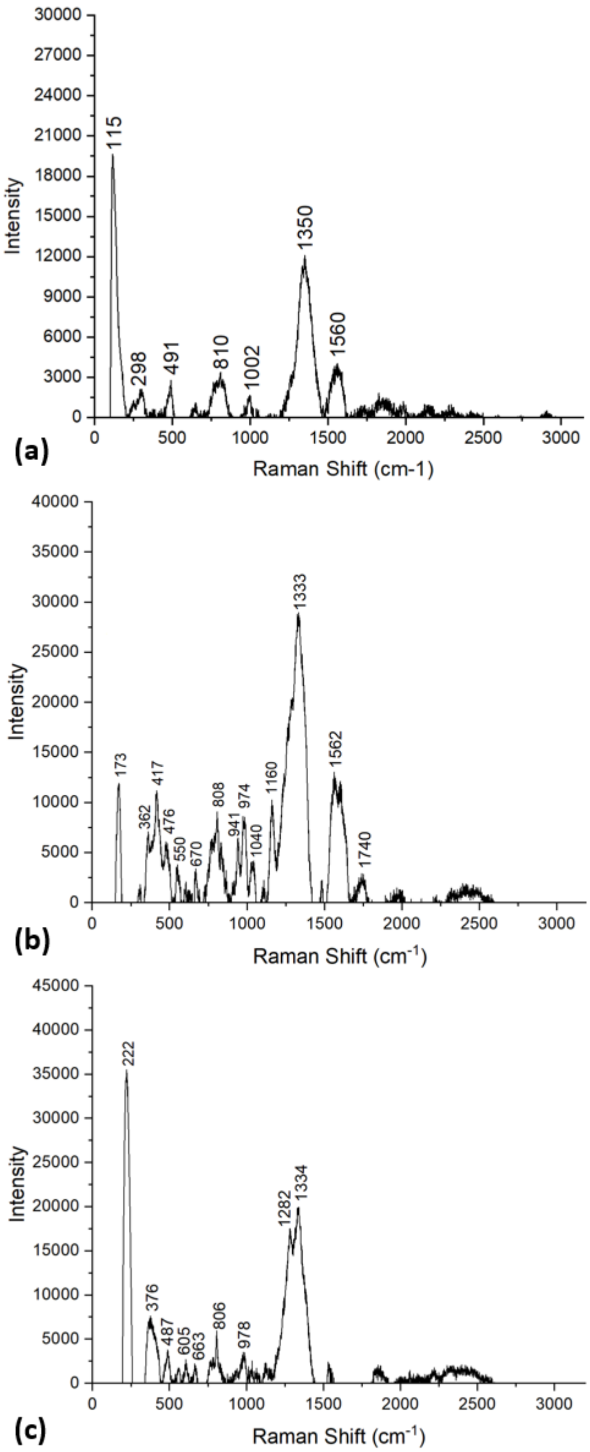

Figure 33: SERS spectra of the tau protein phase-condensates from **Figure 32:** (a) – Inside the circle of droplets; (b) – from a large droplet at the periphery of the circle; (c) – outside of circles of droplets.

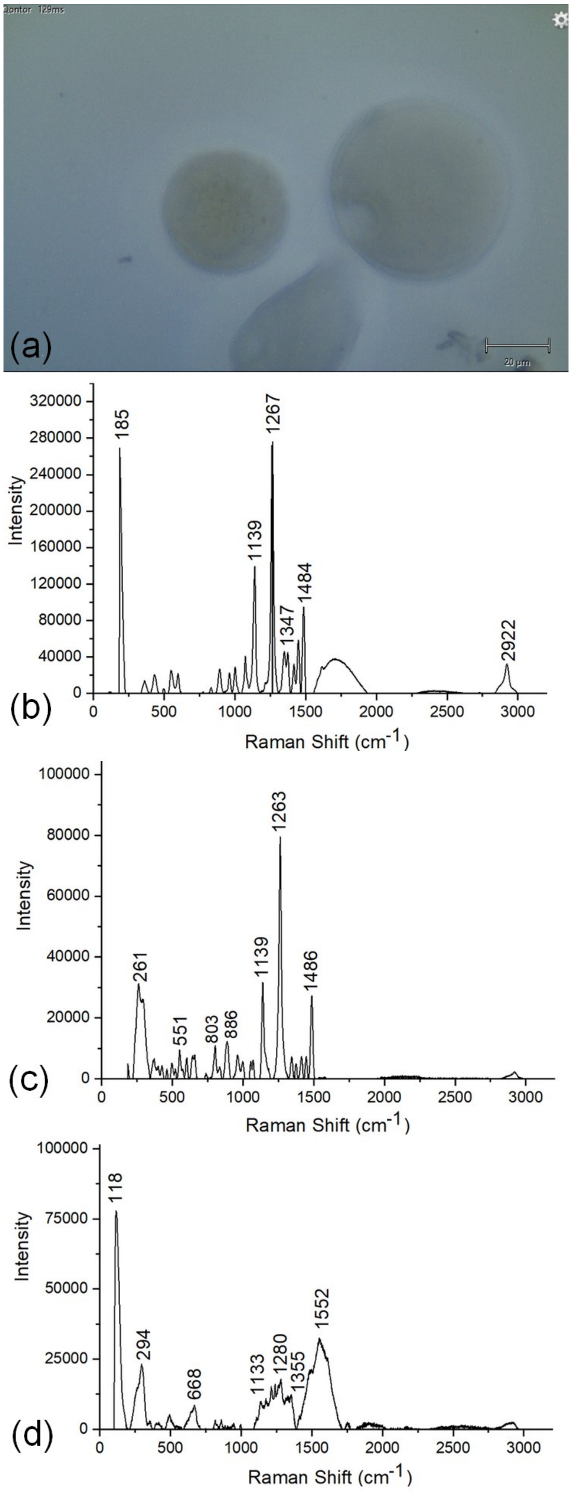

Figure 34: (a) – Confocal microscopic image of potential phase separation in a 27.50 μM solution of tau protein on plasmonic Au/FS substrate; (b – d) – the corresponding SERS spectra taken inside (b), at the periphery (c), and outside (d) of the quasi-circular structures.

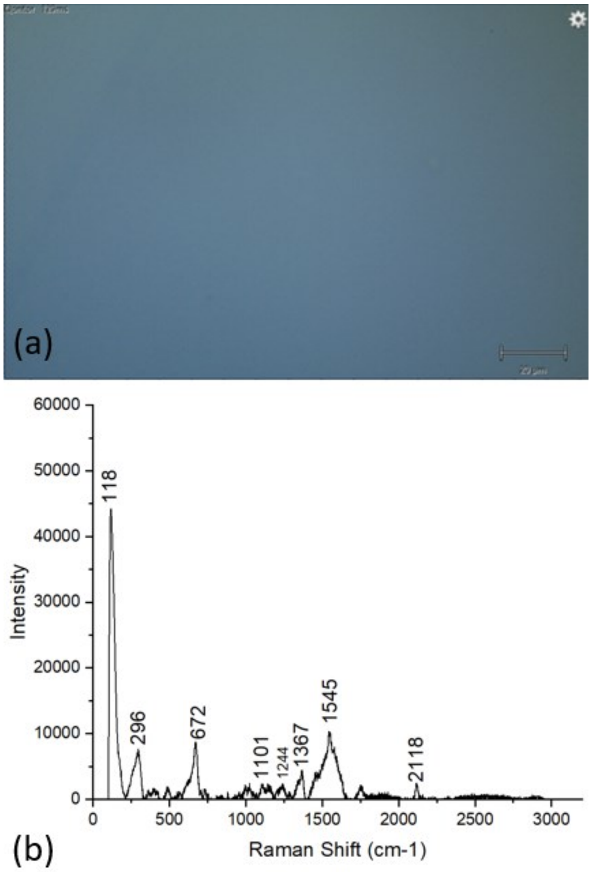

Figure 35: (a) – Confocal microscopic image of a 13.75 µM tau protein solution on plasmonic Au/FS substrate; (b) – the corresponding SERS spectrum.

Next, **Figure 35**(a, b) depict confocal microscopy image (a) and the corresponding SERS spectrum (b) for a 13.75 µM solution of tau protein on an Au/FS substrate. No phase separation is discernible in (a). Positions of Raman bands of the spectrum in (b) are reasonably close to those in **Figure 34**(d), although the intensities are lower. For the 5.50 µM, no phase separation was detected either. Positions of SERS bands were close to those in **Figure 34**(d).

Summarizing, from these data one can infer that the solutions of tau protein with concentrations of 27.50 µM and 55 µM are prone to undergo at least two sequential phase separations. The first phase separation is illustrated by **Figure 34**. In this case, droplets of 100-200 µm in size have formed. Based on the intensities of the Raman bands, on can infer the droplets are enriched in tau, whereas the surrounding regions are depleted. The difference in Raman fingerprints may indicate that the phase separation could be accompanied by a change in conformations of the tau protein. The data in **Figure 32** and **Figure 33** suggest a more complicated process. One can hypothesize that the confocal microscopy images in **Figure 32** might result from a two-stage process that comprises formation of 100-200 μm droplets of a depleted solution of tau embedded in more concentrated background; this is followed by second phase separation into smaller micro-droplets containing highly concentrated tau protein. Of course, these preliminary hypotheses require confirmation.

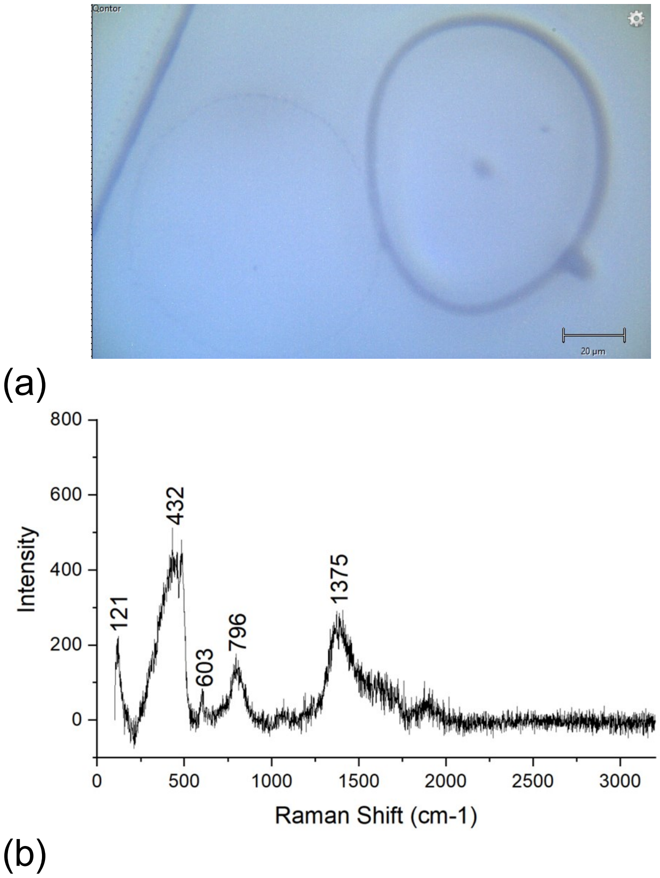

Figure 36: Confocal microscopy image of a 55 μM solution of tau protein (a) and a corresponding Raman spectrum (b) on a bare FS substrate without Au coating.

n order to better understand the role of the Au coating present at the surface of the FS substrates, a 55 μM tau protein solution was placed on a bare piranha-cleaned FS substrate without Au coating and characterized. **Figure 36**(a) shows a representative confocal microscopy image. Although the image exhibits lines reminiscent of phase boundaries, and some of these lines form elliptic structures of 100-200 μm in size, smaller phase-condensate droplets cannot be discerned. The Raman spectral fingerprints (**Figure 36**(b)) were uniform across the sample, with the intensities of the characteristic 1375 cm^{-1} band 40-70 times lower than in similar solutions on a Au-coated FS substrate. One can cautiously hypothesize that the presence of plasmonic Au coating may both facilitate the second liquid-liquid phase separation in tau protein solutions and produce the enhanced SERS signals. If this interpretation is confirmed by future studies, then the community will receive an unprecedented in-vitro technique for interrogating morphological, structural, and dynamical properties of proteinaceous phase-condensates. This may provide a missing link toward development of preventive treatments for Alzheimer's and Parkinson's diseases. In a broader context, it would be possible to create diverse multifunctional nanoplasmonic architectures combining material modulation functions with SERS characterization of ongoing physico-chemical processes in-situ within the same device.

5. Conclusions and Outlook

In this thesis work, the existing methods[19] for EBL-based fabrication of PMMA masks on dielectric supports have been extensively modified. New conductive polymer, Electra 92, was employed to create a protective layer to avoid distortions due to charging of the fused silica (FS) substrate during EBL exposures. This was accompanied by a decrease of the accelerating voltage from 30 keV to 10 keV, as well as the corresponding optimization of the exposure doses. Computer simulations[18,] were used extensively to better understand the impact of the protective layer onto the broadening of the electron beam in the sample. High-quality periodic arrays of 50 nm pitch nanodots were fabricated in PMMA on FS supports, although the simulations have predicted a significant broadening of the electron beam due to the added thickness of the conductive polymer. This is the first successful fabrication of periodic 50 nm pitch arrays of dots on FS supports using 10 keV EBL exposures achieved in this group. The patterned PMMA was used as a mask to fabricate plasmonic nanostructures that comprised periodic arrays of 50 nm pitch Au nanodots on FS supports. The 50 nm periodicity of Au dots with 20-25 nm inter-dot gaps was selected in an effort to obtain the near-field electromagnetic enhancement of plasmonic waves in the arrays of Au dots.

To test the performance of the Au/FS nanostructures as plasmonic substrates, the samples were used for SERS characterization of an important inflammation marker, protein IL-6. The IL-6 protein was immobilized on the substrate's surface via specific binding to a Au-attached IL-6 binding DNA aptamer. Pronounced SERS fingerprints of the immobilized DNA/IL-6 complex were obtained. These fingerprints exhibited distinct difference from immobilized DNA without the protein, even though both the DNA/IL-6 complex and IL6-free DNA were present at the surface of the substrates in sub-monolayer quantities. This extremely high sensitivity confirms that near-field plasmonic effects in the 50 nm pitch Au dots on FS substrates result in sufficient SERS enhancement for fingerprinting of immobilized multi-component biological samples.

Next, in a framework of the group's collaboration project, 10 keV EBL was employed to fabricate plasmonic Ag nanostructures on indium tin oxide (ITO) supports. Computer simulations[18,] were performed to rationally optimize the required exposure doses. The computational predictions of the optimal doses were followed by experimental tests. Together with the simulations, these tests have identified the applicable exposure dose regimes. 50 nm pitch arrays of nanodots were successfully fabricated in PMMA on ITO substrates, and used as a mask for the fabrication of 50 nm pitch arrays of Ag nanodots on ITO. The performance of the fabricated Ag/ITO nanostructures as plasmonic substrates has been tested by the collaborator's group. According to the preliminary tests, the Ag/ITO substrates have demonstrated a very good promise for inducing plasmonic-triggered photocatalytic reduction of an aromatic thiol compound.

In order to complement near-field plasmonic effects with collective plasmonic resonance, 400 nm pitch arrays of heptamers consisting of seven Ag dots with 50 nm inter-dot distances were fabricated on ITO substrates. Currently, the improved Ag/ITO plasmonic nanostructures are undergoing characterization in the collaborator's group. If confirmed to be efficient, such substrates can significantly advance applications of nanoplasmonics in the community.

Complementary to arrays of noble-metal nanodots, periodic arrays of nanopits or nanopores are also known to exhibit plasmonic properties[164,176,179]. In order to additionally broaden the capabilities to fabricate plasmonic nanostructures, helium FIB milling was employed to create arrays of pits directly in a layer of Au on a FS substrate. High quality periodic arrays of 15 nm wide pits in Au films on FS substrates have been successfully fabricated. However, in its current form the He-FIB technique is significantly slower than EBL, which limits its applicability to fabricate large arrays of plasmonic nanostructures. In the future, heavier ions might be employed to increase the efficiency of FIB fabrication, although at the expense of a loss in resolution.

In order to additionally test potential multifunctional applications, plasmonic substrates created by PVD deposition of Au on FS supports were employed to characterize liquid-liquid phase separation in a solution of microtubule-associated protein tau, which plays an important role in Alzheimer's, Parkinson's, and several other neurodegenerative diseases. In this experiment, protein molecules were contained in a solution without specific attachment to the substrate. The results suggest that plasmonic nanostructures may facilitate multiphase coacervation – a process when a solution of charged macromolecules undergoes multiple separations into coexisting liquid phases. If this is confirmed by future studies, then the community will receive an unprecedented in-vitro technique for interrogating morphological, structural, and dynamical properties of proteinaceous phase-condensates. This may provide a missing link toward development of preventive treatments for several severe diseases associated with protein misfolding.

Summarizing, the results reported here demonstrate that plasmonic nanostructures could potentially serve for a broad variety of applications. These may include ultra-sensitive SERS biodetection; plasmonis-triggered photocatalysis; induction of phase-separation phenomena in solutions; as well as multifunctional integration thereof. Furthermore, due to their planar geometry and selection of materials, the developed plasmonic substrates are compatible with both integrated microelectronics and microfluidics settings[16,247]. The challenges relate primarily to the efficiency and cost of the direct-write processes such as EBL or FIB. Further optimization would address, in the first place, improvements of the sensitivity of EBL and/or FIB nanopatterning. In particular, in case of EBL this would include adjustments of the design for both the resist and the protective anti-charging coating, as well as continued co-optimization of low-kV exposure and development processes. Alternatively, in case of FIB, a trade-off of the pattern dimensions with the ion mass and acceleration voltage is required to increase the efficiency.

References

[1] Naldoni, A., Shalaev, V. M., and Brongersma, M. L. (2017). "Applying plasmonics to a sustainable future". *Science, 356* (6341), 908-909.

[2] Lin, K.-T., Lin, H., and Jia, B. (2020). "Plasmonic nanostructures in photodetection, energy conversion and beyond". *Nanophotonics, 9*(10),3135-3163.

[3] Langer, J., de Aberasturi, D. J., Aizpurua, J., Alvarez-Puebla, R. A., Auguié, B., Baumberg, J. J., ... & Liz-Marzán, L. M. (2020). "Present and Future of Surface-Enhanced Raman Scattering". *ACS Nano, 14*(1)*,* 28-117.

[4] Wang, X., Huang, S.-C., Hu, S., Yan, S., and Ren, B. (2020). "Fundamental understanding and applications of plasmon-enhanced Raman spectroscopy". *Nature Reviews Physics, 2* (5),253-271.

[5] Fan, M., Andrade, G. F., and Brolo, A. G. (2020). "A review on recent advances in the applications of surface-enhanced Raman scattering in analytical chemistry". *Analytica chimica acta, 1097,*1-29.

[6] Linic, S., Aslam, U., Boerigter, C., and Morabito, M. (2015). "Photochemical transformations on plasmonic metal nanoparticles". *Nature materials,14*(6), 567-576.

[7] Zhan, C., Chen, X.-J., J. Yi, Li, J.-F., Wu, D.-Y., and Tian, Z.-Q. (2018). "From plasmon-enhanced molecular spectroscopy to plasmon-mediated chemical reactions". *Nature Reviews Chemistry, 2* (9),216-230.

[8] Li *et al.*, S. (2021). "Recent advances in plasmonic nanostructures for enhanced photocatalysis and electrocatalysis". *Advanced Materials, 33*(6), 2000086.

[9] Aslam, U., Rao, V. G., Chavez, S., and Linic, S. (2018). "Catalytic conversion of solar to chemical energy on plasmonic metal nanostructures". *Nature Catalysis, 1*(9), 656-665.

---

[10] Warkentin, C. L., Yu, Z., Sarkar, A., and Frontiera, R. R. (2021). “Decoding chemical and physical processes driving plasmonic photocatalysis using surface-enhanced Raman spectroscopies”. *Accounts of Chemical Research, 54*(10) 2457-2466.

[11] Li, Z., and Kurouski, D. (2021). “Nanoscale structural characterization of plasmon-driven reactions”. *Nanophotonics, 10*(6),1657-1673.

[12] Shattique, M. R., and Stepanova, M. (2020). “Surface Plasmon-Driven Reversible Transformation of DNA-Bound Methylene Blue Detected In-Situ by SERS”. *Plasmonics, 15*(2), 427-434.

[13] Manuel, A. P., Barya, P., Riddell, S., Zeng, S., Alam, K. M., and Shankar, K. (2020). “Plasmonic photocatalysis and SERS sensing using ellipsometrically modeled Ag nanoisland substrates”. *Nanotechnology, 31* (36), 365301.

[14] De Albuquerque, C. D. L., Zoltowski, C. M., Scarpitti, B. T., Shoup, D. N., and Schultz, Z. D. (2021).“Spectrally Resolved Surface Enhanced Raman Scattering Imaging Reveals Plasmon-Mediated Chemical Transformations”. *ACS Nanoscience Au, 1*(1) 38-46.

[15] Kasani, S., Curtin, K., and Wu, N. (2019). “A review of 2D and 3D plasmonic nanostructure array patterns: fabrication, light management and sensing applications”. *Nanophotonics, 8*(12), 2065-2089.

[16] Dong, B., Ma, Y., Ren, Z., and Lee, C. (2020). “Recent progress in nanoplasmonics-based integrated optical micro/nano-systems”. *Journal of Physics D: Applied Physics, 53*(21), 213001.

[17] Chen *et al.*, Y. (2021). “Sub-10 nm fabrication: methods and applications”. *International Journal of Extreme Manufacturing, 3*(3), 032002.

[18] Mohammad, M. A., Muhammad, M., Dew, S. K., and Stepanova, M. (2012). "Fundamentals of electron beam exposure and development". in *Nanofabrication*: Springer, 11-41.

[19] Peters, R. F., Gutierrez-Rivera, L., Dew, S. K., and Stepanova, M. (2015). "Surface enhanced Raman spectroscopy detection of biomolecules using EBL fabricated nanostructured substrates". *JoVE (Journal of Visualized Experiments), 97*, e52712.

[20] Mehrotra, P. (2016). "Biosensors and their applications–A review". *Journal of oral biology and craniofacial research*, *6*(2), 153-159.

[21] Zourob, M., Elwary, S., & Khademhosseini, A. (Eds.). (2010). "Recognition receptors in biosensors". *Springer,* 415-448.

[22] Murugaiyan, S. B., Ramasamy, R., Gopal, N., & Kuzhandaivelu, V. (2014). "Biosensors in clinical chemistry: An overview". *Advanced biomedical research*, *3,* 67.

[23] Mohanty, S. P. (2001). "Biosensors: A Survey Report". *University of South Florida, USA,* 1-15.

[24] Gruhl, F. J., Rapp, B. E., & Länge, K. (2013). "Biosensors for diagnostic applications". *Advances in biochemical engineering/biotechnology*, *133*, 115–148. https://doi.org/10.1007/10_2011_130

[25] Gruhl F.J., Rapp B.E., Länge K. (2011). "Biosensors for Diagnostic Applications. In: Seitz H., Schumacher S. (eds) Molecular Diagnostics". *Advances in Biochemical Engineering/Biotechnology, Springer, 133*, 115-148. https://doi.org/10.1007/10_2011_130

---

[26] Parmin, N. A., Hashim, U., Gopinath, S. C., & Uda, M. N. A. (2019). "Biosensor Recognizes the Receptor Molecules". In *Nanobiosensors for Biomolecular Targeting, Elsevier,* 195-210.

[27] Strehlitz, B., Nikolaus, N., & Stoltenburg, R. (2008). "Protein detection with aptamer biosensors". *Sensors*, *8*(7), 4296-4307.

[28] Seo, H. B., & Gu, M. B. (2017). "Aptamer-based sandwich-type biosensors". *Journal of biological engineering*, *11*(1), 11.

[29] Hoffman, T. L., Canziani, G., Jia, L., Rucker, J., & Doms, R. W. (2000). "A biosensor assay for studying ligand-membrane receptor interactions: binding of antibodies and HIV-1 Env to chemokine receptors". *Proceedings of the National Academy of Sciences*, *97*(21), 11215-11220.

[30] Wang, J. (2005). "Carbon-nanotube based electrochemical biosensors: A review". *Electroanalysis: An International Journal Devoted to Fundamental and Practical Aspects of Electroanalysis*, *17*(1), 7-14.

[31] Hock, B., Seifert, M., & Kramer, K. (2002). "Engineering receptors and antibodies for biosensors". *Biosensors & bioelectronics*, *17*(3), 239–249. https://doi.org/10.1016/s09565663(01)00267-6

[32] Vo-Dinh, T., & Cullum, B. (2000). "Biosensors and biochips: advances in biological and medical diagnostics". *Fresenius' journal of analytical chemistry*, *366*(6-7), 540-551.

[33] Karunakaran, C., Rajkumar, R., & Bhargava, K. (2015). "Introduction to biosensors". In *Biosensors and bioelectronics, Elsevier,* 1-68.

[34] Bunney, J., Williamson, S., Atkin, D., Jeanneret, M., Cozzolino, D., & Chapman, J. (2017). “The use of electrochemical biosensors in food analysis”. *Current Research in Nutrition and Food Science Journal*, *5*(3), 183-195.

[35] Zhou, J., Qi, Q., Wang, C., Qian, Y., Liu, G., Wang, Y., & Fu, L. (2019). “Surface plasmon resonance (SPR) biosensors for food allergen detection in food matrices”. *Biosensors and Bioelectronics*, *142*, 111449.

[36] Gaudino, F., Manfredonia, I., Managò, A., Audrito, V., Raffaelli, N., Vaisitti, T., & Deaglio, S. (2019). “Subcellular Characterization of Nicotinamide Adenine Dinucleotide Biosynthesis in Metastatic Melanoma by Using Organelle-Specific Biosensors”. *Antioxidants & redox signaling*, *31*(15), 1150-1165.

[37] Mohd Said, Nur Azura & Ogurtsov, Vladimir & Herzog, Grégoire. (2014). “Electrochemical biosensor based on microfabricated electrode arrays for life sciences applications”. DOI: 10.13140/RG.2.2.11066.49603, *2014*, 1-300.

[38] Dong, S., & Chen, X. (2002). “Some new aspects in biosensors”. *Reviews in Molecular Biotechnology*, *82*(4), 303-323.

[39] Pearson, J. E., Gill, A., & Vadgama, P. (2000). “Analytical aspects of biosensors”. *Annals of clinical biochemistry*, *37*(2), 119-145.

[40] Zayats, M., Baron, R., Popov, I., & Willner, I. (2005). “Biocatalytic growth of Au nanoparticles: from mechanistic aspects to biosensors design”. *Nano Letters*, *5*(1), 21-25.

[41] The Hong Kong Institute of Education, "Biosensor - Model of biosensor", The Hong Kong Institute of Education, [Online]. Available: http://www.ied.edu.hk/biotech/eng/classrm/main.html, [Accessed 2020].

[42] Li, S., Singh, J., Li, H., and Banerjee, I. A. (2011). “Biosensor Nanomaterials”. Wiley.com.

---

[43] Mohd Said, N. A. (2014). “*Electrochemical biosensor based on microfabricated electrode arrays for life sciences applications”.* (Doctoral dissertation, University College Cork).

[44] de Freitas, R. F., & Schapira, M. (2017). A systematic analysis of atomic protein–ligand interactions in the PDB. *Medchemcomm*, *8*(10), 1970-1981.

[45] Biedermann, F., & Schneider, H. J. (2016). “Experimental binding energies in supramolecular complexes”. *Chemical reviews*, *116*(9), 5216-5300.

[46] Wells, R. A., Kellie, J. L., & Wetmore, S. D. (2013). “Significant strength of charged DNA–protein π–π interactions: a preliminary study of cytosine”. *The Journal of Physical Chemistry B*, *117*(36), 10462-10474.

[47] Kurczab, R., Śliwa, P., Rataj, K., Kafel, R., & Bojarski, A. J. (2018). “Salt bridge in ligand–protein complexes—systematic theoretical and statistical investigations”. *Journal of Chemical Information and Modeling*, *58*(11), 2224-2238.

[48] Kumar, N., Saha, S., & Sastry, G. N. (2021). “Towards developing a criterion to characterize non-covalent bonds: a quantum mechanical study”. *Physical Chemistry Chemical Physics*, *23*(14), 8478-8488.

[49] Smith, R. D., Engdahl, A. L., Dunbar Jr, J. B., & Carlson, H. A. (2012). “Biophysical limits of protein–ligand binding”. *Journal of chemical information and modeling*, *52*(8), 2098-2106.

[50] Boehr, D. D., Nussinov, R., & Wright, P. E. (2009). “The role of dynamic conformational ensembles in biomolecular recognition”. *Nature chemical biology*, *5*(11), 789-796.

[51] Whitehead, T. A., Baker, D., Fleishman, S. J. (2013). “Methods in Enzymology”. *Elsevier, 523*, 1-19.

---

[52] Gellman, S. H. (1997). “Introduction: molecular recognition”. *Chem. Rev*. 97(5) 1231–1232

[53] Xu, X., & Chen, L. (1996). “Molecular Recognition in Chemical and Biological Systems”. *Progress in Chemistry*, *8*(03), 189.

[54] Hinterdorfer, P., and Dufrêne, Y. F., (2006). "Detection and localization of single molecular recognition events using atomic force microscopy". *Nature methods, 3*, 347-355.

[55] Beckerman, M. (2005). “Molecular and cellular signaling”, *Springer,* 1-574.

[56] Kamat, V., Rafique, A., Huang, T., Olsen, O., & Olson, W. (2020). “The impact of different human IgG capture molecules on the kinetics analysis of antibody-antigen interaction”. *Analytical Biochemistry*, *593*, 113580.

[57] Justino, C. I., Freitas, A. C., Pereira, R., Duarte, A. C., & Santos, T. A. R. (2015). “Recent developments in recognition elements for chemical sensors and biosensors”. *TrAC Trends in Analytical Chemistry*, *68*, 2-17.

[58] Goud, K. Y., Kailasa, S. K., Kumar, V., Tsang, Y. F., Gobi, K. V., & Kim, K. H. (2018). “Progress on nanostructured electrochemical sensors and their recognition elements for detection of mycotoxins: A review”. *Biosensors and Bioelectronics*, *121*, 205-222.

[59] Villalonga, A., Pérez-Calabuig, A. M., & Villalonga, R. (2020). “Electrochemical biosensors based on nucleic acid aptamers”. *Analytical and Bioanalytical Chemistry*, *412*(1), 1-18.

[60] Lv, L., & Wang, X. (2020). “Recent Advances in Ochratoxin A Electrochemical Biosensors: Recognition Elements, Sensitization Technologies, and Their Applications”. *Journal of Agricultural and Food Chemistry*, *68*(17), 4769-4787.

[61] Kikuchi, N., & Kolpashchikov, D. M. (2016). “Split spinach aptamer for highly selective recognition of DNA and RNA at ambient temperatures”. *Chembiochem: a European journal of chemical biology*, *17*(17), 1589.

[62] Kolpashchikov, D. M. (2019). “Evolution of Hybridization Probes to DNA Machines and Robots”. *Accounts of chemical research*, *52*(7), 1949-1956.

[63] El-Tholoth, M., Bau, H. H., & Song, J. (2020). “A single and two-stage, closed-tube, molecular test for the 2019 Novel Coronavirus (COVID-19) at home, clinic, and points of entry”. *ChemRxiv*, *93*(38), 13063-13071.

[64] Lewis, C. (2001). “Home diagnostic tests: the ultimate house call?”. *FDA Consumer, 35*, 18-22.

[65] Venture Planning Group, (2013). “US Home/Self-Testing Diagnostic Market: Diabetes, Pregnancy, Ovulation, Occult Blood--Business Challenges and Marketing Strategies for Suppliers”. https://www.reportlinker.com/

[66] Wang, Y., Wang, F., Han, Z., Huang, K., Wang, X., Liu, Z., & Lu, Y. (2020). “Construction of sandwiched self-powered biosensor based on smart nanostructure and capacitor: Toward multiple signal amplification for thrombin detection”. *Sensors and Actuators B: Chemical*, *304*, 127418.

[67] Gooding, J. J. (2006). “Biosensor technology for detecting biological warfare agents: Recent progress and future trends”. *Analytica chimica acta*, *559*(2), 137-151.

[68] Andryukov, B. G., Besednova, N. N., Romashko, R. V., Zaporozhets, T. S., & Efimov, T. A. (2020). “Label-free biosensors for laboratory-based diagnostics of infections: current achievements and new trends”. *Biosensors*, *10*(2), 11.

[69] Zhu, X., Wu, G., Xing, Y., Wang, C., Yuan, X., & Li, B. (2020). “Evaluation of single and combined toxicity of bisphenol A and its analogues using a highly-sensitive micro-biosensor”. *Journal of hazardous materials*, *381*, 120908.

[70] Ali, A. A., Altemimi, A. B., Alhelfi, N., & Ibrahim, S. A. (2020). “Application of Biosensors for Detection of Pathogenic Food Bacteria: A Review”. *Biosensors*, *10*(6), 58.

[71] Kucherenko, I. S., Soldatkin, O. O., Dzyadevych, S. V., & Soldatkin, A. P. (2020). “Electrochemical biosensors based on multienzyme systems: main groups, advantages and limitations–a review”. *Analytica Chimica Acta, 1111*, 114-131.

[72] Petrenko, V. A., and Sorokulova, I. B.,. (2004). "Detection of biological threats. A challenge for directed molecular evolution", *Journal of microbiological methods,58*, 147-168.

[73] Heurich, M., Kadir, M.K.A., and Tothill, I.E., (2011). “An electrochemical sensor based on carboxymethylated dextran modified gold surface for ochratoxin A analysis”. *Sensors and Actuators B: Chemical, 156*(1), 162-168.

[74] Dill, K., et al., (2001). “Antigen detection using microelectrode array microchips”. *Analytica Chimica Acta, 444*(1), 69-78.

[75] Williamson, M., et al., (1989). “Anti-T2 monoclonal antibody immobilization on quartz fibers: stability and recognition of T2 mycotoxin”. *Analytical Letters, 22*(4), 803-816.

[76] Raj, J., et al., (2009). “Surface immobilisation of antibody on cyclic olefin copolymer for sandwich immunoassay”. *Biosensors and Bioelectronics, 24*(8), 2654-2658.

[77] Babacan, S., et al., (2000). “Evaluation of antibody immobilization methods for piezoelectric biosensor application”. *Biosensors and Bioelectronics, 15*(11), 615-621.

---

[78] König, B. and M. Grätzel, (1993). "Development of a piezoelectric immunosensor for the detection of human erythrocytes". *Analytica Chimica Acta, 276*(2), 329-333.

[79] Herzog, G. and D.W.M. Arrigan, (2007). "Electrochemical strategies for the labelfree detection of amino acids, peptides and proteins". *Analyst, 132*(7), 615-632.

[80] Ronkainen-Matsuno, N.J., et al., (2002). "Electrochemical immunoassay moving into the fast lane". *TrAC Trends in Analytical Chemistry, 21*(4), 213-225.

[81] Reid, R. C., & Mahbub, I. (2020). "Wearable self-powered biosensors". *Current Opinion in Electrochemistry*, *19*, 55-62.

[82] Kim, D. M., & Yoo, S. M. (2020). "DNA-modifying enzyme reaction-based biosensors for disease diagnostics: recent biotechnological advances and future perspectives". *Critical Reviews in Biotechnology*, *40*(6), 1-17.

[83] Farajpour, A., Ghayesh, M. H., & Farokhi, H. (2018). "A review on the mechanics of nanostructures". *International Journal of Engineering Science*, *133*, 231-263.

[84] Kuan, S. L., Bergamini, F. R., & Weil, T. (2018). "Functional protein nanostructures: a chemical toolbox". *Chemical Society Reviews*, *47*(24), 9069-9105.

[85] Pirzada, M., & Altintas, Z. (2020). "Recent progress in optical sensors for biomedical diagnostics". *Micromachines*, *11*(4), 356.

[86] Abdul Kadir, M.K., and Tothill, I. E., (2010). "Development of an electrochemical immunosensor for fumonisins detection in foods". Toxins, *2*(4), 382398.

[87] Mazzola, L. (2003). "Commercializing nanotechnology". *Nature biotechnology, 21*, 1137-1143.

[88] Sharma, P. K., Park, J., Park, J. H., & Cho, K. (2020). "Wearable Computing for Defence Automation: Opportunities and Challenges in 5G Network". *IEEE Access*, *8*, 65993-66002.

[89] Marchand, A., Van Hall-Beauvais, A. K., & Correia, B. E. (2022). “Computational design of novel protein–protein interactions–An overview on methodological approaches and applications”. *Current Opinion in Structural Biology*, *74*, 102370.

[90] Yu, W., Xu, X., Jin, K., Liu, Y., Li, J., Du, G., ... & Liu, L. (2022). “Genetically encoded biosensors for microbial synthetic biology: From conceptual frameworks to practical applications”. *Biotechnology Advances*, 62, 108077.

[91] Calzini, M. A., Malico, A. A., Mitchler, M. M., & Williams, G. J. (2021). “Protein engineering for natural product biosynthesis and synthetic biology applications”. *Protein Engineering, Design and Selection*, *34, 1-9*.

[92] Hamula, C. L., Guthrie, J. W., Zhang, H., Li, X. F., & Le, X. C. (2006). “Selection and analytical applications of aptamers”. *TrAC Trends in Analytical Chemistry*, *25*(7), 681-691.

[93] Ilgu, M., & Nilsen-Hamilton, M. (2016). “Aptamers in analytics”. *Analyst*, *141*(5), 1551-1568.

[94] Frutiger, A., Tanno, A., Hwu, S., Tiefenauer, R. F., Voros, J., & Nakatsuka, N. (2021). “Nonspecific binding—fundamental concepts and consequences for biosensing applications”. *Chemical Reviews*, *121*(13), 8095-8160.

[95] Lavigne, J. J., & Anslyn, E. V. (2001). “Sensing a paradigm shift in the field of molecular recognition: from selective to differential receptors”. *Angewandte Chemie International Edition*, *40*(17), 3118-3130.

[96] Liao, Z., Wang, J., Zhang, P., Zhang, Y., Miao, Y., Gao, S., et al.. (2018). “Recent advances in microfluidic chip integrated electronic biosensors for multiplexed detection”. *Biosensors and Bioelectronics*, *121*, 272-280.

[97] Castro, R. C., Saraiva, M. L. M., Santos, J. L., & Ribeiro, D. S. (2021). "Multiplexed detection using quantum dots as photoluminescent sensing elements or optical labels". *Coordination Chemistry Reviews*, *448*, 214181.

[98] Dillen, A., & Lammertyn, J. (2022). "Paving the way towards continuous biosensing by implementing affinity-based nanoswitches on state-dependent readout platforms". *Analyst,* 147, 1006-1023.

[99] Ben Jaber, S. S. (2017). "*Development of nanostructures materials for detection of ultra-trace levels of explosives based on Surface-enhanced Raman spectroscopy (SERS)".* (Doctoral dissertation, UCL (University College London)).

[100] Jeevanandam, J., Barhoum, A., Chan, Y. S., Dufresne, A., & Danquah, M. K. (2018). "Review on nanoparticles and nanostructured materials: history, sources, toxicity and regulations". *Beilstein journal of nanotechnology*, *9*(1), 1050-1074.

[101] Koch, C. C. (2006). "*Nanostructured materials: processing, properties and applications"*. William Andrew, *2nd edition,* 1-719.

[102] Colson, P., Henrist, C., & Cloots, R. (2013). "Nanosphere lithography: a powerful method for the controlled manufacturing of nanomaterials". *Journal of Nanomaterials*, *2013,* 1-19.

[103] Yu, Z., Tetard, L., Zhai, L., & Thomas, J. (2015). "Supercapacitor electrode materials: nanostructures from 0 to 3 dimensions". *Energy & Environmental Science*, *8*(3), 702-730.

[104] Lim, C. T. (2017). "Nanofiber technology: current status and emerging developments". *Progress in Polymer Science*, *70*, 1-17.

[105] Jagadish, C., & Pearton, S. J. (Eds.). (2011). "*Zinc oxide bulk, thin films and nanostructures: processing, properties, and applications"*. Elsevier.

[106] Nowack, K. C., Spanton, E. M., Baenninger, M., König, M., Kirtley, J. R., Kalisky, B., ... & Molenkamp, L. W. (2013). "Imaging currents in HgTe quantum wells in the quantum spin Hall regime". *Nature materials*, *12*(9), 787-791.

[107] Hoffman, S., Chevallier, D., Loss, D., & Klinovaja, J. (2017). "Spin-dependent coupling between quantum dots and topological quantum wires". *Physical Review B*, *96*(4), 045440.

[108] Liu, S., Xiao, J., Lu, X. F., Wang, J., Wang, X., & Lou, X. W. (2019). "Efficient Electrochemical Reduction of CO2 to HCOOH over Sub-2 nm SnO2 Quantum Wires with Exposed Grain Boundaries". *Angewandte Chemie International Edition*, *58*(25), 8499-8503.

[109] Dong, Y., Qiao, T., Kim, D., Parobek, D., Rossi, D., & Son, D. H. (2018). "Precise control of quantum confinement in cesium lead halide perovskite quantum dots via thermodynamic equilibrium". *Nano letters*, *18*(6), 3716-3722.

[110] Reshma, V. G., & Mohanan, P. V. (2019). "Quantum dots: Applications and safety consequences". *Journal of Luminescence*, *205*, 287-298.

[111] Edvinsson, T. (2018). "Optical quantum confinement and photocatalytic properties in two-, one-and zero-dimensional nanostructures". *Royal Society open science*, *5*(9), 180387.

[112] Yu, S., Wang, X., Xiang, H., Zhu, L., Tebyetekerwa, M., & Zhu, M. (2018). "Superior piezoresistive strain sensing behaviors of carbon nanotubes in one-dimensional polymer fiber structure". *Carbon*, *140*, 1-9.

[113] Zhu, J., Hou, J., Uliana, A., Zhang, Y., Tian, M., & Van der Bruggen, B. (2018). "The rapid emergence of two-dimensional nanomaterials for high-performance separation membranes". *Journal of Materials Chemistry A*, *6*(9), 3773-3792.

[114] Shehzad, K., Xu, Y., Gao, C., & Duan, X. (2016). “Three-dimensional macro-structures of two-dimensional nanomaterials”. *Chemical Society Reviews*, *45*(20), 5541-5588.

[115] Wu, Z. Y., Liang, H. W., Chen, L. F., Hu, B. C., & Yu, S. H. (2016). “Bacterial cellulose: a robust platform for design of three dimensional carbon-based functional nanomaterials”. *Accounts of chemical research*, *49*(1), 96-105.

[116] Gusev, A. I., & Rempel, A. A. (2004). “*Nanocrystalline materials”*. Cambridge Int Science Publishing.

[117] Kolobov, Y. R. (2007). “*Grain boundary diffusion and properties of nanostructured materials”*. Cambridge Int Science Publishing.

[118] Sharma, S., Jaiswal, S., Duffy, B., & Jaiswal, A. K. (2019). “Nanostructured materials for food applications: spectroscopy, microscopy and physical properties”. *Bioengineering*, *6*(1), 26.

[119] Rempel, A. A. (2007). “Nanotechnologies. Properties and applications of nanostructured materials”. *Russian Chemical Reviews*, *76*(5), 435.

[120] Novotny, L., & Hecht, B. (2012). “Surface plasmons”. In *Principles of Nano-Optics* (pp. 369-413). Cambridge: Cambridge University Press. doi:10.1017/CBO9780511794193.014

[121] Kelly, K. L., Coronado, E., Zhao, L. L., & Schatz, G. C. (2003). “The optical properties of metal nanoparticles: the influence of size, shape, and dielectric environment”. *The Journal of Physical Chemistry B*, *107*(3), 668-677.

[122] Holma, J. S., Sinclair, Y., Gauglitz, G. (1999). “Surface plasmon resonance sensors: Review”. *Sen. Actuators B: Chem*, *54*(1-2), 3-15.

[123] Ma, J., Wang, X., Feng, J., Huang, C., & Fan, Z. (2021). “Individual plasmonic nanoprobes for biosensing and bioimaging: recent advances and perspectives”. *Small*, *17*(8), 2004287.

[124] Rifat, A. A., Hasan, R., Ahmed, R., & Miroshnichenko, A. E. (2019). “Microstructured optical fiber-based plasmonic sensors”. In *Computational Photonic Sensors, Springer,* 203-232.

[125] Li, P., Long, F., Chen, W., Chen, J., Chu, P. K., & Wang, H. (2020). “Fundamentals and applications of surface-enhanced Raman spectroscopy–based biosensors”. *Current Opinion in Biomedical Engineering*, *13*, 51-59.

[126] Raman, C. V., & Krishnan, K. S. (1928). “A new type of secondary radiation”. *Nature*, *121*(3048), 501-502.

[127] Raman, C.V. (1928). “A new radiation”. *Indian Journal of physics, 2*, 387-398.

[128] McNay, G., Eustace, D., Smith, W. E., Faulds, K., & Graham, D. (2011). “Surface-enhanced Raman scattering (SERS) and surface-enhanced resonance Raman scattering (SERRS): a review of applications”. *Applied spectroscopy*, *65*(8), 825-837.

[129] Colthup, N. (2012). “*Introduction to infrared and Raman spectroscopy”*. *Elsevier*.

[130] Ferraro, J. R. (2003). “*Introductory Raman spectroscopy”*. *Elsevier*.

[131] John, R., Ferraro, N. K., & Chris, W., (1994). “*Introductory Raman Spectroscopy”*. 78-81. Academic press.

[132] Zhang, S. L. (2012). “*Raman spectroscopy and its application in nanostructures”*. John Wiley & Sons.

[133] https://www.edinst.com/blog/what-is-raman-spectroscopy

[134] Sur, U. K. (2010). “Surface-enhanced Raman spectroscopy”. *Resonance*, *15*(2), 154-164.

[135] Fan, M., Andrade, G. F., & Brolo, A. G. (2020). “A review on recent advances in the applications of surface-enhanced Raman scattering in analytical chemistry”. *Analytica Chimica Acta*, *1097*, 1-29.

---

[136] Chang, R. (Ed.). (2013). "*Surface enhanced Raman scattering*". Springer Science & Business Media.

[137] Kumar, S., Doi, Y., Namura, K., & Suzuki, M. (2020). "Plasmonic Nanoslit Arrays Fabricated by Serial Bideposition: Optical and Surface-Enhanced Raman Scattering Study". *ACS Applied Bio Materials*, *3*(5), 3226-3235.

[138] Kastrup, L., and Hell, S. W., "Absolute optical cross section of individual fluorescent molecules". *Angewandte Chemie International Edition, 43*, 6646-6649.

[139] Kneipp, K., and Kneipp, H., "Single molecule Raman scattering". A*pplied Spectroscopy, 60*, 322A.

[140] Burns, K. H., Srivastava, P., & Elles, C. G. (2020). "Absolute Cross Sections of Liquids from Broadband Stimulated Raman Scattering with Femtosecond and Picosecond Pulses". *Analytical Chemistry*, *92*(15), 10686-10692.

[141] McCreery, R. L. (2000). "Raman spectroscopy for chemical analysis". *John Wiley & Sons, Inc.*.

[142] Young, D. (2004). "*Computational chemistry: a practical guide for applying techniques to real world problems"*. *John Wiley & Sons*.

[143] Schmidt, M. W., Baldridge, K. K., Boatz, J. A., Elbert, S. T., Gordon, M. S., Jensen, J. H., ... & Windus, T. L. (1993). "General atomic and molecular electronic structure system". *Journal of computational chemistry*, *14*(11), 1347-1363.

[144] Barca, G. M., Bertoni, C., Carrington, L., Datta, D., De Silva, N., Deustua, J. E., ... & Harville, T. (2020). "Recent developments in the general atomic and molecular electronic structure system". *The Journal of Chemical Physics*, *152*(15), 154102.

---

[145] Lehtola, S., Visscher, L., & Engel, E. (2020). “Efficient implementation of the superposition of atomic potentials initial guess for electronic structure calculations in Gaussian basis sets”. *The Journal of Chemical Physics*, *152*(14), 144105.

[146] Gobato, R., Gobato, M. R. R., Heidari, A., & Mitra, A. (2019). “New Nano–Molecule Kurumi–C13H 20BeLi2SeSi/C13H19BeLi2SeSi, and Raman Spectroscopy Using ab initio, Hartree–Fock Method in the Base Set CC–pVTZ and 6–311G**(3df, 3pd)”. *J Anal Pharm Res*, *8*(1), 1-6.

[147] Fleischmann, M., Hendra, P., and McQuillan, A. (1974). “Raman spectra of pyridine adsorbed at a silver electrode”. *Chemical Physics Letters, 26*, 163-166.

[148] Jeanmaire, D. L.; Van Duyne, R. P. (1977). “Surface Raman Spectroelectrochemistry Part I. Heterocyclic, Aromatic, and Aliphatic Amines Adsorbed on the Anodized Silver Electrode”. *J. Electroanal. Chem. Interfacial Electrochem., 84*, 1−20.

[149] Albrecht, M. G.; Creighton, J. A. (1977). “Anomalously Intense Raman Spectra of Pyridine at a Silver Electrode”. *J. Am. Chem. Soc., 99*, 5215−5217.

[150] Philpott, M. R. (1975). “Effect of Surface Plasmons on Transitions in Molecules”. *J. Chem. Phys., 1975,* 62, 1812.

[151] Stiles, P. L., Dieringer, J. A., Shah, N. C. and Van Duyne, R. P. (2008). "Surface-enhanced Raman spectroscopy", *Annu. Rev. Anal. Chem., 1*, 601-626.

[152] Moskovits, M. (1978). “Surface Roughness and the Enhanced Intensity of Raman Scattering by Molecules Adsorbed on Metals”. *J. Chem. Phys. 69*, 4159.

[153] Sharma, B., Frontiera, R. R., Henry, A. I., Ringe, E., and Van Duyne, R. P. (2012). “SERS: Materials, applications, and the future”. *Materials Today, 15*, 16-25.

[154] Haynes, C. L., McFarland, A. D., & Van Duyne, R. P. (2005). “Surface-enhanced Raman spectroscopy” *Analytical Chemistry, 77*(17), 338-346.

[155] Moskovits, M. (2005). “Surface-enhanced Raman spectroscopy: a brief retrospective”. *Journal of Raman Spectroscopy: An International Journal for Original Work in all Aspects of Raman Spectroscopy, Including Higher Order Processes, and also Brillouin and Rayleigh Scattering*, *36*(6-7), 485-496.

[156] Le Ru, E. C., Etchegoin, P. G., Grand, J., Félidj, N., Aubard, J., Lévi, G., ... & Krenn, J. R. (2008). “Surface enhanced Raman spectroscopy on nanolithography-prepared substrates”. *Current Applied Physics*, *8*(3-4), 467-470.

[157] Gunnarsson, L., Bjerneld, E. J., Xu, H., Petronis, S., Kasemo, B., & Käll, M. (2001). “Interparticle coupling effects in nanofabricated substrates for surface-enhanced Raman scattering”. *Applied Physics Letters*, *78*(6), 802-804.

[158] Kahl, M., Voges, E., Kostrewa, S., Viets, C., & Hill, W. (1998). “Periodically structured metallic substrates for SERS”. *Sensors and Actuators B: Chemical*, *51*(1-3), 285-291.

[159] Le Ru, E. C., and Etchegoin, P. G. (2012). “Single-molecule surface-enhanced Raman spectroscopy”. *Annual Review of Physical Chemistry, 63*, 65-87.

[160] Chaffin, E., O’Connor, R. T., Barr, J., Huang, X., & Wang, Y. (2016). “Dependence of SERS enhancement on the chemical composition and structure of Ag/Au hybrid nanoparticles”. *The Journal of Chemical Physics*, *145*(5), 054706.

[161] Eremina, O. E., Czaja, A. T., Fernando, A., Aron, A., Eremin, D. B., & Zavaleta, C. (2022). “Expanding the Multiplexing Capabilities of Raman Imaging to Reveal Highly Specific Molecular Expression and Enable Spatial Profiling”. *ACS nano, 16*(7), 10341-10353.

---

[162] Krishna, R., & Colak, I. (2022). “Advances in Biomedical Applications of Raman Microscopy and Data Processing: A Mini Review”. *Analytical Letters, 56*(4),576-617.

[163] Ding, Y., Sun, Y., Liu, C., Jiang, Q. Y., Chen, F., & Cao, Y. (2023). “SERS-Based Biosensors Combined with Machine Learning for Medical Application”. *ChemistryOpen*, *12*(1), e202200192.

[164] Zhang, L., Zhang, Y., Wang, X., & Zhang, D. (2021). “Plasma-Driven Photocatalysis Based on Gold Nanoporous Arrays”. *Nanomaterials*, *11*(10), 2710.

[165] Ren, X., Cao, E., Lin, W., Song, Y., Liang, W., & Wang, J. (2017). “Recent advances in surface plasmon-driven catalytic reactions”. *RSC Advances*, *7*(50), 31189-31203.

[166] Huynh, L. T. M., Trinh, H. D., Lee, S., & Yoon, S. (2020). “Plasmon-driven protodeboronation reactions in nanogaps”. *Nanoscale*, *12*(47), 24062-24069.

[167] Oh, Y. J., & Jeong, K. H. (2012). “Glass Nanopillar Arrays with Nanogap-Rich Silver Nanoislands for Highly Intense Surface Enhanced Raman Scattering”. *Advanced Materials*, *24*(17), 2234-2237.

[168] Sun, M., Zhang, Z., Zheng, H., & Xu, H. (2012). “In-situ plasmon-driven chemical reactions revealed by high vacuum tip-enhanced Raman spectroscopy”. *Scientific reports*, *2*(1), 1-4.

[169] Shattique, M. R., & Stepanova, M. (2020). “Surface Plasmon-Driven Reversible Transformation of DNA-Bound Methylene Blue Detected In-Situ by SERS”. *Plasmonics*, *15*(2), 427-434.

[170] Devasia, D., Das, A., Mohan, V., & Jain, P. K. (2021). “Control of Chemical Reaction Pathways by Light–Matter Coupling”. *Annual Review of Physical Chemistry*, *72*, 423-443.

[171] Domke, K. F., Zhang, D., & Pettinger, B. (2007). “Tip-enhanced Raman spectra of picomole quantities of DNA nucleobases at Au (111)”. *Journal of the American Chemical Society*, *129*(21), 6708-6709.

[172] Su, H. S., Feng, H. S., Wu, X., Sun, J. J., & Ren, B. (2021). “Recent advances in plasmon-enhanced Raman spectroscopy for catalytic reactions on bifunctional metallic nanostructures”. *Nanoscale*, *13*(33), 13962-13975.

[173] Liu, X., Guo, J., Li, Y., Wang, B., Yang, S., Chen, W., ... & Ma, X. (2021). “SERS substrate fabrication for biochemical sensing: Towards point-of-care diagnostics”. *Journal of Materials Chemistry B*, *9*(40), 8378-8388.

[174] Jung, G. B., Bae, Y. M., Lee, Y. J., Ryu, S. H., & Park, H. K. (2013). “Nanoplasmonic Au nanodot arrays as a SERS substrate for biomedical applications”. *Applied surface science*, *282*, 161-164.

[175] Liu, M., Bhandari, A., Haqqani Mohammed, M. A., Radu, D. R., & Lai, C. Y. (2021). “Versatile Silver Nanoparticles-Based SERS Substrate with High Sensitivity and Stability”. *Applied Nano*, *2*(3), 242-256.

[176] Fan, M., Andrade, G. F., & Brolo, A. G. (2011). “A review on the fabrication of substrates for surface enhanced Raman spectroscopy and their applications in analytical chemistry”. *Analytica chimica acta*, *693*(1-2), 7-25.

[177] Dinish, U. S., Fu, C. Y., Goh, D., & Olivo, M. (2010, December). “Nanosphere templated optical fiber for In-Vivo SERS sensing applications”. In *2010 Photonics Global Conference* (pp. 1-5). IEEE.

[178] Coluccio, M. L., Das, G., Mecarini, F., Gentile, F., Pujia, A., Bava, L., ... & Di Fabrizio, E. (2009). “Silver-based surface enhanced Raman scattering (SERS) substrate fabrication

using nanolithography and site selective electroless deposition". *Microelectronic Engineering*, *86*(4-6), 1085-1088.

[179] Ding, T., Sigle, D. O., Herrmann, L. O., Wolverson, D., & Baumberg, J. J. (2014). "Nanoimprint lithography of Al nanovoids for deep-UV SERS". *ACS applied materials & interfaces*, *6*(20), 17358-17363.

[180] Zhang, Q., Lee, Y. H., Phang, I. Y., Lee, C. K., & Ling, X. Y. (2014). "Hierarchical 3D SERS Substrates Fabricated by Integrating Photolithographic Microstructures and Self-Assembly of Silver Nanoparticles". *Small*, *10*(13), 2703-2711.

[181] Dinish, U. S., Yaw, F. C., Agarwal, A., & Olivo, M. (2011). "Development of highly reproducible nanogap SERS substrates: Comparative performance analysis and its application for glucose sensing". *Biosensors and Bioelectronics*, *26*(5), 1987-1992.

[182] Gao, T., Xu, Z., Fang, F., Gao, W., Zhang, Q., & Xu, X. (2012). "High performance surface-enhanced Raman scattering substrates of Si-based Au film developed by focused ion beam nanofabrication". *Nanoscale research letters*, *7*(1), 1-8.

[183] Scholder, O., Jefimovs, K., Shorubalko, I., Hafner, C., Sennhauser, U., & Bona, G. L. (2013). "Helium focused ion beam fabricated plasmonic antennas with sub-5 nm gaps". *Nanotechnology*, *24*(39), 395301.

[184] Tao, Z., Zhao, W., Wang, S., Zhao, B., Hua, R., Qin, J., & Xu, Z. (2021). "Annealing treatment of focused gallium ion beam processing of SERS gold substrate". *Nanotechnology and Precision Engineering*, *4*(4), 043004.

[185] Pangpaiboon, N., Phetnam, K., Kalasung, S., Chananonawathorn, C., Patthanasettakul, V., Horprathum, M., … & Limwichean, S. (2021). "Raman signal enhancement of low-cost

metal sheet SERS with gold decoration". *Journal of Metals, Materials and Minerals*, *31*(4), 33-39.

[186] Korcoban, D., Kandjani, A. E., Coyle, V. E., Alenezy, E. K., Bhargava, S. K., & Sabri, Y. (2022). "Recyclable SERS substrate: Optimised by reducing masking effect through colloidal lithography". *Applied Surface Science*, *578*, 151852.

[187] Lim, L. K. (2018). "*Study of plasmonic nano-arrays for the development of cost-effective SERS substrate".* (Doctoral dissertation).

[188] Cai, J., Liu, R., Jia, S., Feng, Z., Lin, L., Zheng, Z., ... & Wang, Z. (2021). "SERS hotspots distribution of the highly ordered noble metal arrays on flexible substrates". *Optical Materials, 122*, 111779.

[189] Li, P., Long, F., Chen, W., Chen, J., Chu, P. K., & Wang, H. (2020). "Fundamentals and applications of surface-enhanced Raman spectroscopy–based biosensors". *Current Opinion in Biomedical Engineering*, *13*, 51-59.

[190] Masterson, A. N., Liyanage, T., Berman, C., Kaimakliotis, H., Johnson, M., & Sardar, R. (2020). "A novel liquid biopsy-based approach for highly specific cancer diagnostics: mitigating false responses in assaying patient plasma-derived circulating microRNAs through combined SERS and plasmon-enhanced fluorescence analyses". *Analyst*, *145*(12), 4173-4180.

[191] Kang, S., Kim, I., & Vikesland, P. J. (2021). "Discriminatory Detection of ssDNA by Surface-Enhanced Raman Spectroscopy (SERS) and Tree-Based Support Vector Machine (Tr-SVM)". *Analytical Chemistry*, *93*(27), 9319-9328.

[192] Petschulat, J., Cialla, D., Janunts, N., Rockstuhl, C., Hübner, U., Möller, R., ... & Pertsch, T. (2010). “Doubly resonant optical nanoantenna arrays for polarization resolved”. *Optics Express*, *18*(5), 4184-4197.

[193] Dong, H., Sun, L. D., & Yan, C. H. (2020). “Upconversion emission studies of single particles”. *Nano Today, 35*, 100956.

[194] Güémez, J., Fiolhais, M., & Fernández, L. A. (2016). “The principle of relativity and the de Broglie relation”. *American Journal of Physics*, *84*(6), 443-447.

[195] Rose, H. H. (2008). “Optics of high-performance electron microscopes”. *Science and Technology of Advanced Materials*, *9*(1), 014107.

[196] Jin, Q., Liang, G., Kong, W., Liu, L., Wen, Z., Zhou, Y.,et al.. (2022). “Negative index metamaterial at ultraviolet range for subwavelength photolithography”. *Nanophotonics*, *11*(8), 1643-1651.

[197] Mojarad, N., Gobrecht, J., & Ekinci, Y. (2015). Beyond EUV lithography: a comparative study of efficient photoresists' performance. *Scientific reports*, *5*(1), 1-7.

[198] Chen, Y. (2015). “Nanofabrication by electron beam lithography and its applications: A review”. *Microelectronic Engineering*, *135*, 57-72.

[199] Altissimo, M. (2010). “E-beam lithography for micro-/nanofabrication”. *Biomicrofluidics*, *4*(2), 026503.

[200] Chakrabarty, S., Ouyang, C., Krysak, M., Trikeriotis, M., Cho, K., Giannelis, E. P., & Ober, C. K. (2013). “Oxide nanoparticle EUV resists: toward understanding the mechanism of positive and negative tone patterning”. In *Extreme Ultraviolet (EUV) Lithography IV*, *8679*, 34-41.

---

[201] Chen, Y., Macintyre, D., & Thoms, S. (1999). “Electron beam lithography process for T- and Γ-shaped gate fabrication using chemically amplified DUV resists and PMMA”. *Journal of Vacuum Science & Technology B: Microelectronics and Nanometer Structures Processing, Measurement, and Phenomena*, *17*(6), 2507-2511.

[202] Tanenbaum, D. M., Lo, C. W., Isaacson, M., Craighead, H. G., Rooks, M. J., Lee, K. Y., ... & Chang, T. H. P. (1996). “High resolution electron beam lithography using ZEP-520 and KRS resists at low voltage”. *Journal of Vacuum Science & Technology B: Microelectronics and Nanometer Structures Processing, Measurement, and Phenomena*, *14*(6), 3829-3833.

[203] Chen, Y., MacIntyre, D., & Thoms, S. (2001). “T-gate fabrication using a ZEP520A/UVIII bilayer”. *Microelectronic engineering*, *57*, 939-943.

[204] Mohammad, M. A., Dew, S. K., & Stepanova, M. (2013). “SML resist processing for high-aspect-ratio and high-sensitivity electron beam lithography”. *Nanoscale research letters*, *8*(1), 1-7.

[205] Zhou, J., Ji, H., Lan, T., Yan, J., Zhou, W., & Miao, X. (2015). “Investigation of the Hydrogen Silsesquioxane (HSQ) Electron Resist as Insulating Material in Phase Change Memory Devices”. *Journal of electronic materials*, *44*(1), 235-243.

[206] Toomey, E., Colangelo, M., & Berggren, K. K. (2019). “Investigation of ma-N 2400 series photoresist as an electron-beam resist for superconducting nanoscale devices”. *Journal of Vacuum Science & Technology B, Nanotechnology and Microelectronics: Materials, Processing, Measurement, and Phenomena*, *37*(5), 051207.

[207] Van Dodewaard, A. J., Ketelaars, W. S. M. M., Roes, R. F. M., Kwinten, J. A. J., van Delft, F. C. M. J. M., van Run, A. J., ... & Romijn, J. (2000). “Comparison of negative tone resists

---

NEB22 and UVN30 in e-beam lithography". *Microelectronic engineering*, *53*(1-4), 461-464.

[208] Manfrinato, V. R., Zhang, L., Su, D., Duan, H., Hobbs, R. G., Stach, E. A., & Berggren, K. K. (2013). "Resolution limits of electron-beam lithography toward the atomic scale". *Nano letters*, *13*(4), 1555-1558.

[209] Manfrinato, V. R., Wen, J., Zhang, L., Yang, Y., Hobbs, R. G., Baker, B., ... & Berggren, K. K. (2014). "Determining the resolution limits of electron-beam lithography: direct measurement of the point-spread function". *Nano letters*, *14*(8), 4406-4412.

[210] Chen, W., & Ahmed, H. (1993). "Fabrication of 5–7 nm wide etched lines in silicon using 100 keV electron-beam lithography and polymethylmethacrylate resist". *Applied physics letters*, *62*(13), 1499-1501.

[211] Cherala, A., Pandya, P. N., Liechti, K. M., & Sreenivasan, S. V. (2021). "Extending the resolution limits of nanoshape imprint lithography using molecular dynamics of polymer crosslinking". *Microsystems & Nanoengineering*, *7*(1), 1-10.

[212] Luo, S., Hoff, B. H., Maier, S. A., & de Mello, J. C. (2021). Scalable Fabrication of Metallic Nanogaps at the Sub-10 nm Level. *Advanced Science*, *8*(24), 2102756.

[213] Eder, K., Bhatia, V., Qu, J., Van Leer, B., Dutka, M., & Cairney, J. M. (2021). A multi-ion plasma FIB study: Determining ion implantation depths of Xe, N, O and Ar in tungsten via atom probe tomography. *Ultramicroscopy*, *228*, 113334.

[214] Vila, A., Hernandez-Ramirez, F., Rodriguez, J., Casals, O., Romano-Rodriguez, A., Morante, J. R., & Abid, M. (2006). "Fabrication of metallic contacts to nanometre-sized materials using a focused ion beam (FIB)". *Materials Science and Engineering: C*, *26*(5-7), 1063-1066.

[215] Gierak, J., Madouri, A., Biance, A. L., Bourhis, E., Patriarche, G., Ulysse, C., ... & Jede, R. (2007). "Sub-5 nm FIB direct patterning of nanodevices". *Microelectronic engineering*, *84*(5-8), 779-783.

[216] Wang, Z. M. (Ed.). (2013). *"FIB nanostructures". New York: Springer International Publishing*, 1-530.

[217] Rashid, S., Walia, J., Northfield, H., Hahn, C., Olivieri, A., Lesina, A. C., ... & Berini, P. (2021). Helium ion beam lithography and liftoff. *Nano Futures*, *5*(2), 025003.

[218] LeFebvre, J. C., & Cybart, S. A. (2021). "Large-Scale Focused Helium Ion Beam Lithography". *IEEE Transactions on Applied Superconductivity*, *31*(5), 1-4.

[219] Allen, F. I. (2021). "A review of defect engineering, ion implantation, and nanofabrication using the helium ion microscope". *Beilstein journal of nanotechnology*, *12*(1), 633-664.

[220] Maas, D., van Veldhoven, E., Chen, P., Sidorkin, V., Salemink, H., van der Drift, E., & Alkemade, P. (2010, April). "Nanofabrication with a helium ion microscope". In *Metrology, Inspection, and Process Control for Microlithography XXIV*, *7638*, 763814.

[221] Notte, J., Ward, B., Economou, N., Hill, R., Percival, R., Farkas, L., & McVey, S. (2007, September). "An introduction to the helium ion microscope". In *AIP Conference proceedings*, *931*(1), 489-496.

[222] Xia, Y., Xiong, Y., Lim, B., & Skrabalak, S. E. (2009). "Shape-controlled synthesis of metal nanocrystals: simple chemistry meets complex physics?". *Angewandte Chemie (International ed. in English), 48*(1), 60–103. https://doi.org/10.1002/anie.200802248

[223] Suzuki, K., & Oho, E. (2014). "Special raster scanning for reduction of charging effects in scanning electron microscopy". *Scanning: The Journal of Scanning Microscopies*, *36*(3), 327-333.

[224] Rossnagel, S. M. (1995). “Directional and preferential sputtering-based physical vapor deposition”. *Thin solid films*, *263*(1), 1-12.

[225] Singh, J., & Wolfe, D. E. (2005). “Review Nano and macro-structured component fabrication by electron beam-physical vapor deposition (EB-PVD)”. *Journal of materials Science*, *40*(1), 1-26.

[226] Wadja, B., Nawrocki, D., & Rattray, L. (2021, May). “Bi-Layer Lift-off Resist Process Optimization of Insulator Film for Neural Probe Fabrication”. In *2021 32nd Annual SEMI Advanced Semiconductor Manufacturing Conference (ASMC), IEEE Xplore,* 1-4.

[227] Chen, Y., Peng, K., & Cui, Z. (2004). “A lift-off process for high resolution patterns using PMMA/LOR resist stack”. *Microelectronic engineering*, *73*, 278-281.

[228] Cremers, V., Puurunen, R. L., & Dendooven, J. (2019). “Conformality in atomic layer deposition: Current status overview of analysis and modelling”. *Applied Physics Reviews*, *6*(2), 021302.

[229] Gutierrez-Rivera, L., Peters, R. F., Dew, S. K., & Stepanova, M. (2013). “Application of EBL fabricated nanostructured substrates for surface enhanced Raman spectroscopy detection of protein A in aqueous solution”. *Journal of Vacuum Science & Technology B, Nanotechnology and Microelectronics: Materials, Processing, Measurement, and Phenomena*, *31*(6), 06F901.

[230] Muhammad, M., Buswell, S. C., Dew, S. K., & Stepanova, M. (2011). “Nanopatterning of PMMA on insulating surfaces with various anticharging schemes using 30 keV electron beam lithography”. *Journal of Vacuum Science & Technology B, Nanotechnology and Microelectronics: Materials, Processing, Measurement, and Phenomena*, *29*(6), 06F304.

[231] Electron-beam lithography simulator, www.nanofab.ualberta.ca/2016/news/ electron-beam-lithography-simulator/

[232] Peters, R., Fito, T., Gutierrez-Rivera, L., Dew, S., & Stepanova, M. (2013). “Study of multilayer systems in electron beam lithography”. *Journal of Vacuum Science & Technology B, Nanotechnology and Microelectronics: Materials, Processing, Measurement, and Phenomena*, *31*(6), 06F407.

[233] Jones, S. A., & Jenkins, B. J. (2018). “Recent insights into targeting the IL-6 cytokine family in inflammatory diseases and cancer”. *Nature Reviews Immunology*, *18*(12), 773-789.

[234] Gao, Y., Nguyen, D. T., Yeo, T., Lim, S. B., Tan, W. X., Madden, L. E., ... & Lim, C. T. (2021). “A flexible multiplexed immunosensor for point-of-care in-situ wound monitoring”. *Science Advances*, *7*(21), eabg9614.

[235] https://www.ks.uiuc.edu/Research/vmd

[236] Protein Data Bank, https://www.rcsb.org

[237] de la O-Cuevas, E., Badillo-Ramírez, I., Islas, S. R., Araujo-Andrade, C., & Saniger, J. M. (2019). “Sensitive Raman detection of human recombinant interleukin-6 mediated by DCDR/GERS hybrid platforms”. *RSC advances*, *9*(22), 12269-12275.

[238] Barth, A. (2007). “Infrared spectroscopy of proteins”. *Biochimica et Biophysica Acta (BBA)-Bioenergetics*, *1767*(9), 1073-1101.

[239] Tuma, R. (2005). “Raman spectroscopy of proteins: from peptides to large assemblies”. *Journal of Raman Spectroscopy: An International Journal for Original Work in all Aspects of Raman Spectroscopy, Including Higher Order Processes, and also Brillouin and Rayleigh Scattering*, *36*(4), 307-319.

[240] Zhu, G., Zhu, X., Fan, Q., & Wan, X. (2011). "Raman spectra of amino acids and their aqueous solutions". *Spectrochimica Acta Part A: Molecular and Biomolecular Spectroscopy*, *78*(3), 1187-1195.

[241] Talari, A. C. S., Movasaghi, Z., Rehman, S., & Rehman, I. U. (2015). "Raman spectroscopy of biological tissues". *Applied spectroscopy reviews*, *50*(1), 46-111.

[242] Guicheteau, J., Argue, L., Hyre, A., Jacobson, M., & Christesen, S. D. (2006, May). "Raman and surface-enhanced Raman spectroscopy of amino acids and nucleotide bases for target bacterial vibrational mode identification". In *Chemical and Biological Sensing VII, 6218*, 174-184.

[243] Davydov, A. S. (1982). "Solitons in quasi-one-dimensional molecular structures". *Soviet Physics Uspekhi*, *25*(12), 898.

[244] Ukmar-Godec, T., Wegmann, S., & Zweckstetter, M. (2020). "Biomolecular condensation of the microtubule-associated protein tau". In *Seminars in Cell & Developmental Biology, 99*, 202-214.

[245] Rai, S. K., Savastano, A., Singh, P., Mukhopadhyay, S., & Zweckstetter, M. (2021). "Liquid–liquid phase separation of tau: From molecular biophysics to physiology and disease". *Protein Science*, *30*(7), 1294-1314.

[246] Lu, T., & Spruijt, E. (2020). "Multiphase complex coacervate droplets". *Journal of the American Chemical Society*, *142*(6), 2905-2914.

[247] Altug, H., Oh, S. H., Maier, S. A., & Homola, J. (2022). "Advances and applications of nanophotonic biosensors". *Nature Nanotechnology*, *17*(1), 5-16.

Appendix

Supplementary Figures

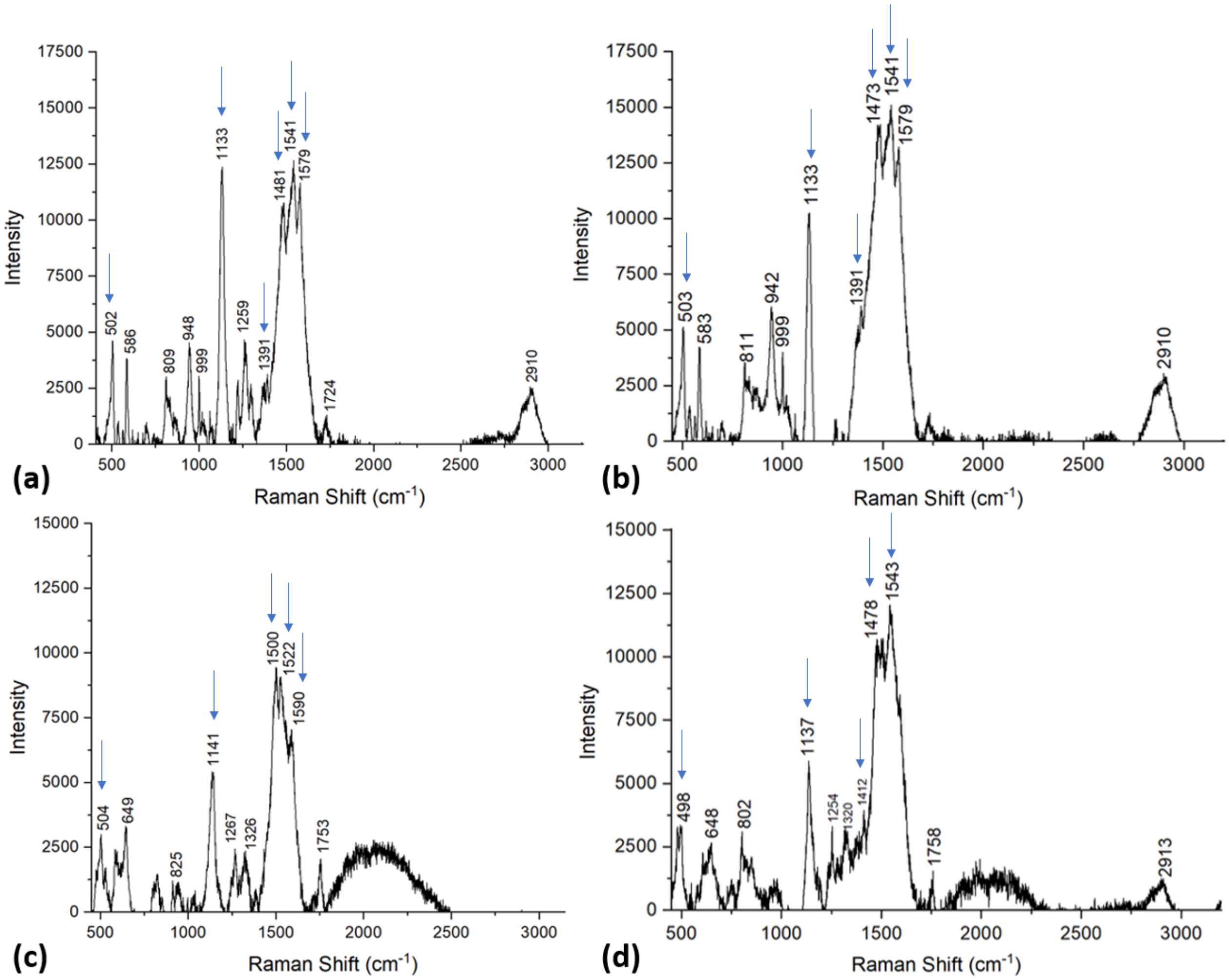

Figure 37: Additional SERS spectra of Au-immobilized DNA/IL-6 complex after background subtraction. The arrows indicate characteristic features of the fingerprint.

Supplementary Tables

Table II: Average positions and standard deviations of characteristic features of the SERS fingerprint of Au-immobilized DNA/IL-6 complex.

Characteristic features of DNA/IL-6 SERS fingerprint	**Average position (*) (cm^{-1})**	**Standard deviation (*) (cm^{-1})**
1. Broad bundle of overlapping peaks between 1350 and 1600 cm^{-1}	1501.4	19.5
2. Strong, narrow peak at 1333-1141 cm^{-1}	1135.4	3.5
3. Medium-intensity peak at 498-504 cm^{-1}	501.8	2.3

(*) The average positions and the standard deviations are calculated across the five SERS spectra in **Figures 29** and **37(a-d).**